TEMPORAL AND SPATIAL ANALYSES OF PRESSURE PERTURBATIONS FROM THE USARRAY TRANSPORTABLE ARRAY

by

Alexander Andrew Jacques

A dissertation submitted to the faculty of
The University of Utah
in partial fulfillment of the requirements for the degree of

Doctor of Philosophy

Department of Atmospheric Sciences

The University of Utah

December 2016

The University of Utah Graduate School

STATEMENT OF DISSERTATION APPROVAL

The dissertation of **Alexander Andrew Jacques**

has been approved by the following supervisory committee members:

John D. Horel	, Chair	**08/11/2016** Date Approved
Erik Tavis Crosman	, Member	**08/11/2016** Date Approved
Courtenay Strong	, Member	**08/11/2016** Date Approved
William James Steenburgh	, Member	**08/11/2016** Date Approved
Frank L. Vernon	, Member	**08/11/2016** Date Approved

and by **Kevin D. Perry** , Chair/Dean of

the Department/College/School of **Atmospheric Sciences**

and by David B. Kieda, Dean of The Graduate School.

ABSTRACT

As part of the EarthScope initiative, the USArray Transportable Array (TA) consisted of seismic sensor platforms that were developed to improve understanding of subsurface processes beneath the North American continent. Atmospheric pressure sensors deployed as part of the TA provided 1-2 yr time series of 1-Hz surface pressure observations at over 1,000 locations across the central and eastern United States and Alaska. To further the availability of these data to the atmospheric science research community, a repository was created within the Research Data Archive at the National Center for Atmospheric Research (http://dx.doi.org/10.5065/D6028PRS), and visualizations are available online (http://meso1.chpc.utah.edu/usarray/).

The frequencies of prominent mesoscale (10 min - 4 h), subsynoptic (4 - 30 h), and synoptic (30 h - 5 day) pressure signatures as a function of location and season were determined from the time series at each location. Results were consistent with other climatologies related to mesoscale convective systems, inertial gravity waves, diurnal and semidiurnal cycles, and regions of prominent cyclogenesis. Since large mesoscale pressure perturbations were common across the central Great Plains during the spring and summer of 2011, TA observations in that region were assimilated using hourly surface pressure background grids to obtain surface pressure analyses every 5 min at 5 km horizontal resolution. Prominent mesoscale features, most often associated with

mesoscale convective systems and gravity waves, were identified and tracked in order to assess their size, duration, propagation speed, and direction as a function of location and season.

TABLE OF CONTENTS

ACKNOWLEDGEMENTS

I would first like to acknowledge my partner, Mike, who has given me the encouragement and support for completing this work. I would like to thank my committee members, Drs. John Horel, Erik Crosman, Frank Vernon, Jim Steenburgh, and Court Strong, for their guidance with this dissertation. John has been a fantastic advisor and this work would not be possible without his valuable input. Erik has also been a tremendous resource for this research and the other projects that I have been a part of. I would like to thank the MesoWest group, managed by John, for taking a chance on hiring me in September 2011 and for continuing to support me during my doctorate pursuit. This work would not have been possible without the programming guidance I obtained with MesoWest. I thank the Array Network Facility staff, particularly Jon Tytell at Scripps Institution of Oceanography, for providing me with answers to questions regarding the TA platforms and quality control assistance. I would like to acknowledge NCAR for allowing us to create an official atmospheric science repository for the 1-Hz TA data we have collected. I also would like to acknowledge MesoWest, Iowa Environmental Mesonet, National Centers for Environmental Prediction, Pennsylvania State University, and University of Wyoming for access to their data resources via various web interfaces. I also thank the University of Utah Center for High Performance Computing (CHPC) for computational hardware and software. This material is based upon work supported by the National Science Foundation under Grant Number 1252315.

Any opinion, findings, and conclusions or recommendations expressed in this material are those of the authors(s) and do not necessarily reflect the views of the National Science Foundation.

CHAPTER 1

INTRODUCTION

1.1 Background

Observations of atmospheric barometric pressure, both direct and derived quantities (e.g., sea-level pressure), have been and continue to be an extremely useful resource for the detection and explanation of meteorological phenomena at all relevant spatial and temporal scales. Such phenomena include atmospheric turbulence (Viana et al. 2010), mesoscale convective systems and complexes (Carbone et al. 2002), mesoscale and inertial gravity waves (Bosart et al. 1998; Koppel et al. 2000; Nappo 2002; Sutherland 2010; Clark et al. 2014), thermal diurnal and semidiurnal cycles (Mass et al. 1991), synoptic baroclinic waves (Alexandersson et al. 1998; Bärring and Fortuniak 2009), and seasonal and multiyear oscillations (Jones et al. 2003). It is well known that the mean surface pressure field has its largest variation in the vertical plane, decreasing exponentially with elevation. Perturbations are induced on the horizontal pressure field by atmospheric processes such as those described above. Since surface pressure is the columnar "weight" of the total atmosphere at a defined location, it is impacted by all relevant processes regardless of where they happen vertically in the atmosphere. Further, while phenomena may produce impacts on other state variables (e.g., temperature and moisture), direct impacts may not be necessarily sensed at the surface of the earth if the

phenomenon is not occurring at the surface. Thus, surface pressure measurements remain an important resource for the identification and tracking of atmospheric processes when other surface state variables may not necessarily respond.

Through the decades, advances in observational measurement techniques, data dissemination, and numerical weather analysis and prediction have shaped how pressure data are utilized. One of the more well-known uses of pressure observations is related to the development of synoptic storm genesis, decay, and track climatologies. In particular, derived sea-level pressure observations have been utilized to identify prominent synoptic storm tracks through analysis and reanalysis of minimum (maximum) sea-level pressure regions indicative of cyclones (anticyclones) (Reitan 1974; Zishka and Smith 1980). Expansion of these synoptic climatologies to data-sparse regions is aided by the advancement of numerical model reanalyses which can provide pressure data on grids with regular spatial and temporal resolution (Thomas and Martin 2007; Ferreira et al. 2013). Derived quantities such as pressure tendency (change of pressure with time) aid in the detection of prominent regions of cyclogenesis, anticyclogenesis, and cyclolysis, which serve as useful analog-based information for forecasting purposes (Sanders and Gyakum 1980; Krueger and von Storch 2012).

Advances in numerical modeling and statistical identification techniques have led to efforts to improve both data assimilation of observations into numerical forecasts as well as better understanding and prediction of shorter duration mesoscale events. In general, surface pressure variance increases drastically with temporal scale, where seasonal and synoptic phenomena have large variance and mesoscale has small variance. However, mesoscale events such as large-magnitude gravity waves and mesoscale

convective systems can induce temporally short but impressively strong pressure perturbations. These perturbations can result in a large-magnitude pressure gradient over a very small area which, in combination with other meteorological factors, can induce a response in the form of very strong surface winds that can pose a threat to life and property.

Following in the footsteps of T. Fujita's mesoanalyses of barograph traces, time-to-space reduction techniques have been heavily used to assist in detection of these mesoscale-based pressure wave features (Fujita and Brown 1958; Koch and Saleeby 2001; Johnson 2001). Large-amplitude gravity waves and severe mesoscale convective systems (MCSs) have been studied extensively (Ramamurthy et al. 1993; Coleman and Knupp 2009; Coleman and Knupp 2010; Adams-Selin and Johnson 2013). In several cases, pressure observations at hourly or longer intervals have been the most common tool available to study these events (e.g., Bosart et al. 1998). When observations at higher sampling intervals are available, signal processing techniques are often utilized to isolate discrete and recurring perturbations. Harmonic analysis has often been used to determine magnitude and phase of the diurnal, semidiurnal, and terdiurnal thermal tides (Mass et al. 1991; Ray and Poulose 2005; Li and Smith 2010). Various band-pass filtering techniques were utilized by Koch and O'Handley (1997) and Koch and Saleeby (2001) to isolate perturbations from mesoscale gravity waves using pressure observations at 5 min intervals, which provided much more accurate detail. Wavelet analysis techniques to extract discrete events in time and space are commonplace as well in the literature (Grivet-Talocia and Einaudi 1998; Grivet-Talocia et al. 1999). While certainly useful to assess specific events, wavelet techniques rely on specifying the expected

pressure fluctuation pattern to cast as the mother wavelet, which lends to the technique being less useful when not having the benefit of a priori knowledge of individual event structures (Torrence and Compo 1998).

Beyond time series analyses, surface pressure observations are a critical input to initialize numerical weather prediction models. Surface pressure lacks many of the representativeness issues (e.g., platform siting) that often plague other state variable observations (Mass and Madaus 2014). Typical errors related to pressure observations are either unavailable or inaccurate metadata (e.g., elevation of the instrument), instrument error, or propagation of errors due to conversion of the measurement to sea level or some other elevation (e.g., Mohr 2004). Improved detection and forecasts of phenomena that produce pressure perturbations using observations at higher spatial and temporal densities have been shown in many recent studies and experiments (Anderson et al. 2005; Dirren et al. 2007; Lei and Anderson 2014).

Depending on the objective, studies have invoked various versions of identification and tracking algorithms to assess detection and movement of features within their respective datasets (e.g., Raible et al. 2008). Objective feature detection and tracking of large-scale atmospheric systems use methodologies associated with nearest-neighbor approaches (e.g., König et al. 1993), image processing (e.g., Hodges 1994), spectral techniques (e.g., Souders et al. 2014a,b; Kravtsov et al. 2015), band-pass filtered variance, and system-centered approaches (Hoskins and Hodges 2002; Hodges et al. 2003), where the Eulerian band-passed variance detected at each grid cell could provide information on feature passage. With improving computational processing, operational identification techniques have been developed to assess smaller features such as the

operational Storm Cell Identification and Tracking (SCIT, Johnson et al. 1998), and Tornado Vortex Signature (TVS, Brown and Wood 2012) algorithms presently deployed within NWS radar systems. Further approaches for radar and satellite image feature identification and tracking using fuzzy logic (Jung and Lee 2015) and cross-correlation between successive images (Liu et al. 2014) have also been developed.

Efforts to improve model verification routines have led to the development of the Method for Object-Based Diagnostic Evaluation (MODE) system for numerical model data (Davis et al. 2006; Davis et al. 2009). The routine relies on fuzzy logic and additional algorithms to collocate regions of a given model scalar field (e.g., precipitation) with regions derived from verification data (e.g., gridded analysis or observational precipitation) to assess model performance. Further, an extension of MODE called MODE Time Domain (MODE-TD) allows for assessing the movement of detected features across time, providing an additional dimension for verification. Feature propagation speeds and directions are computed by MODE-TD using regression techniques that consider the zonal and meridional extent of the feature at each timestamp of existence (Bullock 2011). Both MODE and MODE-TD have been utilized for several numerical verification studies of mesoscale phenomena (Bullock 2011; Mittermaier and Bullock 2013; Clark et al. 2014; McMillen 2014; McMillen and Steenburgh 2015).

1.2 The USArray Transportable Array

While improving technologies have led to the advancement of data collection, archival, and dissemination practices, access to high-quality observations across large spatial regions at higher temporal resolution (< 1 h) remains a challenge. Conventional

observations, hereby denoted as measurements recorded from National Weather Service (NWS) Automated Surface/Weather Observing System (ASOS/AWOS) platforms, are readily available and are considered high-quality systems. Many of these stations are located at airports for the aviation industry, thus spatial coverage for these high-quality platforms is reasonably good across the continental United States. While access to higher temporal resolution data is improving (e.g., 5 min frequency), most users rely on these observations at hourly or 20 min intervals, depending on whether the station utilizes ASOS or AWOS software.

High-quality equipment is often deployed for many mesoscale field campaigns as well, typically with sufficient temporal resolution to accurately assess the translation of mesoscale features. However, the spatial region for many field campaigns is often reduced to a much smaller regional area and focused on the particular goals of the campaign. Access to the data from many past campaigns can also be a burdensome and sometimes restricted process. The access and dissemination of observations from many other surface-based mesonets, such as those available in MesoWest (Horel et al. 2002), certainly can aid in bridging the gap between high temporal and spatial datasets. However, concerns with equipment quality and maintenance between different mesonets can cause challenges when evaluating the data scientifically. New sources of pressure observations such as those available from mobile phones are being presently assessed for validity and use (e.g., Mass and Madaus 2014), though the relative availability and commercialization of such mobile resources renders their usability in many cases unknown.

Pressure sensors are utilized by many disciplines outside of atmospheric science

as well, which leads to the introduction of the primary observational dataset used for this dissertation. Over the previous decade, a massive field campaign has taken place across the United States within the seismic and geoscience communities. The National Science Foundation funded a program called EarthScope to develop a field campaign designed to research subsurface properties of the North American continent. EarthScope has led to the deployment of many different seismic and geoscience-based measurement systems.

Part of the EarthScope project involved the deployment of an array of seismic instrument platforms. The platforms were designed to be quickly installed, report real-time high temporal resolution (greater or equal to 1 Hz) data with minimal latency, and retrieved 1-2 yr after installation. After retrieval, the platforms were repaired as necessary and then redeployed at a new location. Approximately 400 platforms were designed for this purpose and designated as the USArray Transportable Array (TA). The TA was initially deployed across the western coastline of the United States and extended inland into the intermountain west during 2004-2005. After 1-2 yr of reporting, the western-most sites were retrieved and then redeployed east of the main array as new sites. This practice occurred over the continental United States from 2004-2015, creating the appearance of the array moving discretely eastward over time. The intention was to deploy the sites in a Cartesian-like grid configuration with each station separated by about 70 km.

As described by Shearer (2009), waveforms generated by seismic disturbances propagate with speeds of several (1-15) km s^{-1}, orders of magnitude faster than any of the atmospheric phenomena described previously (generally $\leq$ 70 m s^{-1}). Thus, 70 km platform spacing assessing a “slow” 1 km s^{-1} propagating feature would indicate wave

passage between successive platforms in a span of a little over a minute (70 s). Such a deployment strategy to assess an atmospheric disturbance propagating at 25 m s^{-1} would be the equivalent of having surface stations deployed every 1.75 km. The seismic data collected from the TA sites have led to vast improvements in North American continent subsurface understanding (e.g., Burdick et al. 2008; Burdick et al. 2010).

Initially, atmospheric pressure sensors were not deployed with the TA sites. However, it is known within the seismic discipline that atmospheric-based events can be recorded by seismic measurements. Natural disturbances such as bolide events (Hedlin et al. 2010) and anthropogenic acoustic signals such as sonic booms (de Groot-Hedlin et al. 2008; Hedlin et al. 2012) can impact seismic recordings. Pressure perturbations from natural atmospheric phenomena such as gravity waves have also been recorded by seismometers (de Groot-Hedlin et al. 2014). Physically, this makes sense as the surface should respond in some way to an abrupt change in "atmospheric weight" caused by the passage of such events. Thus, there was a need to better identify these atmospheric signals in the TA seismic data to differentiate them from signals caused by seismic-related processes. This led to the addition of several pressure-based sensors to the platforms beginning in late 2009, including eventual installation of Setra-278 atmospheric pressure sensors. The pressure sensors recorded atmospheric surface pressure at 1 and 40 Hz data intervals (Tytell et al. 2016).

Figure 1.1 depicts the geographic locations where pressure sensors were deployed from 1 Jan 2010 to 22 Jul 2016. Due to the pressure sensors being added roughly half-way through the campaign, only the central and eastern United States was densely sampled. The primary portion of the TA is now being deployed across Alaska and the

adjacent provinces of Canada, where it will remain in place for a few years. Some stations also remain in place across the United States, courtesy of additional funding and the adoption of some platforms by other organizations.

1.3 Objectives

The pressure sensor instrumentation quality, high (relative to most atmospheric equipment) temporal resolution, minimal latency, and uniform distribution of platforms tends to make the TA a potentially rich resource of data for many uses within the atmospheric science community. Initial communication began in 2012 between researchers at the Incorporated Research Institutions for Seismology (IRIS) Data Management Center (DMC) and MesoWest at the University of Utah regarding potential real-time collection of TA pressure data within the atmospheric science realm. Further discussions, which included the Array Network Facility (ANF) at Scripps Institution of Oceanography, University of California, San Diego, led to the writing and funding of an NSF ATM proposal to further look into the TA data from an atmospheric perspective. The research encompassed within this dissertation addresses many of the questions addressed in that proposal as well as the following goals.

First, an initial goal was to further the access and dissemination of the TA data within the atmospheric science community. As stated previously, an initial motivator for this project was to have the TA data accessible and flowing through well-known surface observation channels in the atmospheric sciences such as MesoWest (http://meso-west.utah.edu). However, the configuration of MesoWest does not permit the ability to archive observations at 1 Hz frequency, so provisions are made in collection processes to

reduce TA data to 5-minute averages. As described further in portions of Chapters 2 and 3, the TA data collected by MesoWest are distributed with other mesonet data to organizations within NOAA and other entities for use and potential inclusion in data assimilation services for numerical weather prediction. While MesoWest serves the real-time dissemination purpose, access to the 1-Hz data remained somewhat limited. Chapter 2 describes efforts to collect the 1-Hz data and archive it in accessible and efficient ways for research purposes. Local archives are used to visualize TA 1-Hz observations via a variety of web-based products developed as a part of this project (http://meso1.chpc.utah.edu/usarray/). Further, yearly archives of the data are now available as a dataset within the Research Data Archive at the National Center for Atmospheric Research (http://rda.ucar.edu/datasets/ds386.0/).

Second, the temporal resolution and high data quality of the TA data provided an opportunity to execute time series analyses for each TA site to identify pressure fluctuations induced by mesoscale, subsynoptic, and synoptic processes. Chapter 3 explores this work further, including assessments of how pressure fluctuations vary as a function of location, season, magnitude, and additional metrics. Case examples using time series analysis techniques are shown for phenomena ranging from mesoscale to synoptic-scale, in addition to aggregated statistics for each station over the period of the platform's existence.

Third, the uniform distribution of the TA allows for further exploration of the development and translation of pressure features detected through the time series analyses in Chapter 3. Chapter 4 describes efforts to combine high spatial resolution analysis with TA observations to identify and track translating mesoscale perturbations

such as gravity waves and convective systems. A 6-month period from 1 Mar 2011 – 31 August is shown when prominent mesoscale events occurred within the TA footprint.

Finally, Chapter 5 provides a general review of conclusions from the previous chapters as well as thoughts regarding future work, both in terms of using the TA data for other research-based objectives as well as recommendations to further the assessment of pressure perturbations detected within surface observations.

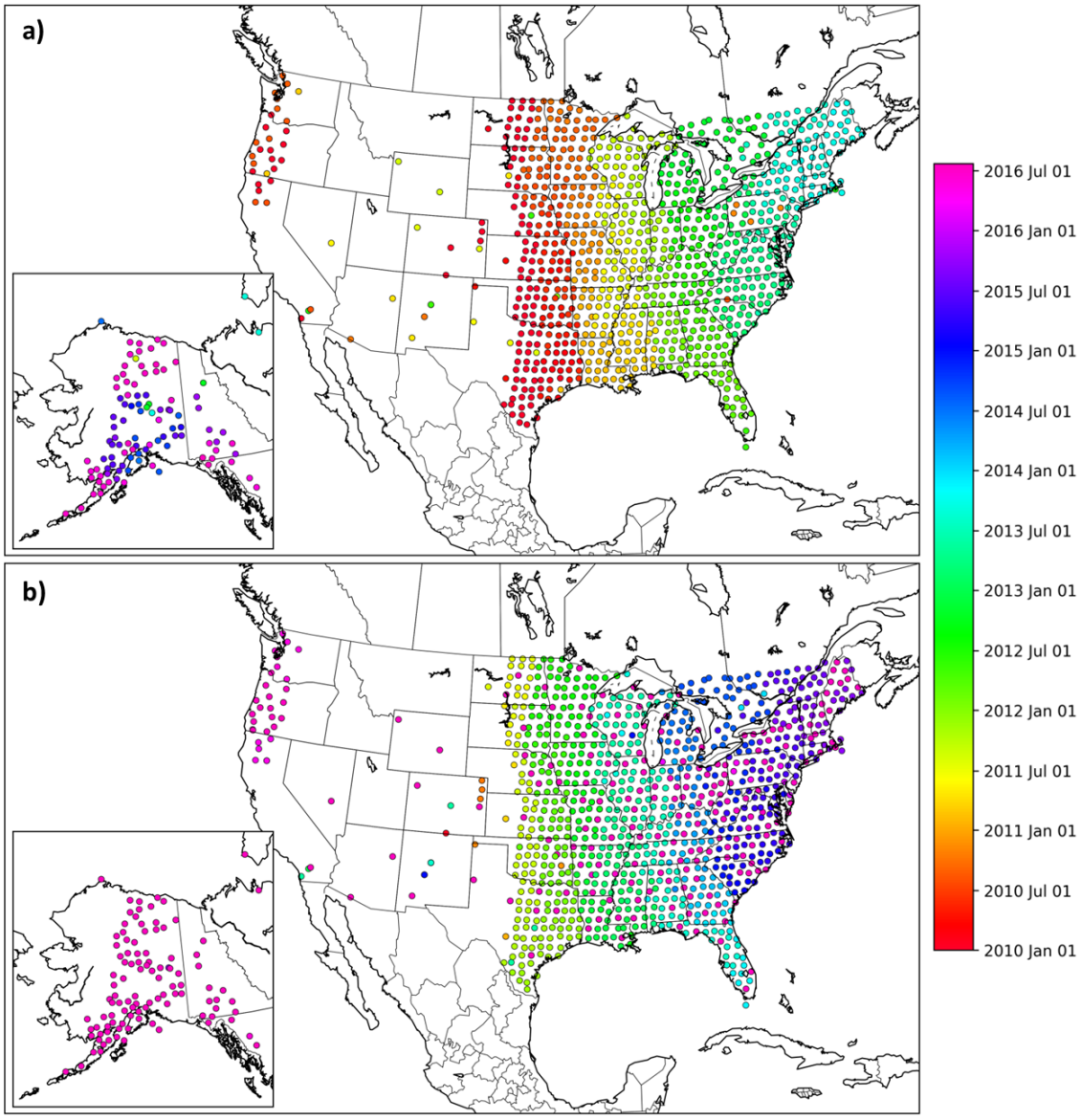

Fig. 1.1. TA platform deployments from 1 Jan 2010 through 22 Jul 2016. Marker color indicates when the station (a) first reported and (b) last reported atmospheric pressure observations. Magenta colors indicate stations likely still deployed and transmitting beyond 22 Jul 2016.

1.4 References

Adams-Selin, R. D., and R. H. Johnson, 2013: Examination of gravity waves associated with the 13 March 2003 bow echo. *Mon. Wea. Rev.*, **141**, 3735-3756.

Alexandersson, H., T. Schmith, K. Iden, and H. Tuomenvirta, 1998: Long-term variations of the storm climate over NW Europe. *Global Atmos. Ocean Syst.*, **6**, 97-120.

Anderson, J. L., B. Wyman, S. Zhang, and T. Hoar, 2005: Assimilation of PS observations using an ensemble filter in an idealized global atmospheric prediction system. *J. Atmos. Sci.*, **62**, 2925-2938.

Bärring, L., and K. Fortuniak, 2009: Multi-indices analysis of southern Scandinavian storminess 1780–2005 and links to interdecadal variations in the NW Europe-North Sea region. *Int. J. Climatol.*, **29**, 373-384.

Bosart, L. F., W. E. Bracken, and A. Seimon, 1998: A study of cyclone mesoscale structure with emphasis on a large-amplitude inertia-gravity wave. *Mon. Wea. Rev.*, **126**, 1497-1527.

Brown, R. A., and V. T. Wood, 2012: The Tornadic Vortex Signature: an update. *Wea. Forecasting*, **27**, 525-530.

Bullock, R., 2011: Development and implementation of MODE time domain object-based verification. Preprints, *24th Conf. on Weather and Forecasting/20th Conf. on Numerical Weather Prediction*, Seattle, WA, Amer. Meteor. Soc., 96. [Available online at https://ams.confex.com/ams/91Annual/webprogram/Paper182677.html.]

Burdick, S., and Coauthors, 2008: Upper mantle heterogeneity beneath North America from travel time tomography with global and USArray Transportable Array data. *Seismological Res. Lett.*, **79**, 384-392.

——, and Coauthors, 2010: Model update January 2010: Upper mantle heterogeneity beneath North America from traveltime tomography with global and USArray Transportable Array data. *Seismological Res. Lett.*, **81**, 689-693.

Carbone, R. E., J. D. Tuttle, D. A. Ahijevych, and S. B. Trier, 2002: Inferences of predictability associated with warm season precipitation episodes. *J. Atmos. Sci.*, **59**, 2033-2056.

Clark, P. A., K. A. Browning, C. J. Morcrette, A. M. Blyth, R. M. Forbes, B. Brooks, and F. Perry, 2014: The evolution of an MCS over southern England. Part 1: Observations. *Quart. J. Roy. Meteor. Soc.*, **140**, 439-457.

Coleman, T. A., and K. R. Knupp, 2009: Factors affecting surface wind speeds in gravity waves and wake lows. *Wea. Forecasting*, **24**, 1664-1679.

—, and K. R. Knupp, 2010: A nonlinear impedance relation for the surface winds in pressure disturbances. *J. Atmos. Sci.*, **67**, 3409-3422.

Davis, C. A., B. Brown, and R. Bullock, 2006: Object-based verification of precipitation forecasts. Part I: Methodology and application to mesoscale rain areas. *Mon. Wea. Rev.*, **134**, 1772-1784.

—, —, —, and J. Halley-Gotway, 2009: The Method for Object-Based Diagnostic Evaluation (MODE) applied to numerical forecasts from the 2005 NSSL/SPC Spring Program. *Wea. Forecasting*, **24**, 1252-1267.

de Groot-Hedlin, C. D., M. A. H. Hedlin, K. Walker, D. P. Drob, and M. Zumberge, 2008: Study of propagation from the shuttle Atlantis using a large seismic network. *J. Acoustic Soc. Amer.*, **124**, 1442-1451.

de Groot-Hedlin, C. D., M. A. H. Hedlin, and K. T. Walker, 2014: Detection of gravity waves across the USArray: A case study. *Earth Planet. Sci. Lett.*, **402**, 346-352.

Dirren, S., R. D. Torn, and G. J. Hakim, 2007: A data assimilation case study using a limited-area ensemble Kalman filter. *Mon. Wea. Rev.*, **135**, 1455-1473.

Ferreira, R. Nieto, L. Hall, and T. M. Rickenbach, 2013: A climatology of the structure, evolution, and propagation of midlatitude cyclones in the southeast United States. *J. Climate*, **26**, 8406-8421.

Fujita, T. T., and H. A. Brown, 1958: A study of mesosystems and their radar echoes. *Bull. Amer. Meteor. Soc.*, **39**, 538-554.

Grivet-Talocia, S., and F. Einaudi, 1998: Wavelet analysis of a microbarograph network. *IEEE Trans. Geosci. Remote Sens.*, **36,** 418-433.

—, —, W. L. Clark, R. D. Dennett, G. D. Nastrom, and T. E. VanZandt, 1999: A 4-yr climatology of pressure disturbances using a barometer network in central Illinois. *Mon. Wea. Rev.*, **127**, 1613-1629.

Hedlin, M. A. H., D. Drob, K. Walker, C. D. de Groot-Hedlin, 2010: A study of acoustic propagation from a large bolide in the atmosphere with a dense seismic network. *J. Geophys. Res.*, **115**, B11312.

Hedlin, M. A. H., C. D. de Groot-Hedlin, D. P. Drob, 2012: A study of infrasound propagation using dense seismic network recordings of surface explosions. *Bull. Seismological Soc. of Amer.*, **102**, 1927-1937.

Hodges, K. I., 1994: A general method for tracking analysis and its application to meteorological data. *Mon. Wea. Rev.*, **122**, 2573-2586.

——, B. J. Hoskins, J. Boyle, and C. Thorncroft, 2003: A comparison of recent reanalysis datasets using objective feature tracking: storm tracks and tropical easterly waves. *Mon. Wea. Rev.*, **131**, 2012-2037.

Horel, J., and Coauthors, 2002: Mesowest: Cooperative mesonets in the western United States. *Bull. Amer. Meteor. Soc.*, **83**, 211-225.

Hoskins, B. J., and K. I. Hodges, 2002: New perspectives on the Northern Hemisphere winter storm tracks. *J. Atmos. Sci.*, **59**, 1041-1061.

Johnson, J. T., P. L. MacKeen, A. Witt, E. D. Mitchell, G. J. Stumpf, M. D. Eilts, and K. W. Thomas, 1998: The Storm Cell Identification and Tracking Algorithm: an enhanced WSR-88D algorithm. *Wea. Forecasting*, **13**, 263-276.

Johnson, R. H., 2001: Surface mesohighs and mesolows. *Bull. Amer. Meteor. Soc.*, **82**, 13-31.

Jones, P. D., Osborn, T. J. and Briffa, K. R., 2003: Pressure-based measures of the North Atlantic Oscillation (NAO): A comparison and an assessment of changes in the strength of the NAO and in its influence on surface climate parameters. *The North Atlantic Oscillation: Climatic Significance and Environmental Impact*, J. W. Hurrell et al., Eds., Amer. Geophys. Union, 173-192.

Jung, S., and G. Lee, 2015: Radar-based cell tracking with fuzzy logic approach. *Meteor. Applications*, **22**, 716-730.

Koch, S. E., and C. O'Handley, 1997: Operational forecasting and detection of mesoscale gravity waves. *Wea. Forecasting*, **12**, 253-281.

——, and S. Saleeby, 2001: An automated system for the analysis of gravity waves and other mesoscale phenomena. *Wea. Forecasting*, **16**, 661-679.

König, W., R. Sausen, and F. Sielmann, 1993: Objective identification of cyclones in GCM simulations. *J. Climate*, **6**, 2217-2231.

Koppel, L. L., L. F. Bosart, and D. Keyser, 2000: A 25-yr climatology of large-amplitude hourly surface pressure changes over the conterminous United States. *Mon. Wea. Rev.*, **128**, 51-68.

Kravtsov, S., I. Rudeva, and S. K. Gulev, 2015: Reconstructing sea level pressure variability via a feature tracking approach. *J. Atmos. Sci.*, **72**, 487-506.

Krueger, O., and H. von Storch, 2012: The informational value of pressure-based single-station proxies for storm activity. *J. Atmos. Oceanic Technol.*, **29**, 569-580.

Lei, L., and J. L. Anderson, 2014: Impacts of frequent assimilation of surface pressure observations on atmospheric analyses. *Mon. Wea. Rev.*, **142**, 4477-4483.

Li, Y., and R. B. Smith, 2010: The detection and significance of diurnal pressure and potential vorticity anomalies east of the Rockies. *J. Atmos. Sci.*, **67**, 2734-2751.

Liu, Y., D. Xi, Z. Li, and C. Shi, 2014: Automatic tracking and characterization of cumulonimbus clouds from FY-2C geostationary meteorological satellite images. *Advances in Met.*, **2014**, 1-18.

Mass, C. F., and L.E. Madaus, 2014: Surface pressure observations from smartphones: A potential revolution for high-resolution weather prediction? *Bull. Amer. Meteor. Soc.*, **95**, 1343-1349.

——, W. J. Steenburgh, and D. M. Schultz, 1991: Diurnal surface-pressure variations over the continental United States and the influence of sea level reduction. *Mon. Wea. Rev.*, **119**, 2814-2830.

McMillen, J. D., 2014: Numerical weather prediction of Great Salt Lake effect precipitation at convection-permitting grid spacings. Doctoral dissertation, Dept. of Atmospheric Sciences, University of Utah. pp. 136

——, and W. J. Steenburgh, 2015: Capabilities and limitations of convection-permitting WRF simulations of lake-effect systems over the Great Salt Lake. *Wea. Forecasting*, **30**, 1711-1731.

Mittermaier, M. P., and R. Bullock, 2013: Using MODE to explore the spatial and temporal characteristics of cloud cover forecasts from high-resolution NWP models. *Met. Applications*, **20**, 187-196.

Mohr, M., 2004: Problems with the mean sea level pressure field over the western United States. *Mon. Wea. Rev.*, **132**, 1952-1965.

Nappo, C., 2002: *An Introduction to Atmospheric Gravity Waves*. International Geophysics Series, Vol. 85. Academic Press. San Diego, CA. 276 pp.

Raible, C. C., P. M. Della-Marta, C. Schwierz, H. Wernli, and R. Blender, 2008: Northern Hemisphere extratropical cyclones: A comparison of detection and tracking methods and different reanalyses. *Mon. Wea. Rev.*, **136**, 880-897.

Ramamurthy, M. K., R. M. Rauber, B. P. Collins, and N. K. Malhotra, 1993: A comparative study of large-amplitude gravity-wave events. *Mon. Wea. Rev.*, **121**, 2951-2974.

Ray, R. D., and S. Poulose, 2005: Terdiurnal surface-pressure oscillations over the continental United States. *Mon. Wea. Rev.*, **133**, 2526-2534.

Reitan, C. H., 1974: Frequencies of cyclones and cyclogenesis for North America, 1951–1970. *Mon. Wea. Rev.*, **102**, 861-868.

Sanders, F., and J. R. Gyakum, 1980: Synoptic-dynamic climatology of the “bomb”. *Mon. Wea. Rev.*, **108**, 1589-1606.

Shearer, P. M., 2009: *Introduction to Seismology*. 2nd Edition. Cambridge University Press. 396 pp.

Souders, M. B., B. A. Colle, and E. K. M. Chang, 2014a: A description and evaluation of an automated approach for feature-based tracking of Rossby wave packets. *Mon. Wea. Rev.*, **142**, 3505-3527.

—, —, —, —, 2014b: The climatology and characteristics of Rossby wave packets using a feature-based tracking technique. *Mon. Wea. Rev.*, **142**, 3528-3548.

Sutherland, B., 2010: *Internal Gravity Waves*. Cambridge University Press. Cambridge, UK. 377 pp.

Thomas, B. C., and J. E. Martin, 2007: A synoptic climatology and composite analysis of the Alberta clipper. *Wea. Forecasting*, **22**, 315-333.

Torrence, C., and G. P. Compo, 1998: A practical guide to wavelet analysis. *Bull. Amer. Meteor. Soc.*, **79**, 61-78.

Tytell J., F. Vernon, M. Hedlin, C. de Groot Hedlin, J. Reyes, B. Busby, K. Hafner, and J. Eakins J, 2016: The USArray Transportable Array as a platform for weather observation and research. *Bull. Amer. Meteor. Soc.*, **97**, 603-619.

Viana, S., E. Terradellas, and C. Yagüe, 2010: Analysis of gravity waves generated at the top of a drainage flow. *J. Atmos. Sci.*, **67**, 3949-3966.

Zishka, K. M., and P. J. Smith, 1980: The climatology of cyclones and anticyclones over North America and surrounding ocean environs for January and July, 1950-77. *Mon. Wea. Rev.*, **108**, 387-401.

CHAPTER 2[1]

THE EARTHSCOPE US TRANSPORTABLE ARRAY 1 HZ SURFACE PRESSURE DATASET

2.1 Abstract

A unique set of high temporal frequency surface atmospheric pressure observations have been collected and archived from a large-scale field campaign in the geosciences. The EarthScope U.S. Transportable Array (USArray TA) consists of approximately 400 deployable surface platforms. Stations were deployed in a Cartesian-like gridded fashion across a section of the contiguous United States for 1-2 year then retrieved and redeployed as new platforms further east. While primarily deployed for seismic measurements, platforms also recorded surface atmospheric pressure. These pressure data, collected and stored at a temporal frequency of 1 Hz, have been made available via the Research Data Archive at the National Center for Atmospheric Research (NCAR) for the time period 1 Jan 2010 - 31 Dec 2015. The 6 years of observations contain data from over 1,000 locations ranging from the central to eastern United States, as well as some platforms in Alaska and the northwest United States. Data were

---

[1] Chapter 2 is reprinted from the following journal article: Jacques, A. A., J. D. Horel, E. T. Crosman, F. L. Vernon, and J. Tytell, 2016: The Earthscope US Transportable Array 1 Hz surface pressure dataset. *Geoscience Data Journal*, **3**, 29-36.

organized as annual station files with supplemental metadata and quality control summary files. Several web-based interfaces are also available to rapidly explore the pressure archive. We describe the available dataset with several prominent atmospheric events shown as usage examples.

2.2 Introduction

Observations of atmospheric pressure remain an important source of information for many disciplines within the field of meteorology. These observations have been a critical piece for identification of weather phenomena at multiple physical scales, as well as understanding common propagation characteristics (e.g., Zishka and Smith 1980; Chenoweth 2014; Ruppert and Bosart 2014). With improved computational power, surface and derived sea-level pressure data have been compared and incorporated into numerical analyses and reanalyses to improve accuracy and depiction of atmospheric events (Whitaker *et al.* 2004; Compo *et al.* 2006; Compo *et al.* 2011). Recent advances in numerical data assimilation techniques have also relied on surface and derived pressure quantities (e.g., pressure tendency) with efforts to improve simulations of mesoscale phenomena (Anderson *et al.* 2005; Ingleby 2014; Lei and Anderson 2014; Madaus *et al.* 2014). Further, measurements of surface pressure lack the common representativeness errors that can affect other atmospheric state variables (e.g., temperature), beyond requiring an accurate elevation above sea level for the site. This broadens the potential to use pressure observations recorded from a wide variety of sources ranging from fixed *in situ* weather stations to mobile phones (Mass and Madaus 2014).

An extensive National Science Foundation (NSF) geoscience field campaign,

known as The EarthScope initiative, has been conducted over the past decade to better understand and map the structural detail underneath the North American continent. One phase of this campaign, called the US Transportable Array Network (USArray TA), involved the temporary deployment of surface platforms in a pseudo-grid formation to provide enhanced information on seismic activity as well as geospatial mapping of the continent itself (Tytell *et al.* 2016). Seismic observations are known to be affected by atmospheric 'signals' including bolide events (Hedlin *et al.* 2010) and human-caused acoustic signals (de Groot-Hedlin *et al.* 2008; Hedlin *et al.* 2012) as well as pressure perturbations from natural atmospheric phenomena such as gravity waves (de Groot-Hedlin *et al.* 2014). As more resources became available to do so, atmospheric pressure sensors recording at high temporal resolution (1 and 40 Hz) were added to the TA platforms to help identify these nonseismic perturbations encountered in the seismic data (Tytell *et al.* 2016).

Surface atmospheric pressure data at such high temporal resolution over an extensive area have not been available before, making these data a unique resource for atmospheric research. Jacques *et al.* (2015) and Tytell *et al.* (2016) illustrate a number of atmospheric applications derived from subsets of the USArray TA pressure dataset. We summarize here, for the USArray TA pressure sensor period of record through 2015, the platform and sensor deployment strategy, sensor metadata and quality control, data format, availability, and additional examples of its use for meteorological applications. Further, we describe an archive of the pressure data set derived from the 1 Hz observations from 1 Jan 2010 – 31 Dec 2015 that is now publicly accessible from the Research Data Archive (RDA) at the National Center for Atmospheric Research

(NCAR). This permanent archive will be updated on an annual basis throughout the remaining lifetime of the TA program.

2.3 Dataset Description and Collection

2.3.1 USArray TA Platforms

The TA deployment methodology consisted of approximately 400-500 platforms, which were placed using a Cartesian-like strategy across a subsection of the contiguous United States (CONUS). Each platform was spaced ~70 km apart from the adjacent sites, forming an array-like appearance when considering all deployments spatially. A single platform recorded and transmitted data in real time for a period of about 1-2 years before being retrieved. After retrieval, a platform would be maintained and repaired, if necessary, and redeployed to a new site along the eastern edge of the TA footprint. From its initial deployment in 2004 through the end of the main CONUS deployment phase in 2015, the TA appeared to 'move' east with time.

Since ~500 pressure sensors began to be added roughly halfway through the project, Figure 2.1 depicts the ~1000 locations for which pressure observations are available primarily from the central CONUS eastward during the 2010-2015 period. A separate array of platforms is in place near the Cascade Mountain Range in the northwest CONUS, while some additional TA stations were adopted by other organizations and remain in place as part of the Central and Eastern United States Network initiative (Tytell *et al.* 2016). The primary portion of the TA is now transitioning from the CONUS to deployment in Alaska and adjacent Canadian provinces with a similar gridded array of platforms to evolve there over the next several years.

Tytell *et al.* (2016) describe a typical TA platform deployment, which consists of a below-surface vault enclosing the seismometer and additional equipment. The atmospheric pressure sensor is placed adjacent to the primary data logger near the top of the vault with tubing extending upward to allow adequate sensor exposure. Most platforms rely on solar power and batteries to power the sensor, logging, and communication systems, which allow CONUS stations to transmit data in real-time with minimal latency.

Three types of pressure sensors were typically installed on each platform: infrasound microphones for very high frequency (0.1-100 Hz) pressure perturbations as well as Micro-Electro-Mechanical (MEMS) and Setra-278 pressure sensors. As described by Jacques *et al.* (2015), the more expensive Setra-278 is the preferred sensor for our uses due to its superior performance characteristics. The Setra-278 sensors provide an accuracy of 0.5-1.0 hPa, resolution of 0.01 hPa, and long-term stability of 0.1 hPa $year^{-1}$. The MEMS sensors provide similar metrics of 1.5 hPa accuracy, 0.015 hPa resolution, and 1.0 hPa $year^{-1}$ stability (Jacques *et al.* 2015). The combination of good accuracy and stability of the Setra-278 sensor with the relatively short lifetime of equipment deployment per site provide added confidence in data quality. Sensors were recalibrated or replaced as necessary, typically when a platform was retrieved from its previous location to eventually be redeployed. Data from MEMS sensors are used to fill in any small gaps and complete the data archives when Setra-278 data are unavailable.

Seismic and pressure data are collected in real time and stored in repositories hosted by the Incorporated Research Institutions for Seismology (IRIS) Data Management Center (Tytell *et al.* 2016). For the data archive described here, 1 Hz

surface pressure observations have been collected daily from IRIS and stored at the University of Utah after initially backfilling to begin the archive on 1 Jan 2010. Data are requested from IRIS after a 2-day delay to minimize data loss arising from real-time communication or data transfer issues between the platforms and IRIS.

2.3.2 Data Quality Control and Platform Uptime

As described by Tytell *et al.* (2016), analysts at Scripps Institution of Oceanography review and quality control all data collected from the TA platforms with weekly quality control reports available to researchers. An additional objective pressure rate-of-change check of 2 hPa s^{-1} has been applied as well as subjective reviews of the platform time series for spurious observations, in particular those with a rate-of-change greater than 2 hPa min^{-1} (Jacques *et al.* 2015). Subjective reviews of altimeter-corrected pressure observations were also executed to assist in confirmation that the platform's listed elevation above sea level was correct. Observation time periods that either fail the objective rate-of-change check or the subjective checks indicated above are then flagged as suspect. Time ranges within which platform observations may be suspect are recorded within the quality control summary dataset.

Over 68 billion surface pressure observations were collected from 1064 locations during the period 1 Jan 2010–31 Dec 2015 (Table 2.1). The typical (median) station recorded 99.79% of its possible pressure values with a small loss (order 0.1%) arising from the quality control procedures in place. Hence, high quality pressure observations are available nearly continuously from an overwhelming majority of the platforms. At any one time, a very small number of platforms may be experiencing sensor problems

(e.g., plugged inlet tubing) or loss of power.

2.4 RDA Data Archive

Hierarchal Data Format Version 5 (HDF5) was selected in order to handle the high temporal frequency and volume of this dataset. This open and extensible format, designed for use with large and complex scientific datasets, not only can minimize storage space but also maximize access speed. Approximately two yearly HDF5 files per station have been created since platforms were typically deployed at each location for 2 years (Table 2.1). The Python scripting language and PyTables hierarchal data format module were used to create the HDF5 repository from the data obtained from IRIS.

Data are stored using a table-based concept for a defined node within the HDF5 file. Observational tables contain rows for each observation, with columns denoting the valid observation timestamp (integer epoch seconds) and surface pressure (hPa). Each data file also contains descriptors for each table column and platform metadata, including a numeric station identifier, station character identifier (e.g., H62A), latitude, longitude, and elevation above sea level. Finally, a sortable index is associated with the timestamp column to decrease the time required to read data over a time range.

Level 7 Z-Lib compression was applied to each HDF5 file to reduce disk space, yet allow for fast querying without the need to uncompress the entire file. A complete annual station file, which may contain over 30 million observations, requires only 40 Mb. For the 3075 annual data HDF5 files, only 85 Gb of disk space are required (Table 2.1).

Metadata and quality control summary files corresponding to each annual data file also rely on HDF5. Records in the metadata, quality control, and data files are related to

one another through the numeric and character station identifiers. The metadata summary files contain geolocation and period of record information for each platform. Annual quality control summaries for each platform contain those temporal ranges within which observational data may be suspect as a function of the quality control type. Although at this time there is only one set of tests (see Section 2.3.2), future annual data files may be subject to additional tests applied to the data beyond 31 Dec 2015.

The archive of these pressure data maintained at the University of Utah has also been placed in the RDA repository and made accessible to the public utilizing RDA resources (http://rda.ucar.edu/datasets/ds386.0/). This archive contains all TA pressure observations, platform metadata, and quality control summaries from 1 Jan 2010 to 31 Dec 2015. Registered users of the RDA can utilize web-based interfaces to explore the available archive geographically and temporally. Further, a dataset citation service is also provided by the RDA which allows users to build proper dataset citations when downloading and accessing data from the archive. Annual updates for the RDA archived dataset with new data, metadata, and quality control summaries beyond 31 Dec 2015 are planned as the TA continues to transition into Alaska.

2.5 Utilizing the Pressure Archive

As part of the research described by Jacques *et al.* (2015), a website has been developed and maintained to visualize the TA pressure data in addition to other atmospheric data. These resources are particularly useful to discover locations and periods when atmospheric pressure perturbations may be of interest to a user before downloading data from the archive available from the RDA. The website

(http://meso1.chpc.utah.edu/usarray) provides time series and maps of surface pressure and a number of derived quantities obtained from the surface pressure data (e.g., altimeter pressure and pressure perturbations within specific temporal bands).

These web interfaces access the archive at the University of Utah as well as a more restricted amount of real-time 1 Hz TA pressure data available from IRIS. Observations can be plotted with respect to surface wind observations courtesy of MesoWest (Horel *et al.* 2002) as well as the Iowa Environmental Mesonet Web Map Service (WMS) national composite radar reflectivity imagery. Efficient querying within the HDF5 files has made it possible to interactively plot, for example, time series of lengths up to 45 days within the time of a typical web browser loading sequence. By default, the web tools mask observations deemed suspect by the quality control procedures, although the masking can be deactivated to view the raw data.

Many users may not require the high temporal frequency of the pressure data available from the RDA and, hence, would prefer not to have to download all the data in order to process them into time-averaged values. TA pressure observations have already been processed in real-time into 5-min average values and archived in databases as part of MesoWest at the University of Utah (Horel *et al.* 2002). The observations are available and can be accessed with other meteorological surface observations collected by MesoWest through interactive web tools (http://mesowest.utah.edu) and API services (http://synopticlabs.org/api). Those 5-min averages have also been disseminated in near-real time routinely to the National Weather Service via the Meteorological Automated Data Ingest System and thereby distributed further to the National Centers for Environmental Prediction for use in operational numerical weather prediction and other

applications.

2.6 Visualizing the Pressure Archive Resources

As shown by Jacques *et al.* (2015) and Tytell *et al.* (2016), the TA data archive is a very useful resource for examining pressure signatures from mesoscale events for which conventional pressure observations may lack sufficient temporal resolution to resolve them. For example, consider the well-defined mesoscale convective system in Figure 2.2 with a prominent bowing feature evident from radar reflectivity at 2220 UTC 23 Jun 2015 approaching TA station P61A (Hammonton, NJ) at that time. The time series of surface pressure available from that station (Figure 2.3a) has a well-defined sharp pressure rise associated with the passage of the mesoscale convective system. However, the transect time and magnitude of the pressure rise becomes distorted when observations are sampled at intervals longer than 5 min (Figures 2.3c-d), which are still commonplace with many real-time conventional observation networks.

TA surface pressure can also be used effectively to assess larger-scale meteorological phenomena as well, as shown in Figure 2.4. The TA platforms were deployed near the eastern coast of North Carolina during 4 July 2014 at the time of the landfall of Hurricane Arthur. Arthur reached the North Carolina coastline as a Category 2 hurricane with a minimum central pressure of 973 hPa (Berg, 2015). As the hurricane strengthened and made landfall shortly after 0300 UTC 4 July 2014, its center passed directly over TA station V62A (Hyde County Airport, NC) between 0630 to 0700 UTC. Figure 2.5 depicts altimeter-corrected pressure time series for V62A and the three adjacent TA sites U61A (Possum Corner Farms, NC), V61A (Roper, NC), and W61A

(Ground Anchor Farm, NC), located directly to its west. Strong pressure gradients can be seen both spatially (Figure 2.4c) and temporally (Figure 2.5), with a minimum altimeter setting of 975.2 hPa occurring around 0650 UTC 4 July 2014 at V62A, slightly higher than the minimum central pressure recorded from the storm at peak intensity. Altimeter-corrected observations at that time from the surrounding stations were calculated to be 1006.1, 1000.0, and 1004.6 hPa, respectively. Jacques *et al.* (2015) provides an additional large-scale example of TA data use for a rapidly strengthening northeastern CONUS snowstorm on 13-15 February 2014. These examples demonstrate that the TA can be a potentially valuable additional resource to conventional observations for assessing both the spatial scale and spatial gradients of larger-scale atmospheric phenomena.

2.7 Summary

Surface pressure observations originating from a long-term geoscience field campaign have been collected and made available in a variety of forms for atmospheric scientists. Observations at 1 Hz temporal frequency were collected from over 1,000 different platforms deployed at various periods from 1 Jan 2010 to 31 Dec 2015 as part of the USArray TA initiative. At any given time 400-500 platforms were deployed in a Cartesian-grid configuration. The retrieval and redeployment of platforms along the eastern edge of the primary array resulted in stations being located across the CONUS Central Plains (2010-2011), Ohio Valley to the Gulf Coast (2012-2013), and finally along the East Coast (2014-2015). Each platform recorded approximately 1-2 years of pressure observations with high reliability and data quality (Table 2.1).

A complete archive of these data, metadata, and quality control summaries have been made available via the RDA. Data are organized into annual station time series files using HDF5 for data compression and fast time series querying. In order to obtain quick looks at the information available in the RDA, the 1 Hz data are also accessible graphically as time series and maps (http://meso1.chpc.utah.edu/usarray) as well as 5 min averages in the MesoWest web (http://mesowest.utah.edu) and API services (http://synopticlabs.org/api).

A new phase of the TA is now underway in Alaska, with many platforms now providing data (Figure 2.1). Final deployments in Alaska are expected in 2017 as a similar gridded array is completed there. We intend to continue collecting the 1 Hz pressure data courtesy of IRIS as long as pressure observations are available. These data will continue to be appended to the 1 Hz archives at the University of Utah as well as made available as 5-min averages via MesoWest. The RDA archive is planned to be updated annually with new observations, metadata, and quality control metrics.

2.8 Acknowledgements

Funding for this project was through the National Science Foundation Grant 1252315. TA data collection and access has been provided by the Incorporated Research Institutions of Seismology and the Array Network Facility at Scripps Institution of Oceanography, University of California San Diego. This material is based upon work supported by the Incorporated Research Institutions for Seismology under their Cooperative Agreement No. EAR-1261681 with the National Science Foundation. WMS radar imagery was courtesy of the Iowa Environmental Mesonet web services. The

authors thank the University of Utah Center for High Performance Computing (CHPC) for computational hardware and software, as well as hosting web services and local data archives.

Table 2.1. USArray TA metrics derived from the dataset archived within the NCAR RDA. Metrics are valid for data available from 1 Jan 2010 - 31 Dec 2015.

Description	**Quantity**
Total Platforms	1064
Total Annual Data Files	3075
Total 1 Hz Observations	68,537,083,579
Total HDF5 Repository Disk Space	~85 Gb
Median Station Reporting Period	662.6 days
Median Station Observations Reported	57,253,228
Median Station Uptime (recorded/expected observations)	99.79%
Median Station Data - Passed Quality Control (good/expected)	99.68%

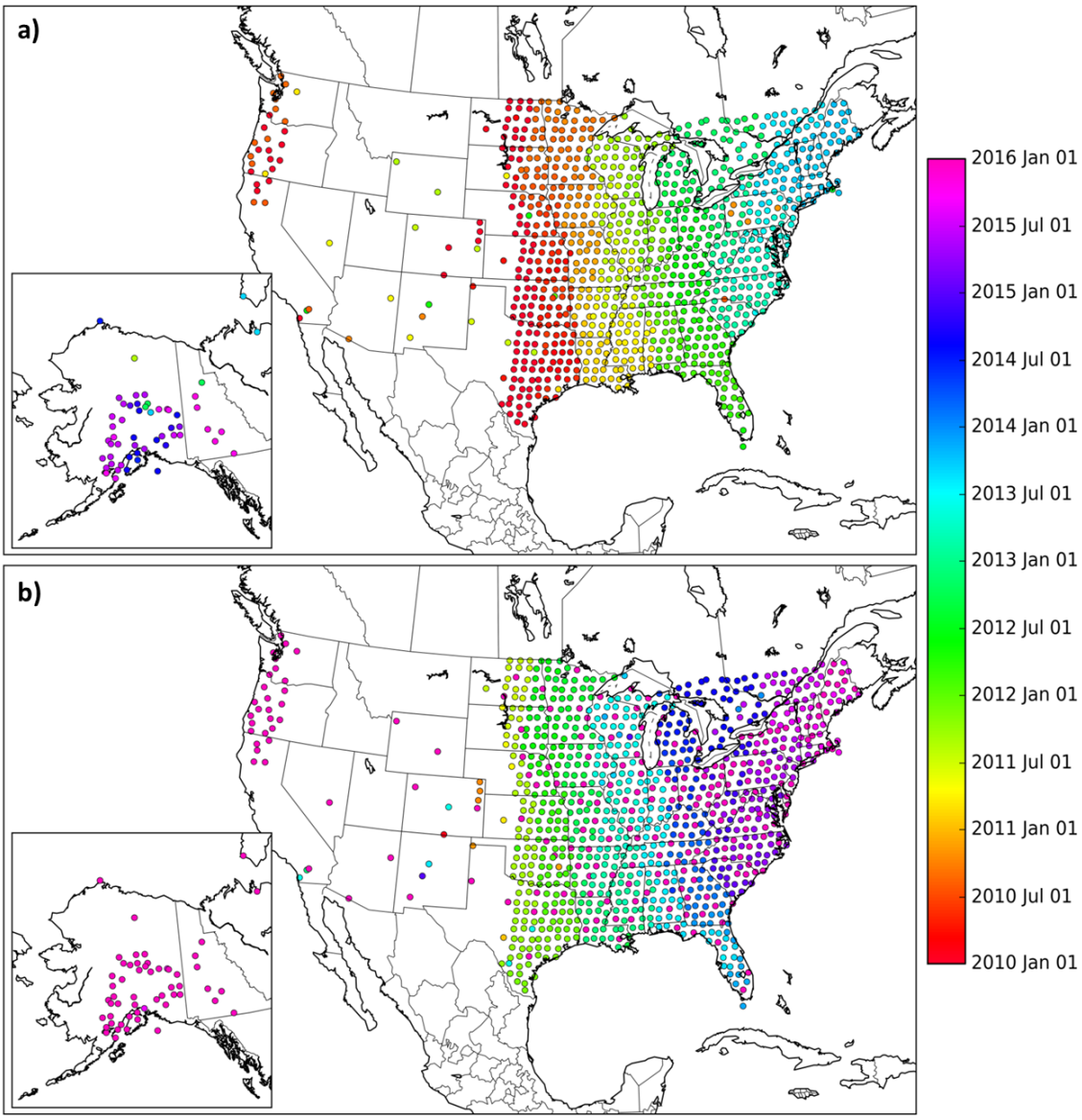

Fig. 2.1. USArray TA station deployments from 1 Jan 2010 through 31 Dec 2015. Marker color indicates when the station (a) first transmitted data and (b) last transmitted data. Magenta colors indicate stations likely still deployed and transmitting beyond 31 Dec 2015.

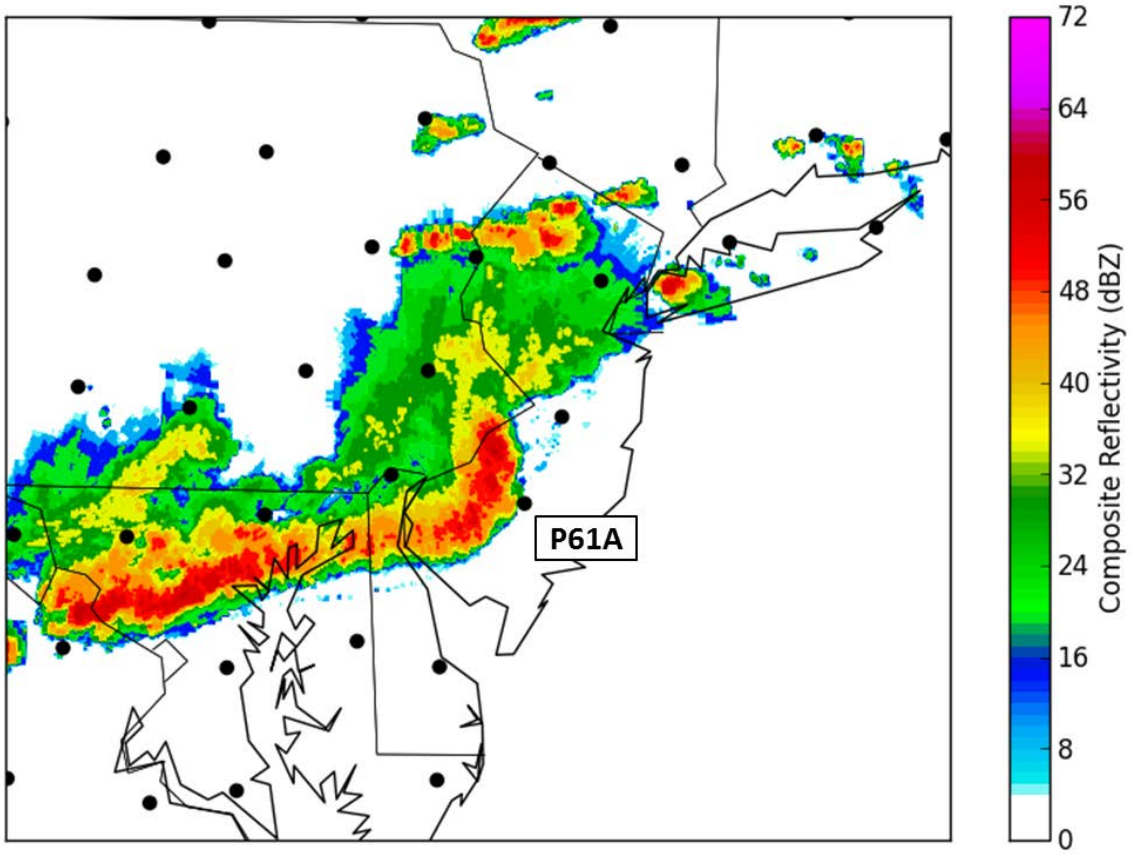

Fig. 2.2. Base radar reflectivity centered on New Jersey at 2220 UTC 23 Jun 2015. Active TA stations are shown as black markers with station P61A (Hammonton, NJ) labeled for reference to Fig 2.2. Reflectivity imagery courtesy the Iowa Environmental Mesonet web services.

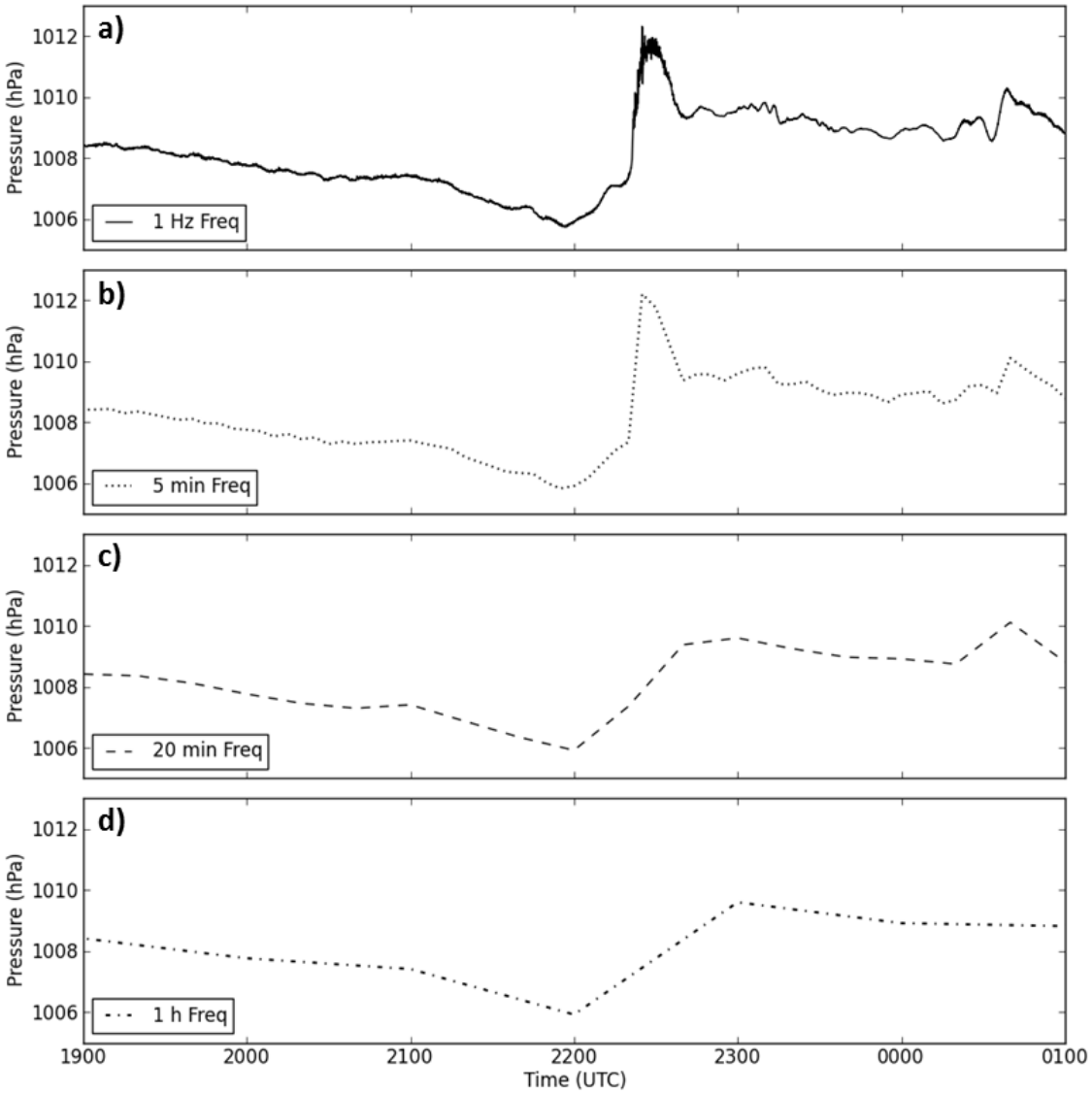

Fig. 2.3. Pressure time series data recorded by TA station P61A (Hammonton, NJ) from 1900 UTC 23 Jun to 0100 UTC 24 Jun 2015. Data shown at sampling frequencies of (a) 1 Hz, (b) 5 min, (c) 20 min, and (d) hourly.

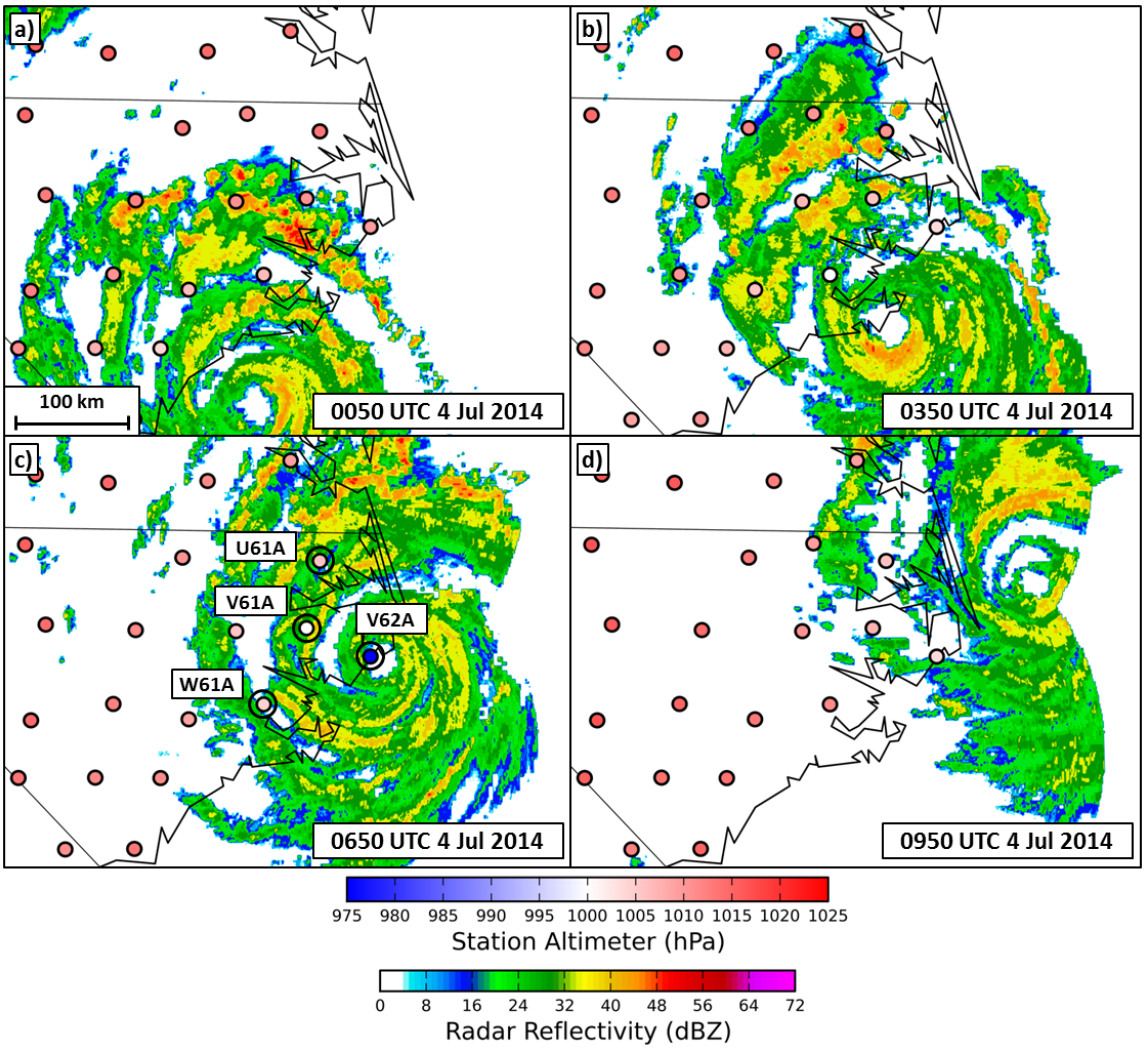

Fig. 2.4. Transect of Hurricane Arthur across coastal North Carolina at (a) 0050, (b) 0350, (c) 0650, and (d) 0950 UTC 4 July 2014. TA altimeter-corrected pressure observations are shown as colored markers with blue (red) indicating lower (higher) pressure, with relevant stations shown in Fig. 2.5 circled and labeled in (c). Radar reflectivity imagery also displayed courtesy of the Iowa Environmental Mesonet Web Map Services.

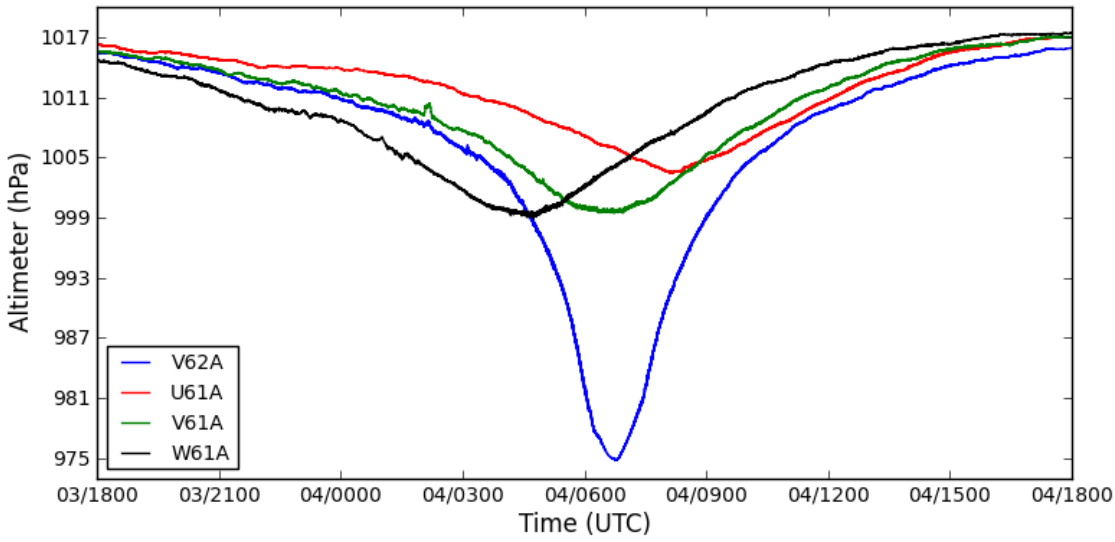

Fig. 2.5. Altimeter-corrected time series plots of TA data from stations V62A (Hyde County Airport, NC - blue), U61A (Possum Corner Farms, NC - red), V61A (Roper, NC - green), and W61A (Ground Anchor Farm, NC - black) during the transect of Hurricane Arthur (1800 UTC 3 July - 1800 UTC 4 July 2014). See Fig 2.4 for TA spatial location reference.

2.9 References

Anderson, J. L., B. Wyman, S. Zhang, and T. Hoar, 2005: Assimilation of surface pressure observations using an ensemble filter in an idealized global atmospheric prediction system. *J. Atmos. Sci.*, **62**, 2925-2938.

Berg, R., cited 2016: National Hurricane Center Tropical Cyclone Report: Hurricane Arthur (AL012014) 1-5 July 2014. [Available online at http://www.nhc.noaa.gov/data/tcr/AL012014_Arthur.pdf.]

Chenoweth, M., 2014: A new compilation of north Atlantic tropical cyclones, 1851-98*. *J. Climate*, **27**, 8674-8685.

Compo, G. P., J. S. Whitaker, and P. D. Sardeshmukh, 2006: Feasibility of a 100-year reanalysis using only surface pressure data. *Bull. Amer. Meteor. Soc.*, **87**, 175-190.

—, and Coauthors, 2011: The Twentieth Century Reanalysis Project. *Quart. J. Royal Met. Soc.*, **137**, 1-28.

de Groot-Hedlin, C. D., M. A. H. Hedlin, K. Walker, D. P. Drob, and M. Zumberge, 2008: Study of propagation from the shuttle Atlantis using a large seismic network. *J. Acoustic Soc. Amer.*, **124**, 1442-1451.

—, —, —, 2014. Detection of gravity waves across the USArray: A case study. *Earth Planet. Sci. Lett.*, **402**, 346-352.

Hedlin, M. A. H., D. Drob, K. Walker, and C. D. de Groot-Hedlin, 2010: A study of acoustic propagation from a large bolide in the atmosphere with a dense seismic network. *J. Geophys. Res.*, **115**, B11312.

Hedlin, M. A. H., C. D. de Groot-Hedlin, and D. P. Drob, 2012: A study of infrasound propagation using dense seismic network recordings of surface explosions. *Bull. Seismological Soc. of Amer.*, **102**, 1927-1937.

Horel, J., and Coauthors, 2002: Mesowest: Cooperative mesonets in the western United States. *Bull. Amer. Meteor. Soc.*, **83**, 211–225.

Ingleby, B., 2014: Global assimilation of air temperature, humidity, wind and pressure from surface stations. *Quart. J. Roy. Meteor. Soc.*, **141**, 504-517.

Jacques, A. A., J. D. Horel, E. T. Crosman, and F. L. Vernon, 2015: Central and eastern United States surface pressure variations derived from the USArray network. *Mon. Wea. Rev.*, **143**, 1472-1493.

—, —, —, —, 2016: EarthScope USArray Transportable Array (TA) Surface Pressure Observations Sampled at 1 Hz Frequency. *Research Data Archive at the National Center for Atmospheric Research, Computational and Information Systems Laboratory, Boulder, Colorado, USA*. doi:10.5065/D6028PRS

Lei L., and J. Anderson, 2014: Impacts of frequent assimilation of surface pressure observations on atmospheric analyses. *Mon. Wea. Rev.*, **142**, 4477-4483.

Madaus, L. E., G. J. Hakim, and C. F. Mass, 2014: Utility of dense pressure observations for improving mesoscale analyses and forecasts. *Mon. Wea. Rev.*, **142**, 2398-2413.

Mass, C. F., and L.E. Madaus, 2014: Surface pressure observations from smartphones: A potential revolution for high-resolution weather prediction? *Bull. Amer. Meteor. Soc.*, **95**, 1343-1349.

Ruppert, J. H., and L. F. Bosart, 2014: A case study of the interaction of a mesoscale gravity wave with a mesoscale convective system. *Mon. Wea. Rev.*, **142**, 1403-1429.

Tytell, J., F. Vernon, M. Hedlin, C. de Groot Hedlin, J. Reyes, B. Busby, K. Hafner, and J. Eakins, 2016: The USArray Transportable Array as a platform for weather observation and research. *Bull. Amer. Meteor. Soc.*, **97**, 603-619.

Whitaker, J. S., G. P. Compo, X. Wei, and T. M. Hamill, 2004: Reanalysis without radiosondes using ensemble data assimilation. *Mon. Wea. Rev.*, **132**, 1190-1200.

Zishka, K. M., and P. J. Smith, 1980: The climatology of cyclones and anticyclones over North America and surrounding ocean environs for January and July, 1950-77. *Mon. Wea. Rev.*, **108**, 387-401.

CHAPTER 3[2]

CENTRAL AND EASTERN U.S. SURFACE PRESSURE VARIATIONS DERIVED FROM THE USARRAY NETWORK

3.1 Abstract

Large-magnitude pressure signatures associated with a wide range of atmospheric phenomena (e.g., mesoscale gravity waves, convective complexes, tropical disturbances, and synoptic storm systems) are examined using a unique set of surface pressure sensors deployed as part of the National Science Foundation EarthScope USArray Transportable Array. As part of the USArray project, approximately 400 seismic stations were deployed in a pseudo-grid fashion across a portion of the United States for 1-2 yr, then retrieved and redeployed farther east. Surface pressure observations at a sampling frequency of 1 Hz were examined during the period 1 January 2010 to 28 February 2014 when the seismic array was transitioning from the central to eastern continental United States. Surface pressure time series at over 900 locations were band-pass filtered to examine pressure perturbations on three temporal scales: meso (10 min - 4 h); subsynoptic (4 - 30 h); and synoptic (30 h - 5 days).

---

[2] Chapter 3 is reprinted from the following journal article: Jacques, A. A., J. D. Horel, E. T. Crosman, and F. L. Vernon, 2015: Central and eastern United States surface pressure variations derived from the USArray network. *Mon. Wea. Rev.*, **143**, 1472-1493.

Case studies of strong pressure perturbations are analyzed using web tools developed to visualize and track tens of thousands of such events with respect to archived radar imagery and surface wind observations. Seasonal assessments of the band-pass filtered variance and frequency of large-magnitude events are conducted to identify prominent areas of activity. Large-magnitude mesoscale pressure perturbations occurred most frequently during spring in the southern Great Plains and shifted northward during summer. Synoptic-scale pressure perturbations are strongest during winter in the northern states, with maxima located near the east coast associated with frequent synoptic development along the coastal storm track.

3.2 Introduction

Large-amplitude surface pressure perturbations are produced by a wide variety of high-impact atmospheric phenomena (Koppel et al. 2000; Nappo 2002; Sutherland 2010). Measurements of surface barometric pressure have been used to identify and follow propagating atmospheric systems on spatial and temporal scales ranging from turbulence (e.g., Viana et al. 2010) to multiyear oscillations (e.g., Jones et al. 2003). As summarized by Mass and Madaus (2014), surface pressure observations have fewer siting and measurement issues than observations of temperature or wind. Surface pressure is also more readily assimilated into research and operational models (Whitaker et al. 2004; Dirren et al. 2007; Wheatley et al. 2010). As discussed by Madaus et al. (2014), assimilating densely spaced surface pressure observations shows promise for improving future mesoscale analyses and forecasts.

Numerous studies have relied on pressure observations to catalogue and examine

meteorological events. Sea-level pressure analyses derived from surface pressure observations have often been used to produce climatologies of synoptic storm tracks (Reitan 1974; Zishka and Smith 1980). More recent climatologies of synoptic storm tracks rely on pressure data derived from numerical model reanalyses (Thomas and Martin 2007; Nieto Ferreira et al. 2013). Pressure tendency (i.e., the change in pressure over a specified duration) has been used frequently to identify preferred geographical locations for cyclogenesis and anticyclogenesis (Sanders and Gyakum 1980; Krueger and von Storch 2012).

While the pressure perturbations associated with internal waves are often viewed as noise for large-scale weather systems (Sutherland 2010), an extensive literature base exists on the theoretical, observational, and modeling aspects of pressure perturbations resulting from a wide array of physical processes. The highest impact pressure perturbations occurring over space and time scales less than those of large weather disturbances are usually gravity waves associated with intense convection, and many analyses of the spatiotemporal evolution of these waves have occurred in the last several decades following T. Fujita's mesoanalyses of barograph traces using time-to-space data reduction techniques (Fujita and Brown 1958; Koch and Saleeby 2001; Johnson 2001). However, as reviewed by Wei and Zhang (2014), gravity waves and their associated pressure perturbations can also result from topographic effects, density gradients, shear instabilities, and geostrophic adjustments. In addition to gravity waves, localized or regional pressure gradients are also generated by mesoscale high and low pressure disturbances, differential heating of land surfaces, diurnal tides, and persistent flow over terrain.

The overlapping temporal scales within which these pressure perturbations and associated phenomena occur include the following:

- Less than 20 min: high-frequency internal gravity waves resulting from shear layers, horizontal convective rolls, katabatic flows, and other boundary-layer phenomena (Tian et al. 2004; Adams-Selin and Johnson 2010; Viana et al. 2010)
- 5 min - 4 h: propagating gravity waves associated with individual convective storms and associated cold pools, mesohighs and wake lows, bow echoes, derechos, and other mesoscale disturbances (Crook 1988; Engerer et al. 2008; Metz and Bosart 2010)
- 2-12 h: differential heating of land and water surfaces (Novak and Colle 2006), elevated terrain (Geerts et al. 2008), long-lived mesoscale gravity waves and inertia-gravity waves, cold fronts, or dry lines associated with large synoptic disturbances (Jewett et al. 2003; Bosart et al. 1998), or prolonged flow over a topographic barrier (Gaberšek and Durran 2006)
- 12-24 h: Diurnal and semidiurnal migrating thermal tides due to diurnal heating (Dai and Wang 1999; Li and Smith 2010).

While many of the phenomena mentioned above tend to occur largely unnoticed, large-amplitude gravity waves, wake lows, and other mesoscale convective systems (MCS) leading to severe weather have received much attention during recent decades (Ramamurthy et al. 1993; Coleman and Knupp 2009; Coleman and Knupp 2010; Adams-Selin and Johnson 2013). A mix of microbarograph traces and pressure observations at hourly or longer intervals have been the most common tools available to study such events (Bosart et al. 1998).

While extensive research has been conducted regarding the dynamics and evolution of specific high-impact, long-lived mesoscale gravity wave events, relatively few studies have looked at the occurrence of pressure perturbations over broader spatial and temporal scales. Koppel et al. (2000) conducted a 25-yr climatology of large pressure perturbations over the conterminous United States, but were limited by 1 h sampling intervals, which likely underestimated the frequency of occurrence of these features. Figure 3.1 illustrates the importance of sampling pressure perturbations at high frequency for a large-amplitude gravity wave event on 17 April 2013 for which sampling at 20 min or 1 h intervals fails to capture the primary wave signature.

Various signal processing techniques have been relied upon to isolate discrete or recurring pressure perturbations. Harmonic analysis has been utilized to determine the magnitude and phase of the diurnal, semidiurnal, and terdiurnal cycles (Mass et al. 1991; Ray and Poulose 2005; Li and Smith 2010). Band-pass filtering techniques were utilized by Koch and O'Handley (1997) as well as Koch and Saleeby (2001) to isolate pressure perturbations coincident with mesoscale gravity waves using pressure observations at 5 min intervals, which, as shown in Fig. 3.1, provide a reasonable reconstruction of gravity waves in pressure time series. Wavelet analysis techniques to extract discrete events in time and space are common as well (Grivet-Talocia and Einaudi 1998; Grivet-Talocia et al. 1999). However, wavelet techniques rely on specifying the expected pressure fluctuation pattern to cast as the mother wavelet, which is difficult to define generally (Torrence and Compo 1998).

This research takes advantage of the deployment beginning in 2010 of pressure sensors on the National Science Foundation sponsored EarthScope USArray

Transportable Array (TA; Tytell et al. 2011; Vernon et al. 2011; Vernon et al. 2012). Very high temporal resolution (1 Hz) surface pressure data for roughly 2-yr periods are available at stations separated by ~70 km in the central and eastern portions of the United States and southern Canada. An extensive set of web tools have been developed to interactively examine these data (see http://meso1.chpc.utah.edu/usarray/).

The objective of this study is to analyze the frequency and amplitude of pressure perturbations as a function of location and season at each TA observing site. Band-pass filters applied to the pressure data allow large-amplitude mesoscale, subsynoptic, and synoptic pressure signatures to be examined. Case studies of high-impact events demonstrate the capabilities of the TA 1-Hz pressure surface pressure network to capture the relevant spatiotemporal evolution of these events.

3.3 Data and Methods

3.3.1 USArray TA Surface Pressure Observations

The USArray TA in situ network was developed as part of an EarthScope project to study seismic activity across the continental United States (Yang and Ritzwoller 2008; Pavlis et al. 2012). The project began in 2004 with stations placed across the western United States using a pseudogrid concept, with average spacing of about 70 km between locations. Stations report for a period of 1-2 yr, then are retrieved and redeployed as new stations east of the existing grid. This method of station deployment and retrieval produces a temporal “rolling appearance” of the array over several years. While only seismic sensors were installed as the array progressed from the Pacific coastline across the west, atmospheric pressure sensors were added to stations that were redeployed over

the central United States beginning in 2010 (Fig. 3.2). As described by de Groot-Hedlin et al. (2014), stations were initially equipped with less expensive Micro-Electro-Mechanical (MEMS) pressure sensors (0.015 hPa resolution; 1.5 hPa accuracy; 1.0 hPa per yr stability). Additional Setra-278 barometric pressure sensors (0.01 hPa resolution; 0.5-1.0 hPa accuracy; 0.1 hPa per yr stability) were installed from late 2010 into 2011. Both sensors were enclosed within the main vault of the station that was placed slightly underground for seismometer housing, with tubing extending from the sensors to the surface to allow for adequate sampling of the atmospheric pressure. Readings from the MEMS pressure sensors were initially fetched until the Setra-278 units were installed, with Setra-278 observations taking priority over the MEMS once they were active due to their better accuracy, resolution, and long-term stability.

The combination of high-resolution and fast response time allows the pressure measurements to be collected at high sampling rates (including 1 and 40 Hz) for seismic applications. Real-time communications allow the observations to be received by the Scripps Institution of Oceanography Array Network Facility (ANF) and then transmitted to the Incorporated Institutions of Seismology (IRIS) with minimal latency. Through the IRIS web service products, 1-Hz pressure observations from 1 January 2010 to the present have been retrieved for all USArray stations.

Figure 3.2 depicts the first and last date within the 1 January 2010 to 28 February 2014 window during which pressure observations were available for this study at the over 900 unique station locations. In general, stations across the central United States were active during 2010-2011, the upper Midwest and southeast from late 2011 to early 2013, and further east toward New England and southern Canada from 2013-2014. Since 1

March 2012, the 1-Hz data have been processed into 5-min averages, made available publicly with minimal latency via MesoWest (Horel et al. 2002), and transmitted via the NOAA Meteorological Automated Data Ingest System (MADIS) to National Weather Service (NWS) field offices and the National Centers for Environmental Prediction (NCEP) for nowcasting and operational numerical weather prediction.

3.3.2 Quality Control

Several steps were employed to flag the small amount of erroneous 1-Hz pressure data and to avoid introducing spurious signals resulting from filtering across data gaps. First, periods of missing data exceeding 5 min were identified and no interpolation was performed to fill in those missing periods. Second, large pressure signals not plausible for atmospheric phenomena of interest in this study were identified. For example, short duration power outages, pressure sensor "warm-up" signatures, and external siting factors occasionally produced large discontinuous changes. Pressure changes exceeding 2 hPa s^{-1} were immediately flagged as suspect, while rates exceeding 2 hPa min^{-1} required further subjective examination on a case by case basis. Although pressure change rates exceeding these thresholds could occur as a result of extreme local weather events (e.g., tornadoes or dust devils), sampling such events would be extremely rare, given the large horizontal spacing of the sensor array. Third, bulk statistics (range, variance, etc.) for each station time series over seasonal and annual periods were examined for both pressure and derived altimeter setting using available elevation metadata. Seasons were defined as December-January-February (DJF), March-April-May (MAM), June-July-August (JJA), and September-October-November (SON) periods. These statistics helped

to identify stations with problems ranging from improper installation, sensor programming (voltage multiplier or offset issues), or metadata inaccuracies. Finally, subjective quality control was required for some blatantly spurious pressure signals that were not flagged by the objective procedures.

Table 3.1 provides summary statistics for the total number of 1-Hz observations collected and quality control of the 1-Hz data from 1 January 2010 to 28 February 2014. Over 48 billion observations were collected during this time period. Stations had very little missing data, with a median loss of only 0.17% of the possible observations per station. The quality control procedures flagged a total of 2.39% of the 1-Hz data, the majority from a few problematic stations or stations that had extended periods of sensor problems that required maintenance. For example, heavy rain events in some instances led to water infiltrating the inlet tubes to the pressure sensors, resulting in wild, unphysical swings in pressure. To maintain the integrity of the 1-Hz data archive, suspect data were not removed but simply ignored in subsequent analyses. The available web tools were developed with the ability to view the observed pressure time series with quality control filtering applied or removed, so high-frequency fluctuations labeled as suspect can be assessed visually on a case-by-case basis.

3.3.3 Temporal Filtering

Since very high-frequency ($> 1\ \text{min}^{-1}$) perturbations are not of interest in this study and to reduce processing time, 1-min samples were derived from the 1-Hz observations. Three Butterworth band-pass filters (referred to as the meso, subsynoptic, and synoptic filters) were applied separately to each 1-min pressure time series after

removing the period-of-record mean. These second-order filters using 5 coefficients were applied twice (forwards and backwards) to minimize unwanted phase shifts. Figure 3.3 depicts the squared magnitude response of each band-pass filter versus period. Following the work of Koch and Saleeby (2001), the meso filter attempts to isolate mesoscale pressure perturbations with periods between 10 min and 4 h, which correspond to the micro-α and meso-γ temporal scales according to Orlanski (1975). The synoptic filter (30 h to 5 days) was chosen to identify pressure perturbations associated with synoptic-scale weather features. The middle filter (4 to 30 h) partially overlaps the other two (which introduces some ambiguity when interpreting its specific temporal range) and focuses on pressure perturbations arising from a complex mix of processes including frontal passages (particularly strong cold fronts) and those leading to semidiurnal and diurnal tides. Following Orlanski (1975), this filter encompasses the meso-β temporal scale, and the longer timescales of mesoscale phenomena according to Markowski and Richardson (2010). We are in essence subdividing the total variance of each pressure time series into 4 bands: meso, subsynoptic, synoptic, and low frequency (i.e., periods longer than 5 days). While the filters are applied continuously to the entire record for each station, the small portions of each time series including and surrounding missing or suspect data are ignored in the subsequent analyses.

Figure 3.4 illustrates these filtering techniques applied to the 24-h period encompassing the mesoscale gravity wave event shown in Fig. 3.1. The gravity wave signature near 0600 UTC 11 April 2013 is clearly isolated by the meso filter while the decreasing pressure trend over the 24-h period is captured by the synoptic filter. The small perturbations on the subsynoptic scale are of less interest in this case. As a

contrasting case, Fig. 3.5 shows pressure traces for a station in southern Texas over a 2-week period during late February 2010. The total range in pressure from +10 hPa to -15 hPa observed during this period is explained in part by perturbations within the synoptic band (±8 hPa) with additional contributions from the subsynoptic band (±3 hPa) and minimal contributions from the meso band. In particular, the subsynoptic band captures the diurnal and semidiurnal fluctuations.

Large pressure rises and falls, hereby denoted as pressure signatures, are identified from each filtered time series. Consecutive local maxima and minima are paired as pressure signature start and end points if they occur within the nominal temporal duration defined for the meso, subsynoptic, and synoptic filters (i.e., 4 h, 30 h, and 5 days, respectively). Events that occur at the beginning or end of the time series as well as near missing or erroneous data periods were checked manually. Metrics (e.g., duration and absolute and perturbation pressure changes) for each event were calculated and stored for later analysis.

Figure 3.6 illustrates how the variance in each filtered time series for a particular station and season relates to one another, to the unfiltered variance of the complete time series, and to corresponding variances at other stations. For this particular case, station T37A in southeast Kansas during the 2011 spring (MAM) season, the total variance about the period-of-record mean is 28.2 hPa^2. This value is substantively less than 80 hPa^2, which corresponds to a scaling value defined approximately from the 80^{th} percentile for all unfiltered variance values for all seasons and stations. The variance in the synoptic period (30 h - 5 day) is 13.1 hPa^2, which places it approximately near the 40^{th} percentile of all the synoptic-filtered time series (i.e., roughly half of the scaling value of 25 hPa^2 for

this band). The large pressure perturbations after 3 May evident in the top time series clearly arise from low-frequency (< 0.2 day^{-1}) fluctuations rather than synoptic scale disturbances that were more common earlier in the spring. The seasonal variances explained by subsynoptic and mesoscale fluctuations during spring 2011 are small (0.82 and 0.058 hPa^2, respectively). However, some large mesoscale events took place and, while small, the variance in the meso band during this season is greater than the ~80^{th} percentile for all the meso-filtered time series. To allow comparison to other stations during other seasons, the "final marker" in the center right displays the magnitudes of the four variance values as vectors in specified compass directions. Interpretation of the marker relative to the 80^{th} percentile scaling vectors indicates that the unfiltered, synoptic, and subsynoptic variances at this station for spring 2011 were below average to average compared to other stations during all seasons, but the meso variance was quite large, indicating active mesoscale phenomena at this station during this season.

3.4. Case Studies

3.4.1. Overview

The web-based products (http://meso1.chpc.utah.edu/usarray/) developed as part of this study to visualize the USArray TA data allow detailed examination of thousands of pressure signatures arising from a wide variety of weather phenomena. For this study, three examples were selected to highlight these analysis capabilities that include relating the available USArray TA pressure observations to surface wind observations and conventional radar imagery. Two events with prominent mesoscale perturbations and one synoptic-scale event were selected to illustrate meteorological features that are

commonly studied. As described in Section 3.3, the pressure time series in Fig. 3.5 illustrates subsynoptic-scale forcing resulting from diurnal and semi-diurnal tides.

3.4.2 11 April 2013 Midwest Gravity Wave Event

One of the stronger mesoscale pressure signatures found in this study was a solitary wave of depression on 11 April 2013 (Figs. 3.1 and 3.4). A strengthening synoptic storm system over the central United States produced several rounds of convection and mesoscale gravity waves from 10-11 April 2013 over a large swath of the country, stretching from the Gulf of Mexico through the Great Lakes region. Similar to the 7 March 2008 solitary wave of depression studied by Ruppert and Bosart (2014), Fig. 3.7 depicts the wave propagation from Iowa into Wisconsin. Circled markers show the locations of the USArray stations, with the marker color denoting the value of the meso-filtered pressure perturbation at the selected time. Large negative pressure perturbations trail the northern edge of the precipitation complex from Iowa into Wisconsin, which is evident in the radar imagery provided courtesy of the Iowa Environmental Mesonet. Such large negative pressure perturbations are a common signature seen in many solitary mesoscale gravity wave structures with precipitation (Ramamurthy et al. 1993). According to Ruppert and Bosart (2014), precipitation regions such as the region depicted here also may contribute to the large pressure reduction seen directly behind the precipitation shield, and often these systems can further evolve into mesohigh-wake low couplets.

Figure 3.8 focuses on the region near J41A (Figs. 3.1 and 3.4) at approximately the time of the wave's peak intensity (0600 UTC) over southern Wisconsin. Included are

surface wind observations with reported sustained or gust values larger than 10 m s^{-1}. Stations with the largest sustained winds and gusts were co-located with the back edge of the precipitation. Time series of the mesoscale-filtered pressure data for USArray station J41A and K42A (Fig. 3.9) depict mesoscale pressure drops of 9.1 hPa in 40 min and 7.3 hPa in 17 min preceded by negligible or small 0.5 hPa pressure rises, respectively. Wind observations at Middleton Municipal Airport (KC29, Fig. 3.9c) are predominantly from the east-northeast at 5-8 m s^{-1} preceding the event. Sustained wind speeds increase to ~15 m s^{-1} with gusts over 20 m s^{-1} during the wave passage and then lessen during the next hour as the wave propagates eastward.

3.4.3 13 June 2013 Mid-Atlantic Derecho

Thunderstorms associated with a shortwave trough over the Great Lake region late on 12 June 2013 led to the eventual development of two long-lived MCS/derecho events that produced widespread wind damage from the Ohio Valley eastward. Both events meet the definition of a derecho as described by Johns and Hirt (1987), and the secondary complex was described as a weak derecho by the Blacksburg, VA NWS office as a result of its continuity (wind damage extending greater than about 400 km) and extensive number of severe (25.9 m s^{-1} or greater) straight-line wind damage reports along the damage swath (NWS Weather Forecast Office Blacksburg, VA, 2014).

The first complex formed over northern Indiana and Ohio early on 13 June 2013 and moved east-southeast through the Mid-Atlantic region and eventually off the coast by 1600 UTC. A second convective complex formed over central Indiana at ~1000 UTC and propagated through Ohio, Kentucky, West Virginia, Virginia, and North Carolina

through the remainder of the day. The first complex had a more classic bow-echo structure, with convective cells along a bowed singular line. The second system was more complex, with several small clusters of convection developing into a larger squall line late in the duration of the event. The top panels of Fig. 3.10 show the propagation of the first complex off the coast from 1245 to 1445 UTC, while the second complex is displayed in the bottom panels from 1940 to 2105 UTC. Both events produce large positive perturbations at USArray stations at the leading edge of the convection.

The largest mesoscale pressure rise associated with these two complexes occurred at station P60A in northern Delaware (Fig. 3.11). A 5.4 hPa rise in 11 min was calculated from the meso-filtered data, which equates to a 29.56 hPa per h rate of change. However, surface observations near the station did not record any severe wind gusts. The second complex produced numerous severe wind observations as it reached the Southern Virginia coastline, as seen in Fig. 3.12. Pressure and wind time series for USArray station T60A and Felker Army Field (KFAF) are shown in Fig. 3.13a-b, respectively. Station T60A had a 3.7 hPa increase in 11 min, while nearby station KFAF recorded wind gusts near 30 m s^{-1} immediately after the passage of the primary gust front. Comparing the pressure time-series evolution between USArray station P60A (Fig. 3.11) and T60A (Fig. 3.13) provides insight into the derecho evolution and spatial variability that would not be seen using filtered or averaged pressure data. At P60A, the 5.4 hPa pressure rise was immediately followed by a several hPa pressure drop ten minutes later, with several hours of more gradual pressure falls thereafter (Fig. 3.11). However, at T60A, the strengthening of the cold pool behind the derecho resulted in a more prolonged pressure maximum (~30 min) and a reduced pressure fall (with a secondary

pressure rise behind the derecho likely associated with outflow).

3.4.4 2014 Valentine's Day Storm

A strong synoptic system, originating in the Gulf of Mexico, moved up the east coast of the United States from 13-15 February 2014. The storm brought widespread heavy snowfall for inland regions spanning from northwestern North Carolina through Maine. Figure 3.14 shows the evolution of this event as an area of low pressure developed off the Mid-Atlantic coastline, strengthened, and moved northeast towards Nova Scotia. The shading of the USArray stations is derived from a three-hour pressure tendency based on the synoptic-filtered dataset to lessen the impact of other time scales in the unfiltered data. The dark blue circles indicated large pressure falls on the synoptic scale, which were located ahead of the propagating synoptic wave. The largest falls were located across New England from 0000-0600 UTC 14 February 2014. Behind the system, pressure rises are seen, with the largest values located along the coastline closest to the low pressure. The unfiltered and synoptic-filtered time series for station Q61A in Delaware are shown in Fig. 3.15. Whether evaluated on the basis of the unfiltered or synoptic-filtered data, the pressure falls of 40 hPa or 29 hPa respectively in 29 h are impressive.

3.5. Perturbation Pressure Variance

To summarize seasonal and spatial differences in the amplitude of the pressure perturbations, the variance vectors introduced in Fig. 3.6 are now used as shown in Figs. 3.16-3.19. Referring to Fig. 3.2, station clusters are used to reduce the number of vectors

displayed on the figures as well as account for the eastward progression of the array during the four years of this study, i.e., there are four roughly north-south-oriented lines of clusters available for each calendar season. Each cluster comprises 2-50 (median 23) stations within 2^o x 6^o latitude-longitude bins during each season. The vectors shown in these figures represent the median variance values derived from the sample of time series available within each cluster.

During the winter (DJF) months (Fig. 3.16), the unfiltered (black vector pointing north) and synoptic-filtered (green vector pointing east) variance increases with latitude. When the array was located farthest west during the 2010-2011 winter and along the east coast during the 2013-2014 winter, the unfiltered variance tended to be larger in the northern tier of clusters than during the 2011-2012 and 2012-2013 winters. Less longitudinal and interannual variance is evident in the synoptic-filtered data. A tendency for subsynoptic variance (blue vectors pointing south) to decrease with latitude is apparent, particularly during the 2010-2011 winter with high subsynoptic variance evident in southern Texas. Mesoscale variance (red vectors pointing west) is largest in the center of the US Array during the 2011-2012 and 2012-2013 winters.

During the spring (MAM) months (Fig. 3.17), unfiltered and synoptic variances are reduced from those found during winter (Fig. 3.16), except for the 2010 and 2011 spring seasons over the upper Great Plains. The largest subsynoptic variance remains over Texas. Substantively larger mesoscale variance during the 2011 spring season is evident from Oklahoma northward to Iowa.

As shown in Fig. 3.18, the unfiltered and synoptic variances reach their minimum values during summer (JJA) compared to other seasons. Large mesoscale variance is

evident over the central Great Plains during the 2010 and 2011 summers. The sub-synoptic variance is lower during the summer months across the southern United States compared to that during spring.

The latitudinal increase in the unfiltered and synoptic variance evident during winter appears as well during autumn (SON) months (Fig. 3.19), particularly during the 2013 autumn with high values over southeast Canada. Large subsynoptic variance is evident again over southern Texas during the 2010 autumn. Mesoscale variance values are small overall compared to other seasons.

3.6. Pressure Signatures

Figures 3.20 and 3.21 summarize pressure signatures derived from the synoptic band-pass filtered data. As introduced in Section 3.3.3, event start and end points are defined by consecutive local maxima and minima in a filtered time series if they occur within the nominal maximum temporal duration defined for the synoptic, subsynoptic, and meso filters (i.e., 5 days, 30 h, and 4 h, respectively). The difference between the maximum and minimum pressure divided by the time interval between the start and end times defines the pressure rate of change. Using the case presented in Fig. 3.15 as an illustration, the 29.2 hPa pressure fall over 29.4 h corresponds to a rate of -23.9 hPa day^{-1} while the subsequent pressure rise of 21.7 hPa over 25.3 h leads to a 20.6 hPa day^{-1} rate. Hence, two pressure signatures often result from a single weather disturbance passing over a station.

A total of 62,482 synoptic signatures were discovered to have a pressure rate of change larger than 8 hPa day^{-1}, with 74.5% of signatures having a temporal duration

between 22-36 h (Fig. 3.20a). Large synoptic pressure signatures are defined here as having pressure rates exceeding 18 hPa day^{-1}, approximately the 95th percentile of all synoptic signatures. This threshold also falls within limits of other similar thresholds between 16-25 hPa day^{-1} (Alexandersson et al. 1998; Bärring and Fortuniak 2009; Krueger and von Storch 2012). Figure 3.20b indicates that very few large synoptic signatures had temporal durations longer than 36 h (1.2%), indicating that stronger signatures were associated with shorter duration synoptic events.

Using the 18 hPa day^{-1} threshold, a total of 3,269 large synoptic pressure signatures were detected during the 4-yr period. Synoptic pressure signatures are most frequent during the winter months (Fig. 3.21a). Maximum values of ~20 synoptic large pressure signatures per season occurred during the 2014 winter along the northeast coast of the United States, corresponding roughly to ~10 strong weather disturbances during that winter. A secondary maximum is evident over the northern Great Plains during the 2011 and 2012 winters. The frequency of such large pressure signatures drops substantively during spring (Fig. 3.21b), with only a few evident across the northern tier of reporting stations. Very few such synoptic signatures were seen during the summer months, e.g., the landfall of Hurricane Isaac contributed to a 23.9 hPa drop in 27 h near Chauvin, LA (station 645A) in the synoptic filtered data. During autumn, an increase towards the northeast is evident, in particular for the stations over southern Ontario and Quebec provinces (Fig. 3.21d).

The ubiquitous occurrence during all seasons of modest subsynoptic-scale pressure fluctuations is evident in Figs. 3.22 and 3.23. Using an initial 0.5 hPa pressure change threshold, 1,187,795 subsynoptic signatures were discovered with a wide range of

temporal durations (Fig. 3.22a). As shown in Figure 3.5, many of these signatures appeared to be associated with fluctuations due to the superposition of diurnal and semidiurnal tides. Large-magnitude subsynoptic signatures are defined here by a pressure rate of change exceeding 1 hPa h^{-1}. This threshold effectively removes routine diurnal and semidiurnal pressure fluctuations, while retaining strong signatures associated with cold frontal passages and larger convective complexes. A total of 5,262 large subsynoptic pressure signatures were found during the 4-yr period, with temporal durations primarily between 3-8 h. Figure 3.23 shows that a peak of ~10 signatures occurred each season during winter, spring, and summer, with a minimum number occurring during the fall. The maxima during winter occur in the Ohio Valley into the northeast United States while the peak number of signatures occur in the central Great Plains region during spring and summer.

From the mesoscale-filtered time series, 301,294 signatures were found using an initial absolute pressure change greater than 1 hPa within 4 h. The majority of these signatures (82.7%) occurred within 1 h (Fig. 3.24a). Large pressure signatures are defined as those having an absolute pressure change greater than 3 hPa within 4 h, corresponding to the 95th percentile of all meso pressure signatures computed. A total of 15,703 mesoscale pressure signatures were found during the 4-yr sample, again with the majority (83.2%) within 1 h (Fig. 3.24b). As shown in Fig. 3.25, very few occurred during autumn and winter. During the 2010-2013 spring seasons, large pressure signatures were more commonplace over the Central Plains and upper Midwest regions, with 20-25 signatures per season evident from Oklahoma northwestward toward Wisconsin. A secondary smaller maximum is also evident in the southeast over Georgia

during spring. A pronounced maximum in mesoscale pressure signatures is evident over the states of Nebraska and Iowa during summer. Several stations recorded 35-40 pressure signatures per season from the 2010-2012 summers when the array was located in this region.

3.7. Summary and Discussion

Surface pressure observations from the USArray have been examined at meso- (10 min - 4 h), subsynoptic (4 h - 30 h), and synoptic (30 h - 5 days) scales. This study is the first to look at the variance of pressure signatures on multiple temporal scales over a broad region at relatively uniform spacing. A unique data source of 1-Hz sampled pressure observations from the eastward-propagating USArray seismic project network was used for this study. Band-pass filters at meso-, sub-synoptic, and synoptic frequencies were applied to the pressure time series, and the occurrences of large-magnitude pressure signatures were identified objectively. All of the resulting tens of thousands of pressure signature events can be looked at individually or collectively through a web interface (http://meso1.chpc.utah.edu/usarray). Several representative case studies were examined here in Section 3.4, followed by aggregate statistics in Sections 3.5 and 3.6. The high temporal resolution of the USArray pressure data provides an enhanced perspective relative to other conventional sources of pressure data for studying mesoscale phenomena, some of which exhibit sharp short-duration pressure perturbations that can propagate over hundreds of km. It is not our intention to imply that the USArray provides a great deal of added value for studying longer-duration pressure perturbations compared to hourly pressure reports available from other meteorological networks.

However, there is considerable value in contrasting the characteristics of pressure perturbations over a range of temporal scales using a consistent dataset as is done in this study.

The relatively short deployment (~2 yr) for each pressure sensor limits interpreting the results of this study as a long-term climatology of pressure perturbations and signatures for a specific locale, although gravity wave climatologies were estimated using even shorter records by Einaudi et al. (1989) and Lee and Barr (1998). This shortcoming is compensated for in some respects by the rich detail afforded by the high temporal sampling. For example, the long-term climatology of mesoscale pressure signatures by Koppel et al. (2000) based on hourly pressure changes larger than 4.25 hPa misses, not surprisingly, the majority of mesoscale pressure signatures (Fig. 3.24). In addition, we have taken care to compensate as best as possible for the year-to-year variability in pressure perturbations by grouping stations as a function of their deployment (Figs. 3.16-3.19). Hence, the larger synoptic variance evident in Fig. 3.16 in the northeastern United States and southern Canada during the 2013-14 winter compared to the smaller synoptic variance in the Great Lakes region during the previous 2 winters is likely due to year-to-year variations in storm tracks embedded within the planetary-scale circulation.

The cumulative statistics presented in Sections 3.5 and 3.6 help to delineate several obvious patterns associated with weather features that are accompanied by pressure perturbations on time scales from minutes to seasons. Foremost, as with nearly all geophysical phenomena, the magnitude of the variance of pressure perturbations at low frequencies (spanning beyond 5 days) is larger than that for any of the filtered bands

(synoptic, subsynoptic, or mesoscale), and the variance within the mesoscale band is the weakest of all. Hence, while the pressure signatures associated with mesoscale severe weather events tend to be quite distinct and frequent (Fig. 3.22), their relative amplitude during all seasons is small compared to the pressure changes associated with more benign shifts in the large-scale circulation (note the relative scales in Figs. 3.16-3.19). During winter and fall, the pressure perturbations are most dominated by low-frequency (longer than 5 days) and synoptic-scale fluctuations (Figs. 3.16 and 3.19), with increasing synoptic variance with increasing latitude.

Phenomena on subsynoptic scales and mesoscales tend to be more ubiquitous during the warm seasons, with mesoscale events prominent during the 2010 and 2011 spring and summer seasons over the central Great Plains (Figs. 3.23 and 3.25). Climatologically, severe convective events begin to peak in frequency across the southern plains during the spring, suggesting the large pressure signature maxima over Oklahoma and Arkansas in Fig. 3.17 that shift northward to the central Great Plains during summer in Fig. 3.18 are likely due to organized convective activity. The seasonal variations of the large-magnitude subsynoptic pressure signatures evident in Fig. 3.23 highlight the diversity of mechanisms capable of forcing them [e.g., sharp frontal passages during the winter and mesohighs, wake lows, and sequences of organized convection during summer (Carbone et al. 2002)]. Pressure variations in the southern half of the United States exhibit pronounced diurnal and semidiurnal cycles in pressure during summer (Fig. 3.18). As the USArray shifted east during the 2012 and 2013 warm seasons, the number of large mesoscale pressure perturbations diminished due to reduced convective activity (Figs. 3.23 and 25).

The over 48 billion pressure observations collected by the USArray TA pressure network and analyzed here are available for statistical analysis and graphical display at http://meso1.chpc.utah.edu/usarray. While the period of this study ended on 28 February 2014, USArray TA pressure data are still being collected routinely and are available via the web. Approximately 180 stations are being left in place to collect data for several years across the eastern and central United States. As part of the EarthScope initiative, another subset of the USArray is to be deployed across Alaska beginning in late 2014.

This study introduces the USArray TA pressure data in part as a means to stimulate further research whether at specific locales (e.g., Lee and Barr 1998 analyzed gravity waves within a forest) or simultaneously tracking multiple medium to large-amplitude pressure signatures and their spatiotemporal interactions (e.g., Adams-Selin and Johnson 2010). The broad geographic coverage at ~70 km horizontal resolution afforded by the pseudo-gridded USArray TA over the eastern United States during the 2010-2014 period provides an excellent data set for case-study analysis of large-amplitude gravity wave propagation dynamics within this region. These large-amplitude gravity waves (both solitary and wave packets) are known to propagate several hundred kilometers at speeds of 10-35 m s^{-1} (Adams-Selin and Johnson 2010; Ruppert and Bosart 2014; Clark et al. 2014), which extends beyond the geographic range of previous moderate-density pressure networks that have been used to study large-amplitude gravity waves (e.g., Koch and Siedlarz 1999; Jewett et al. 2003).

The capability for researchers to examine individual as well as sets of large pressure perturbations within temporal bands (mesoscale, sub-synoptic, synoptic) or simply from the unfiltered pressure time series is an important outcome of this study.

Since the temporal evolution of some weather events does not fit neatly into the filter windows selected here (e.g., the multiple convective events described by Carbone et al. 2002), careful evaluation of the unfiltered and filtered data is necessary as well as taking advantage of other data resources. For example, vertical rawinsonde profiles at Green Bay, WI and Davenport, IA confirm that the environmental conditions favorable for forming and maintaining ducted gravity waves (e.g., shallow surface mixed layer capped by a strong stable layer and wind reversal with height) were present during the 11 April 2013 gravity wave case discussed in Section 3.4.2 (not shown).

Researchers may find the pressure data useful for validating forecasts available from research and operational numerical weather prediction models. For example, forecasts at lead times of 1-2 days from the Global Forecast System model of the National Centers for Environmental Prediction (NCEP) suggested internal gravity waves were likely to form within an evolving northeast United States coastal low on 26 November 2014 (not shown). Researchers following this event used the USArray pressure website to evaluate the model guidance and to interpret the subsequent development of banded precipitation features within the storm evident in radar imagery (B. Colle, personal communication).

To develop high-resolution gridded fields of sea level pressure over the USArray domain, we are now testing a two-dimensional variational analysis technique to create sea level pressure grids at 2.5 km horizontal resolution at 5 min intervals. These grids are being used to examine the propagation of mesoscale pressure perturbations that are difficult to detect from the widely spaced USArray alone or from other conventional meteorological networks. Surface pressure 1-h forecasts available every hour from the

NCEP Rapid Refresh model are downscaled by NCEP to a 2.5 km grid for the Real-Time Mesoscale Analysis (RTMA, de Pondeca et al. 2011). We interpolate the differences in these pressure fields from one hour to the next using cubic splines in the time domain at 5 min intervals. The corresponding 1-h differences in pressure at the USArray locations are then used to adjust the background fields using the variational approach described by Tyndall and Horel (2012). Applying this approach to the 11 April 2013 case examined in Section 3.4.2 demonstrates the spatial and temporal continuity of the wave progressing across the Great Lakes region.

3.8 Acknowledgements

Funding for this research was provided by National Science Foundation Grant 1252315. Access to USArray pressure data was provided by the Incorporated Research Institutions of Seismology Web Services, as well as the Array Network Facility at Scripps Institution of Oceanography, University of California San Diego. Web product radar imagery was courtesy of the Iowa Environmental Mesonet web services. Wind observations provided by developmental API services courtesy of MesoWest. The authors thank the University of Utah Center for High Performance Computing (CHPC) for computational hardware and software, as well as providing a host location for developed web products.

Table 3.1. Observation and quality control statistics for USArray 1-Hz pressure observations from 1 Jan 2010 to 28 Feb 2014.

Metric	**Value**
Individual Stations	997
Total 1-Hz Observations Collected	48,358,325,315
Total 1-Hz Observations Retained Post-QC	47,200,863,231
Total 1-Hz Observations Retained Post-QC Percentage	97.61%
Median Station Active Period	615.5 days
Median Percentage of Expected Observations	99.84%
Median Percentage of Observations Retained Post-QC	99.79%

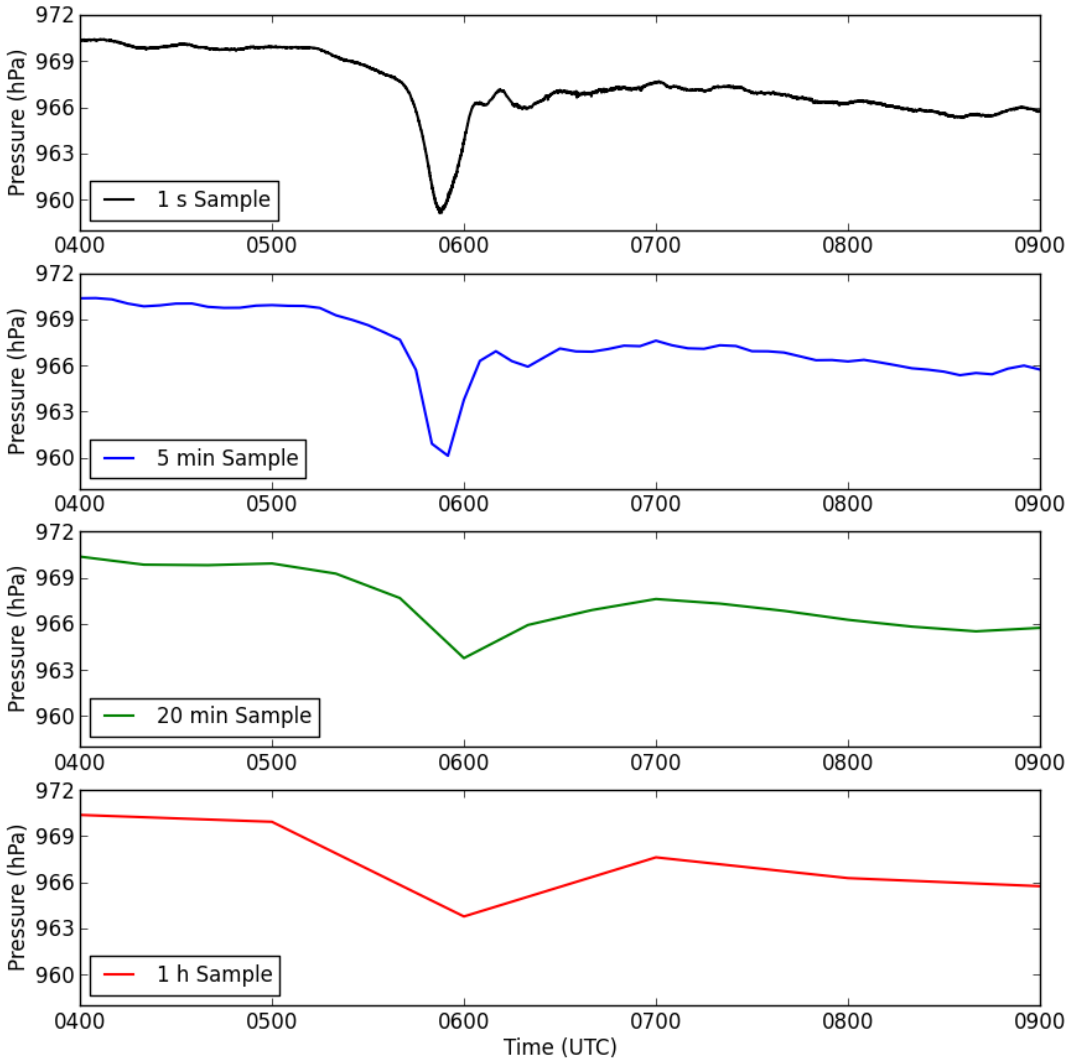

Fig. 3.1. Pressure sampled at 1 Hz (black), 5 min (blue), 20 min (green), and hourly (red) from USArray station J41A (Loganville, WI) during 0400-0900 UTC 11 Apr 2013.

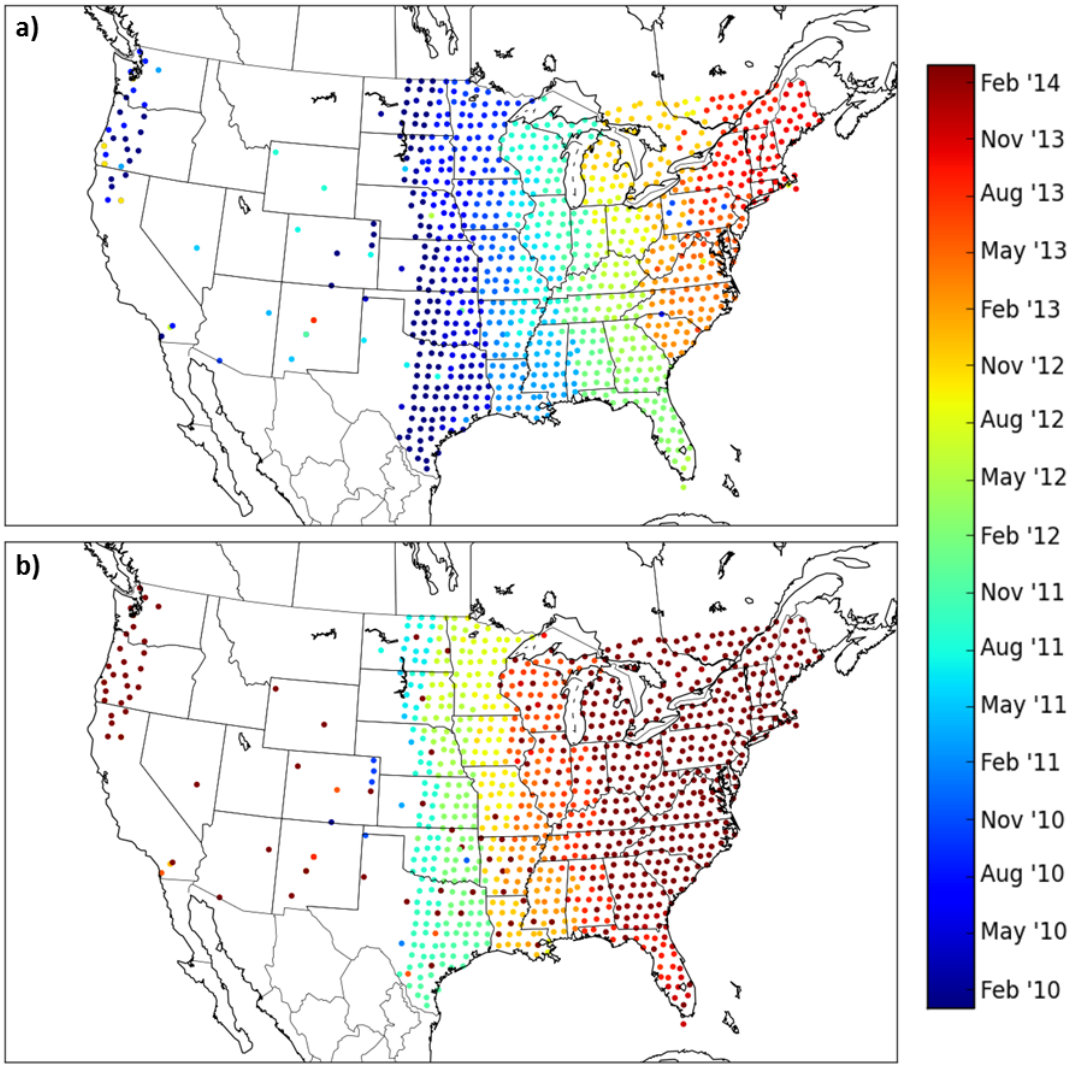

Fig. 3.2. USArray seismic station locations from 1 Jan 2010 to 28 Feb 2014. Marker colors denote the (a) first and (b) last date of pressure observations.

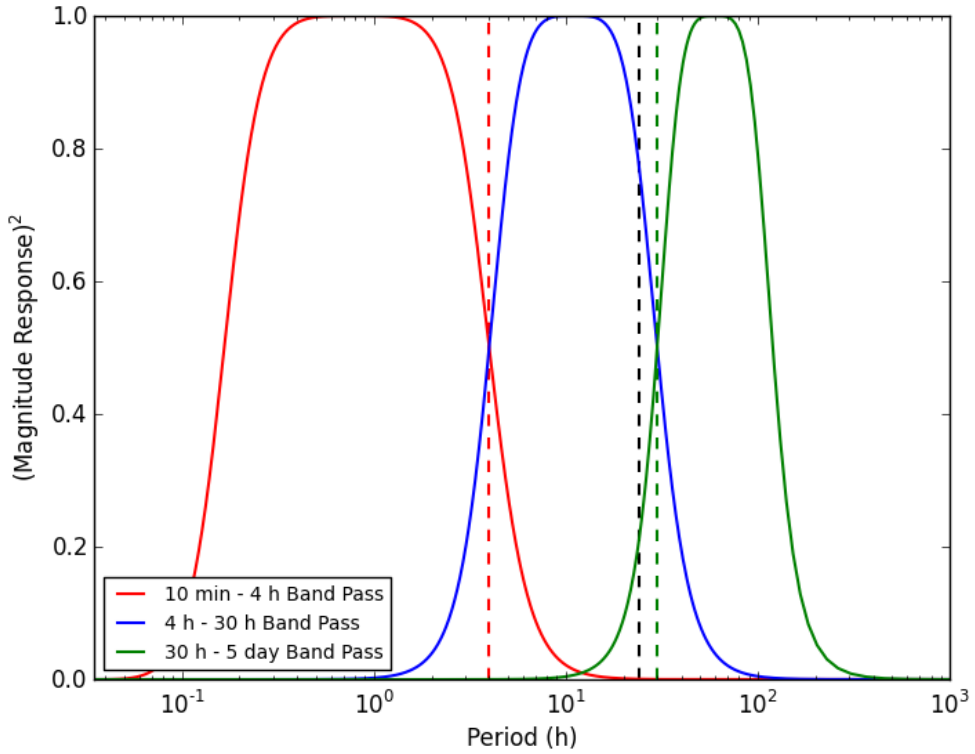

Fig. 3.3. Period (h) versus squared magnitude response for the mesoscale (red), subsynoptic (blue), and synoptic (green) band-pass filters applied to the pressure observations. Vertical lines denote 4 h (red dashed), 24 h (black dashed), and 30 h (green dashed) periods.

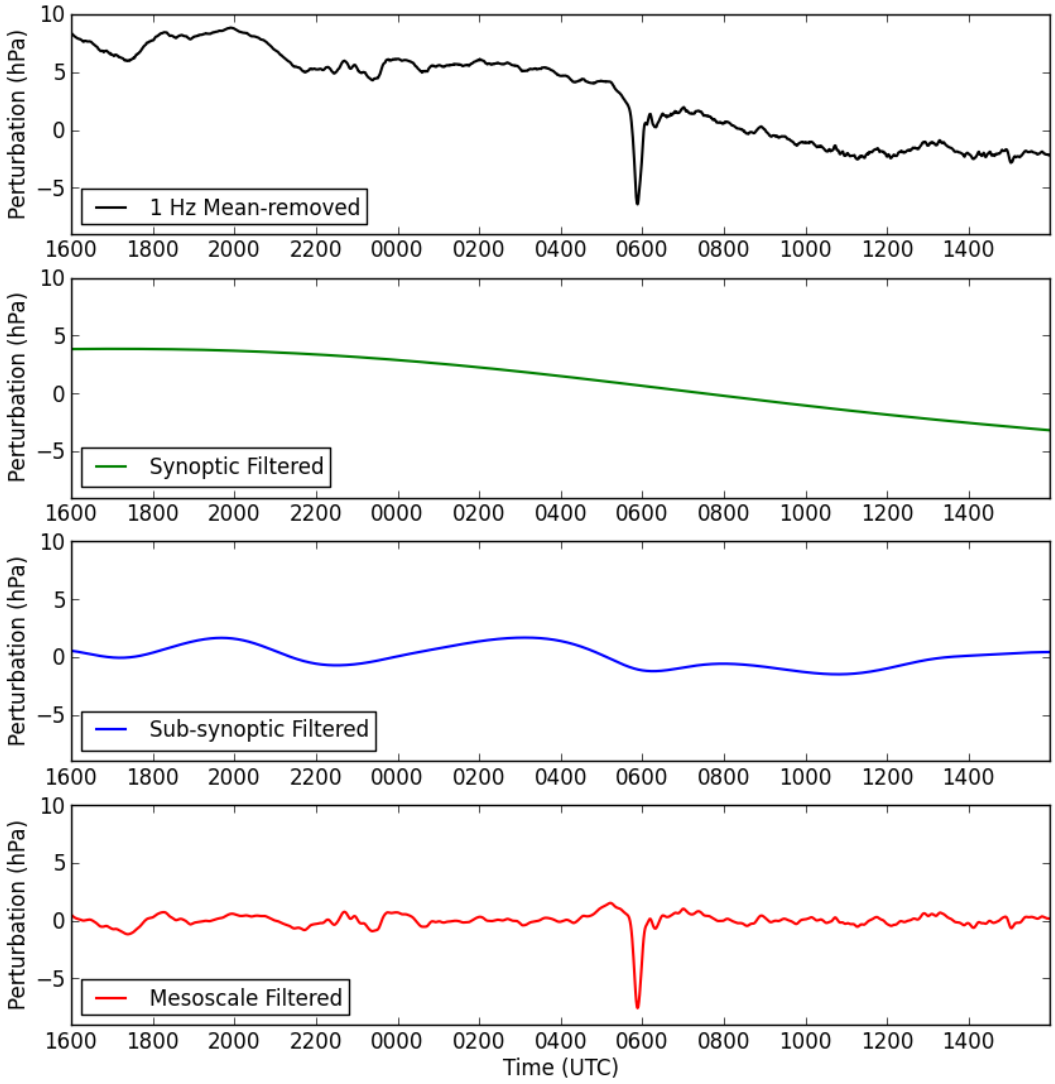

Fig. 3.4. 1-Hz pressure data (black) and synoptic (green), sub-synoptic (blue), and meso (red) filtered pressure data for USArray station J41A (Loganville, WI) during 1600 UTC 10 Apr 2013 - 1600 UTC 11 Apr 2013. The mean derived from the entire station time series was subtracted from the 1-Hz data.

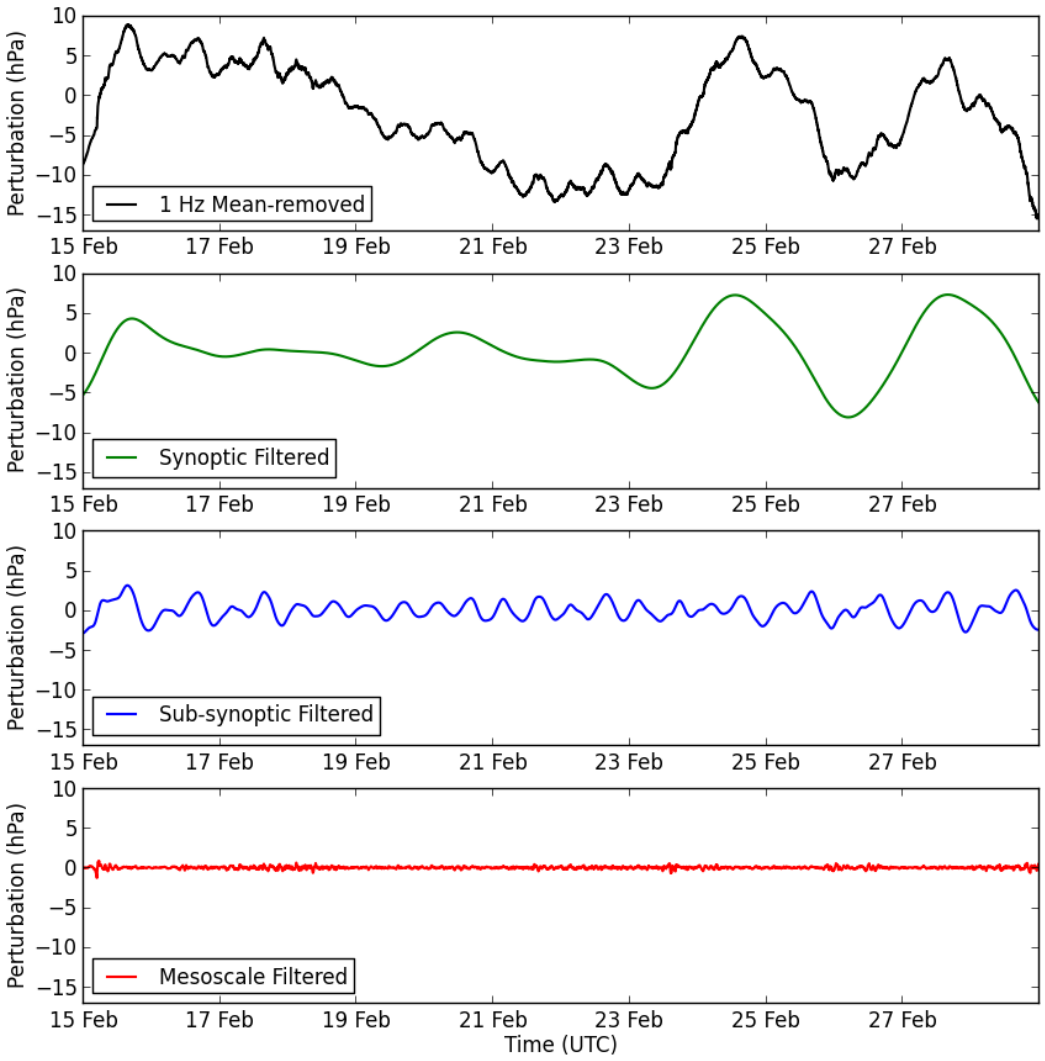

Fig. 3.5. As in Figure 3.4, but for USArray station O35Z (Hargill, TX) from 0000 UTC 15 Feb 2010 - 0000 UTC 1 Mar 2010.

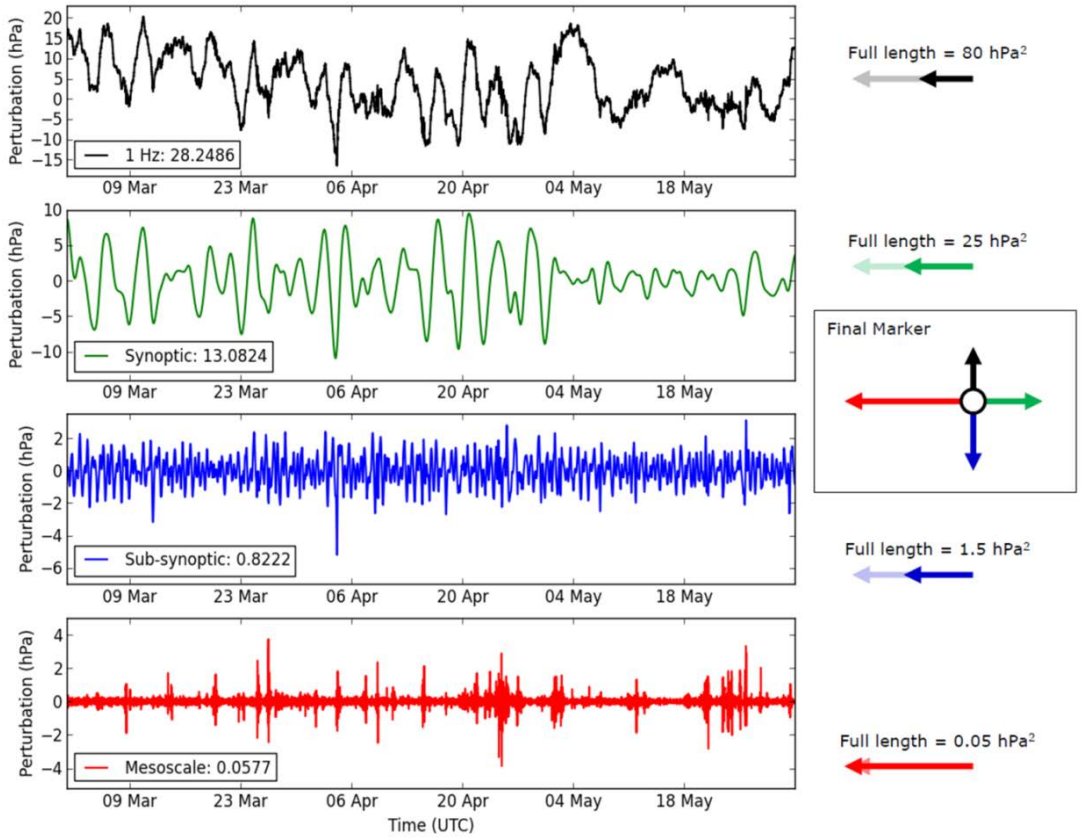

Fig. 3.6. Time series as in Figure 3.4 for USArray station T37A (Cheneyville 1850, KS) for the entire 2011 spring season (MAM). The variance (hPa^2) is provided in the legend for each time series. Vectors corresponding to the variance magnitudes are shown on the right (solid vectors) along with the corresponding "unit length" variance values (translucent vectors). The four vectors are then combined in a compass format for the final marker shown to the center-right.

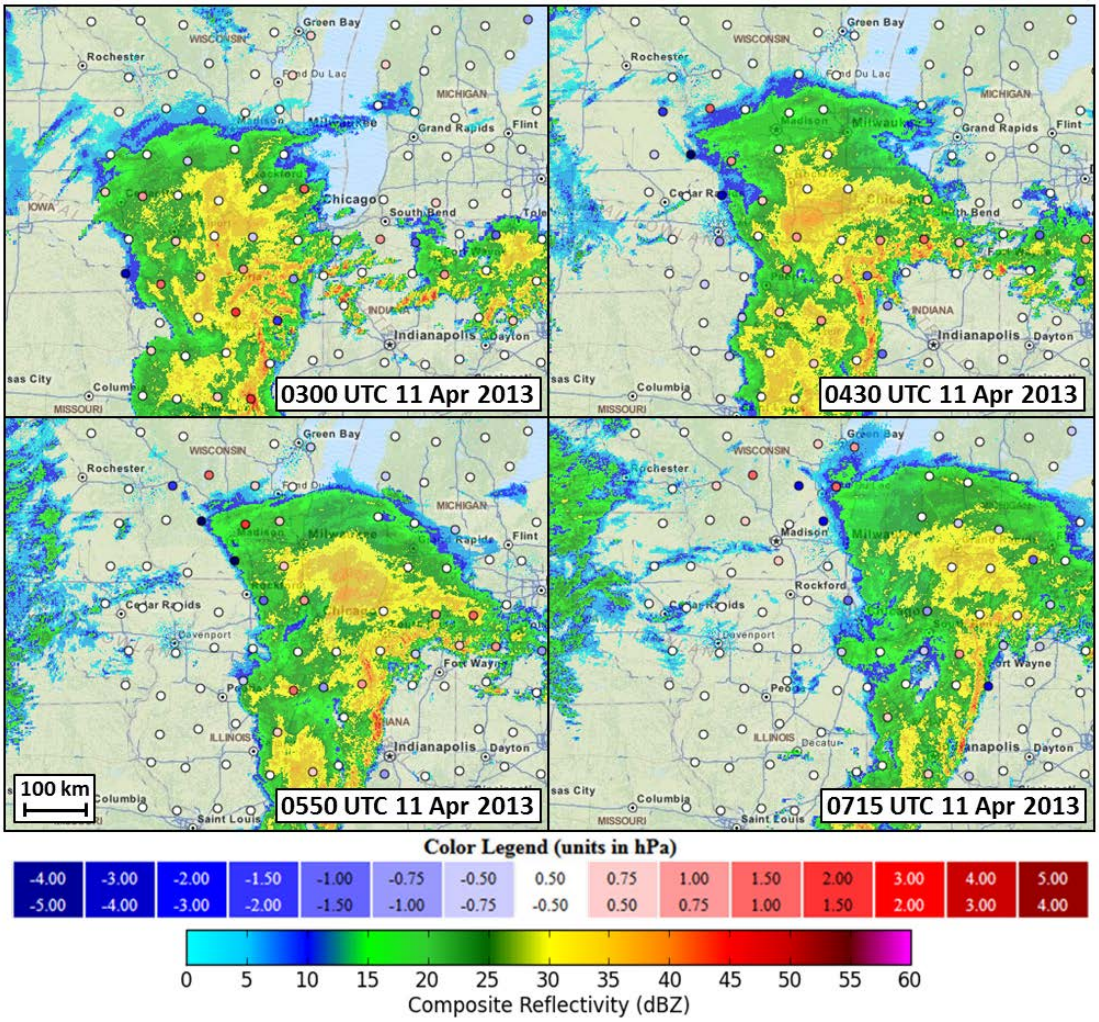

Fig. 3.7. USArray mesoscale-filtered pressure perturbations (hPa) overlaid on composite radar reflectivity at 0300, 0430, 0550, and 0715 UTC 11 Apr 2013. Red (blue) filled circles indicate positive (negative) perturbations according to the color bar as used on the website (http://meso1.chpc.utah.edu/usarray). Composite radar imagery provided by the Iowa Environmental Mesonet web services.

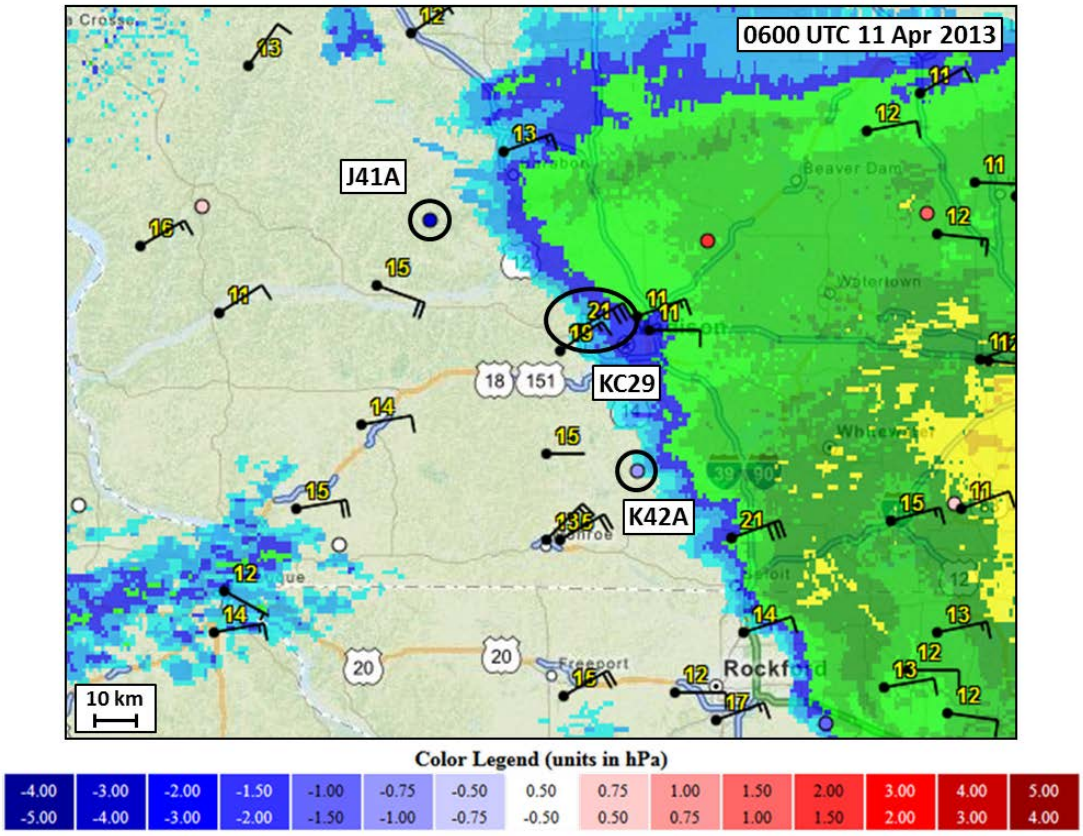

Fig. 3.8. As in Figure 3.7 except near southern Wisconsin at 0600 UTC 11 Apr 2013 with wind observations greater than 10 m s^{-1} added. A full wind barb represents 5 m s^{-1} sustained wind speed, with wind gust values labeled to the upper-right of the station. Stations discussed in the text are circled and labeled.

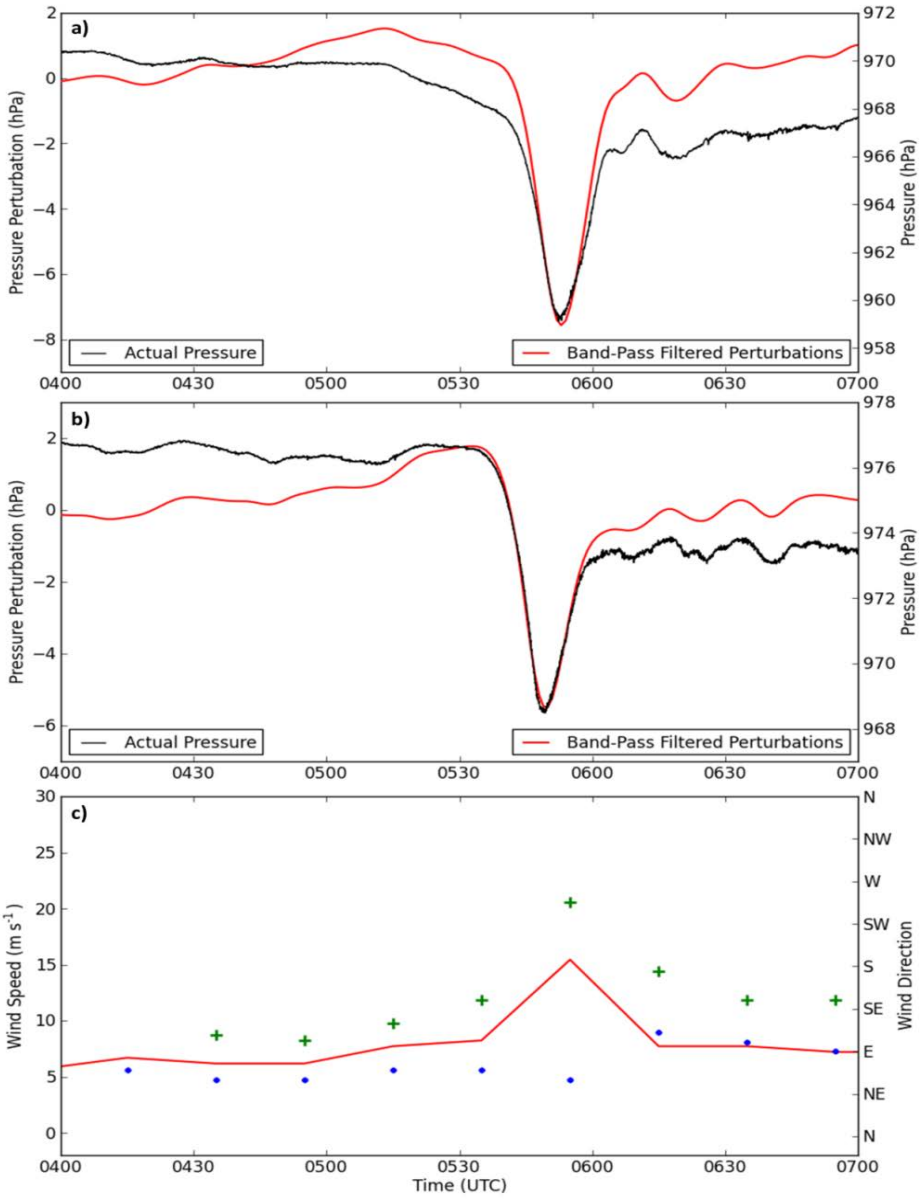

Fig. 3.9. (a) Time series of 1-Hz pressure (hPa, black line according to scale on the right) and mesoscale band-pass filtered pressure perturbations (hPa, red line according to scale on the left) for USArray station J41A (Loganville, WI) from 0400-0700 UTC 11 Apr 2013. (b) As in (a) but for USArray station K42A (Prairie Point, WI). (c) Wind speed (solid red), wind direction (blue circle markers), and wind gust (green cross markers) for station KC29 (Middleton Municipal Airport, WI).

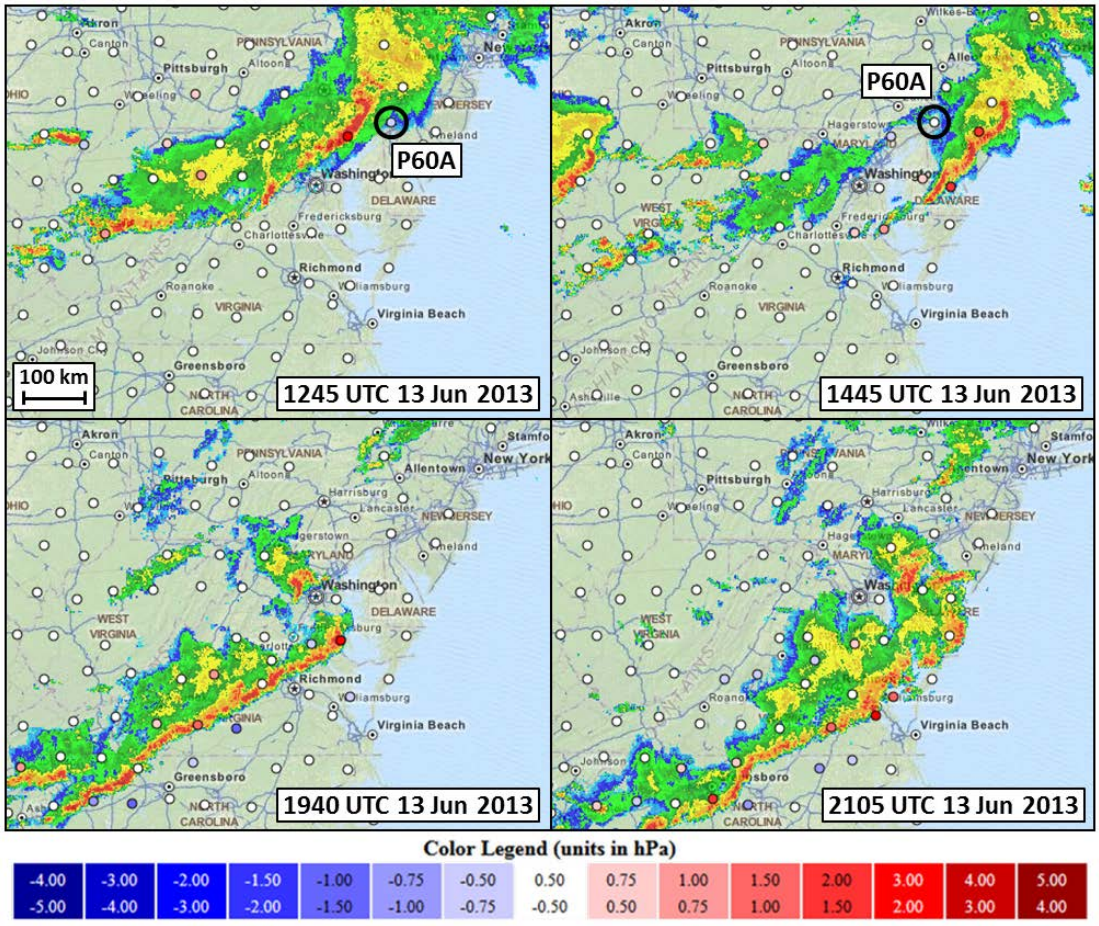

Fig. 3.10. As in Figure 3.7, but for two derecho events across the Mid-Atlantic at 1245, 1445, 1940, and 2105 UTC 13 Jun 2013.

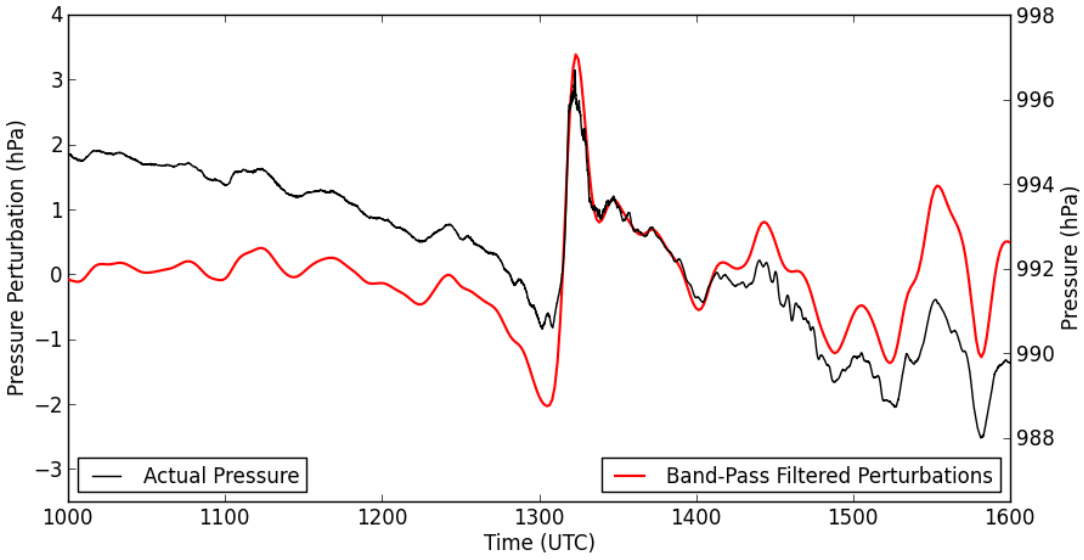

Fig. 3.11. As in Figure 3.9a, but for station P60A (Greenville, DE) from 1000-1600 UTC 13 Jun 2013.

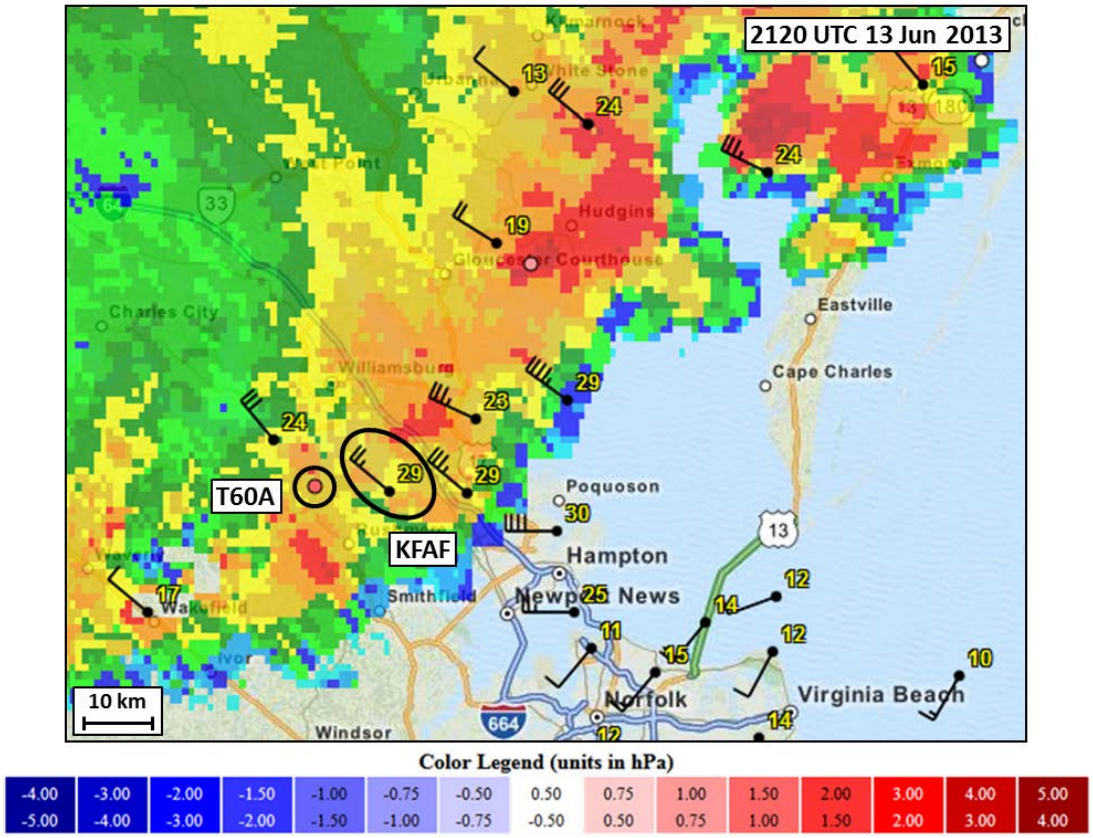

Fig. 3.12. As in Figure 3.8, but for the derecho event across the Mid-Atlantic at 2120 UTC 13 Jun 2013.

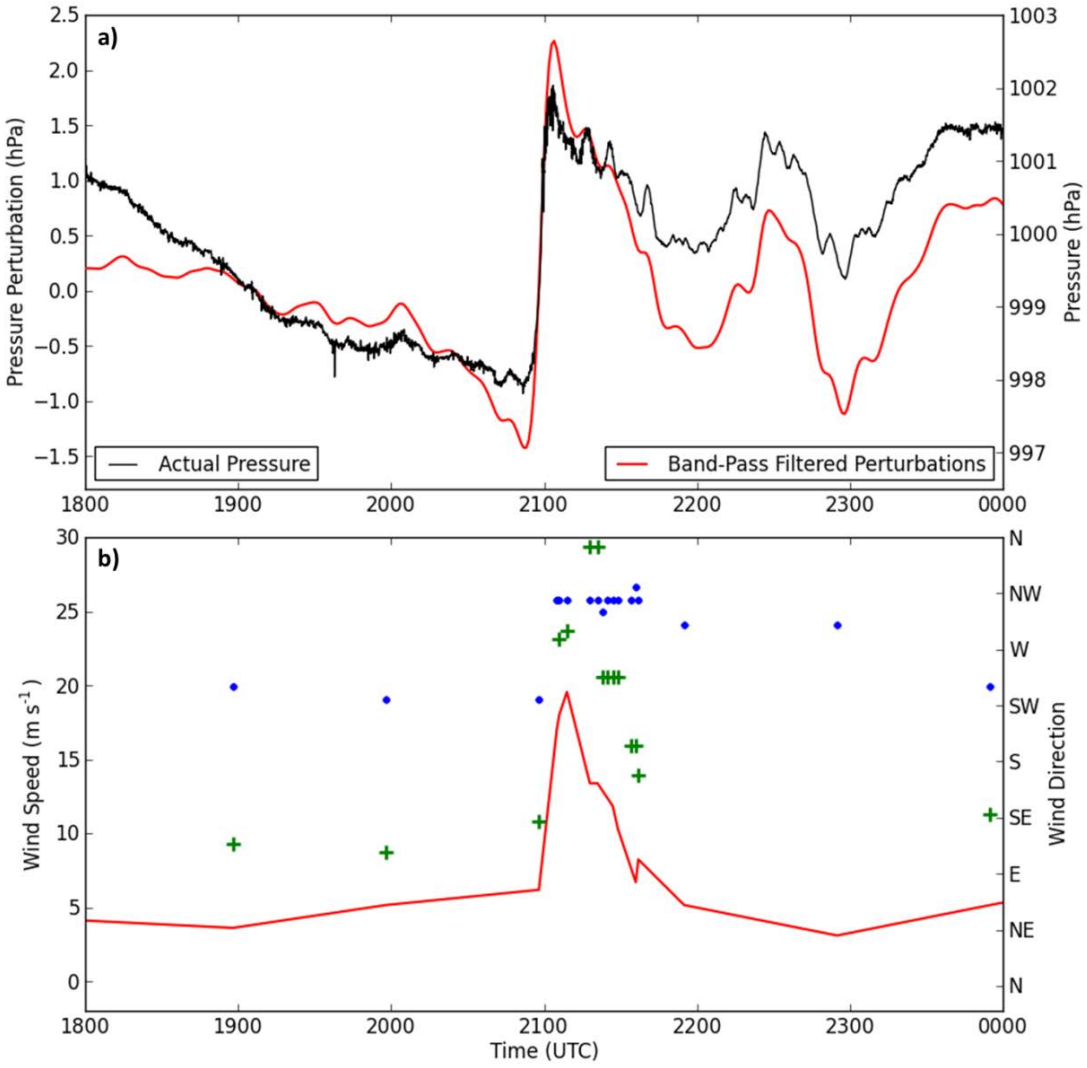

Fig. 3.13. (a) As in Figure 3.9a, but for USArray station T60A (Surry, VA) from 1800 UTC 13 Jun 2013 - 0000 UTC 14 Jun 2013 during a derecho event. (b) As in Figure 3.9c, but for station KFAF (Felker Army Airfield, VA) between 1800 UTC 13 Jun 2013 - 0000 UTC 14 Jun 2013.

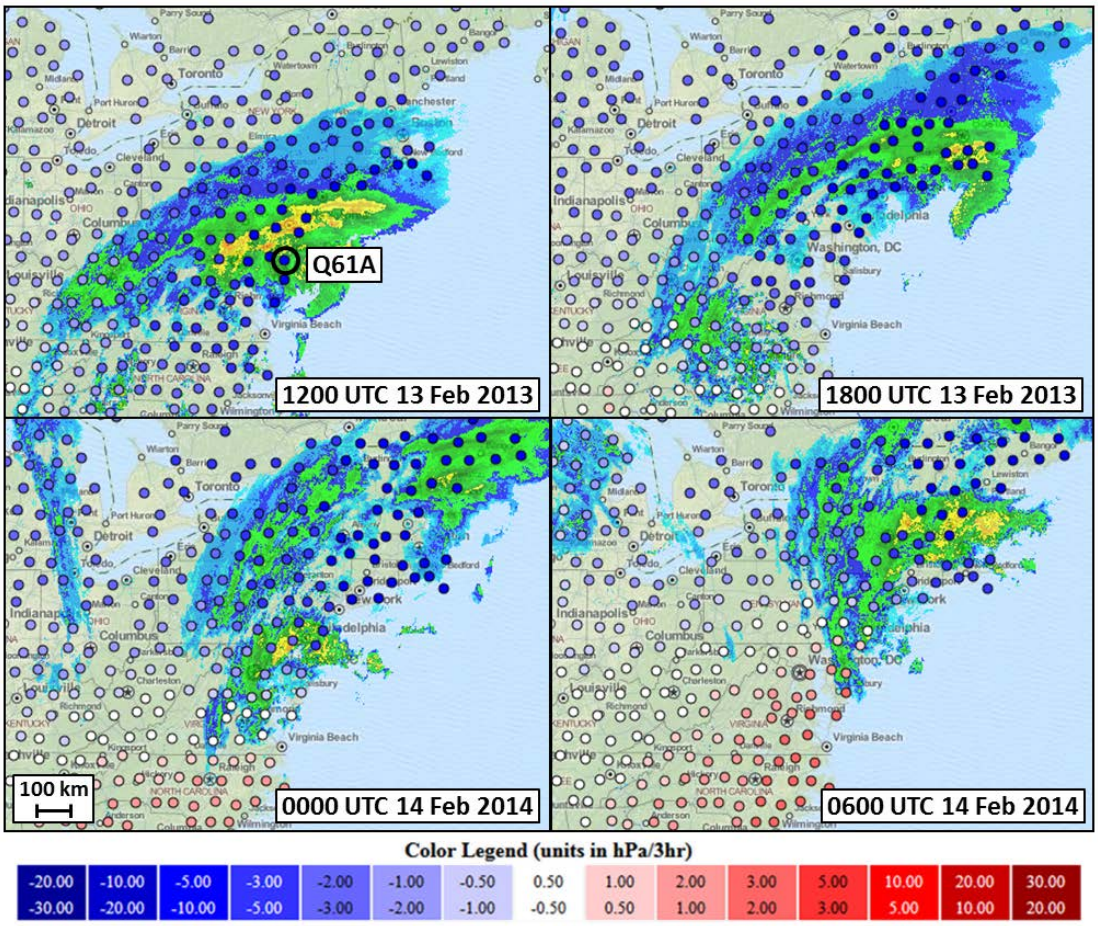

Fig. 3.14. USArray synoptic-filtered pressure tendency (hPa 3 h^{-1}) overlaid with radar reflectivity imagery for a northeast snowstorm event from 1200 UTC 13 Feb 2014 – 0600 UTC 14 Feb 2014. Red (blue) filled circles indicate positive (negative) pressure tendencies according to the color bar as used on the website (http://meso1.chpc.utah.edu/usarray).

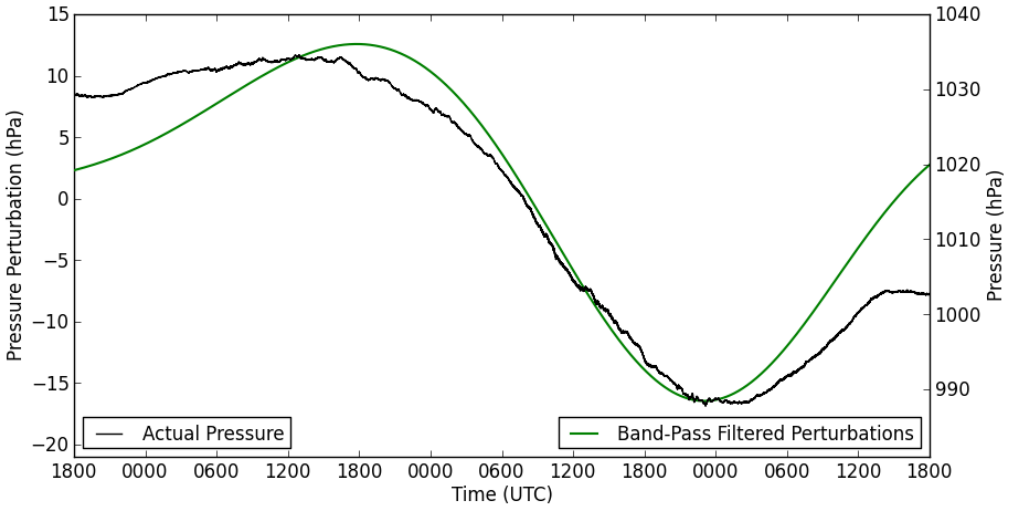

Fig. 3.15. Time series of 1-Hz pressure (hPa, black line according to scale on the right) and synoptic band-pass filtered pressure perturbations (hPa, green line according to scale on the left) for USArray station Q61A (Milford, DE) from 1800 UTC 11 Feb 2014 - 1800 UTC 14 Feb 2014.

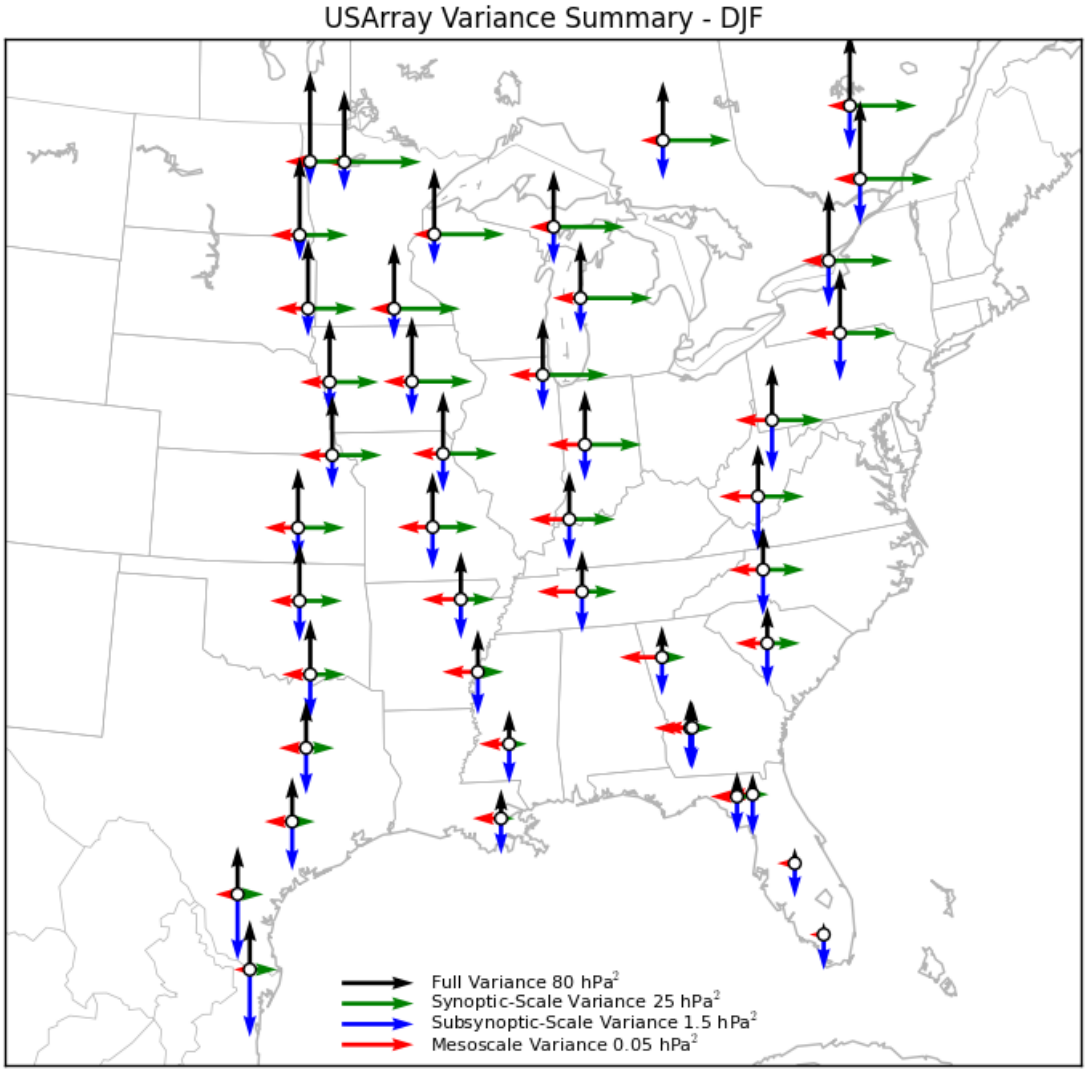

Fig. 3.16. USArray pressure perturbation variance during winter (DJF) seasons from 2010-2011 to 2013-2014. The variance values at each station are combined into station clusters as described in the text. See Figure 3.6 for the description of the markers with vector scaling lengths provided at the bottom.

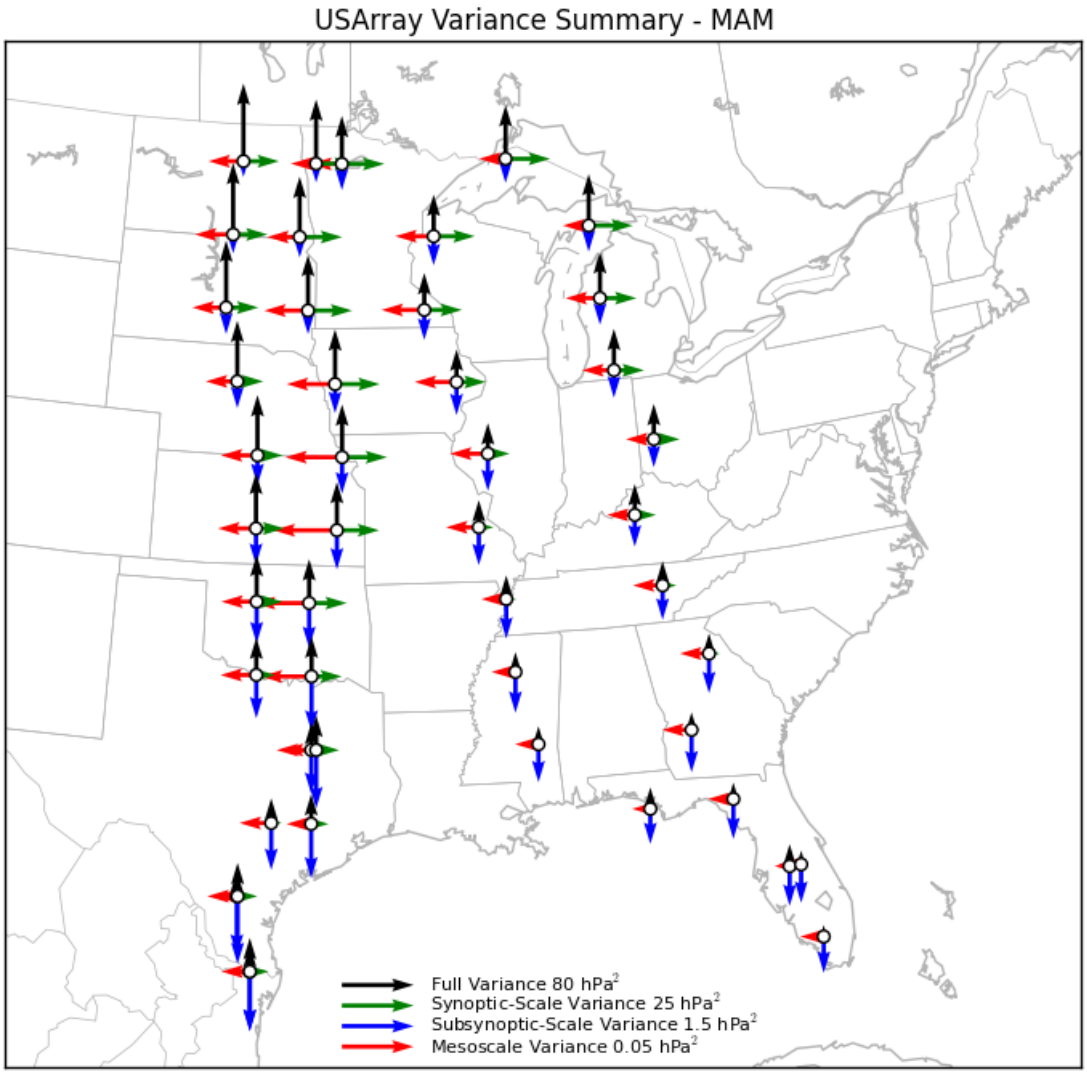

Fig. 3.17. As in Figure 3.16 but for spring (MAM) seasons from 2010-2013.

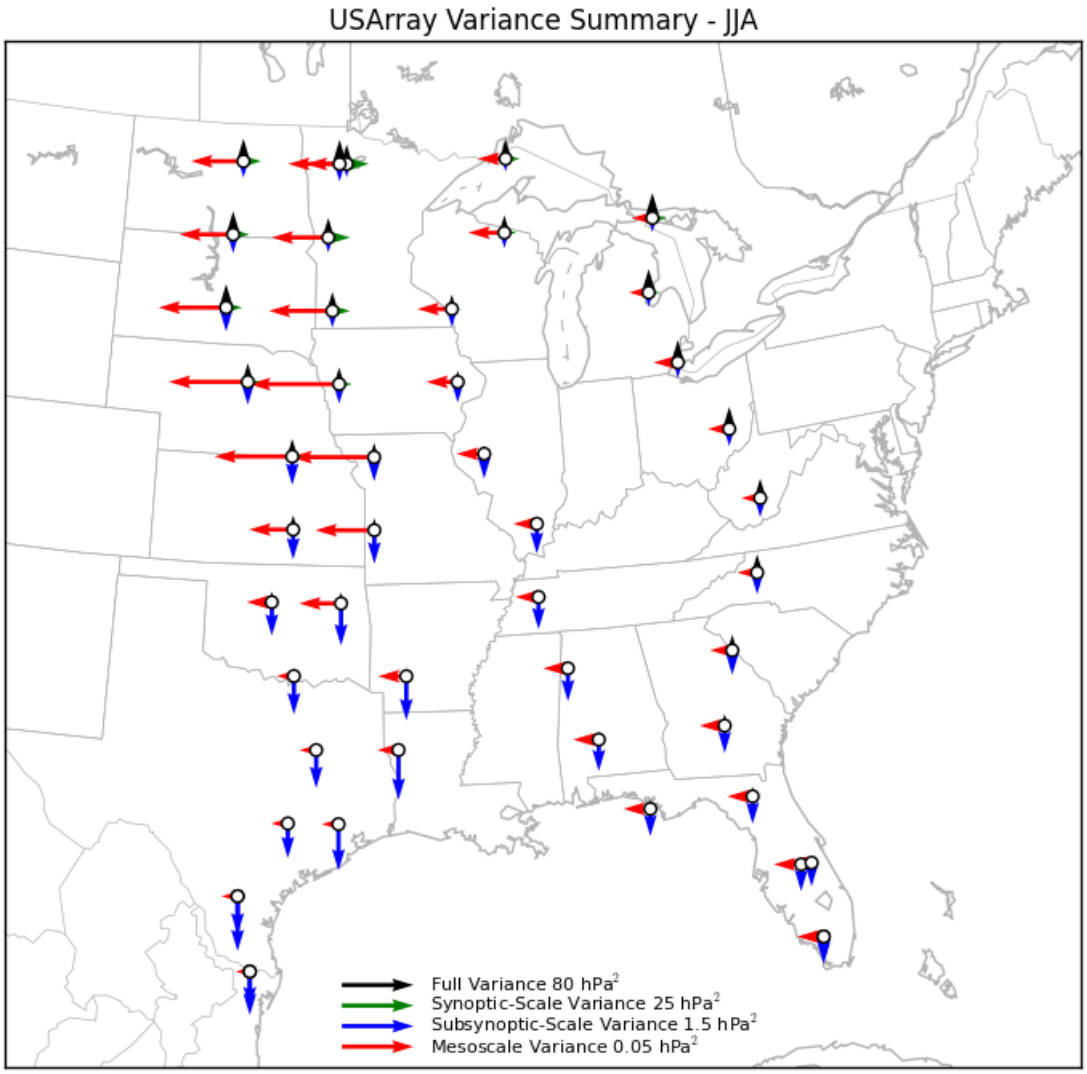

Fig. 3.18. As in Figure 3.16 but for summer (JJA) seasons from 2010-2013.

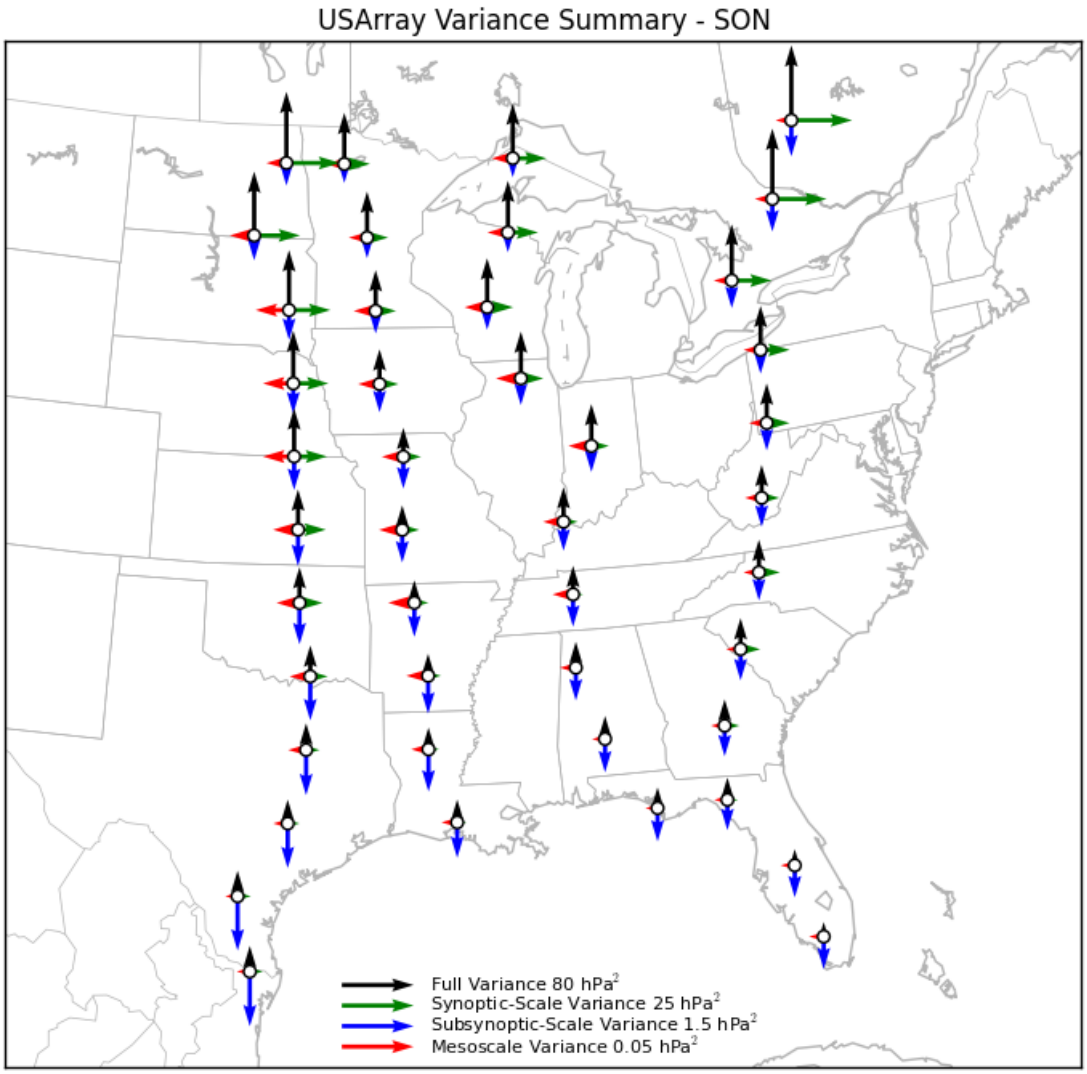

Fig. 3.19. As in Figure 3.16 but for autumn (SON) seasons from 2010-2013.

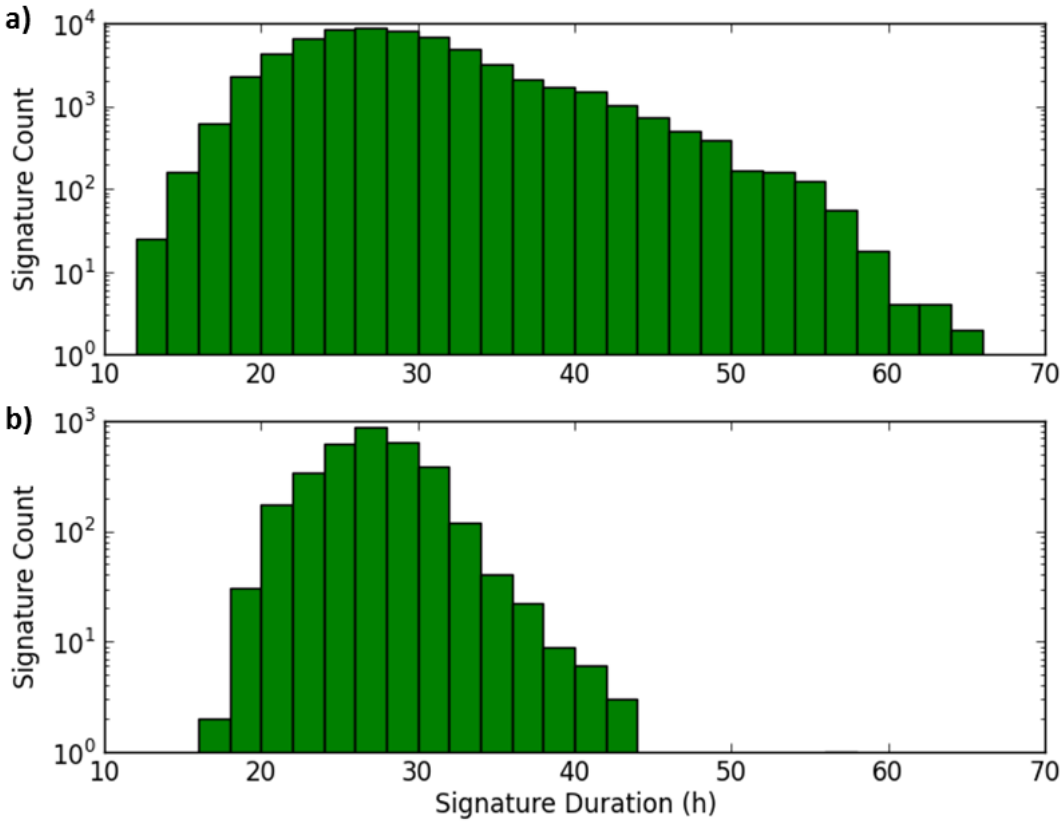

Fig. 3.20. (a) Synoptic pressure signature frequencies as a function of signature temporal duration (h) for all signatures detected (pressure rate magnitude exceeding 8.0 hPa day^{-1}). (b) As in (a) but for only large signatures (pressure rate magnitude exceeding 18.0 hPa day^{-1}). Signature count axis given in log scale.

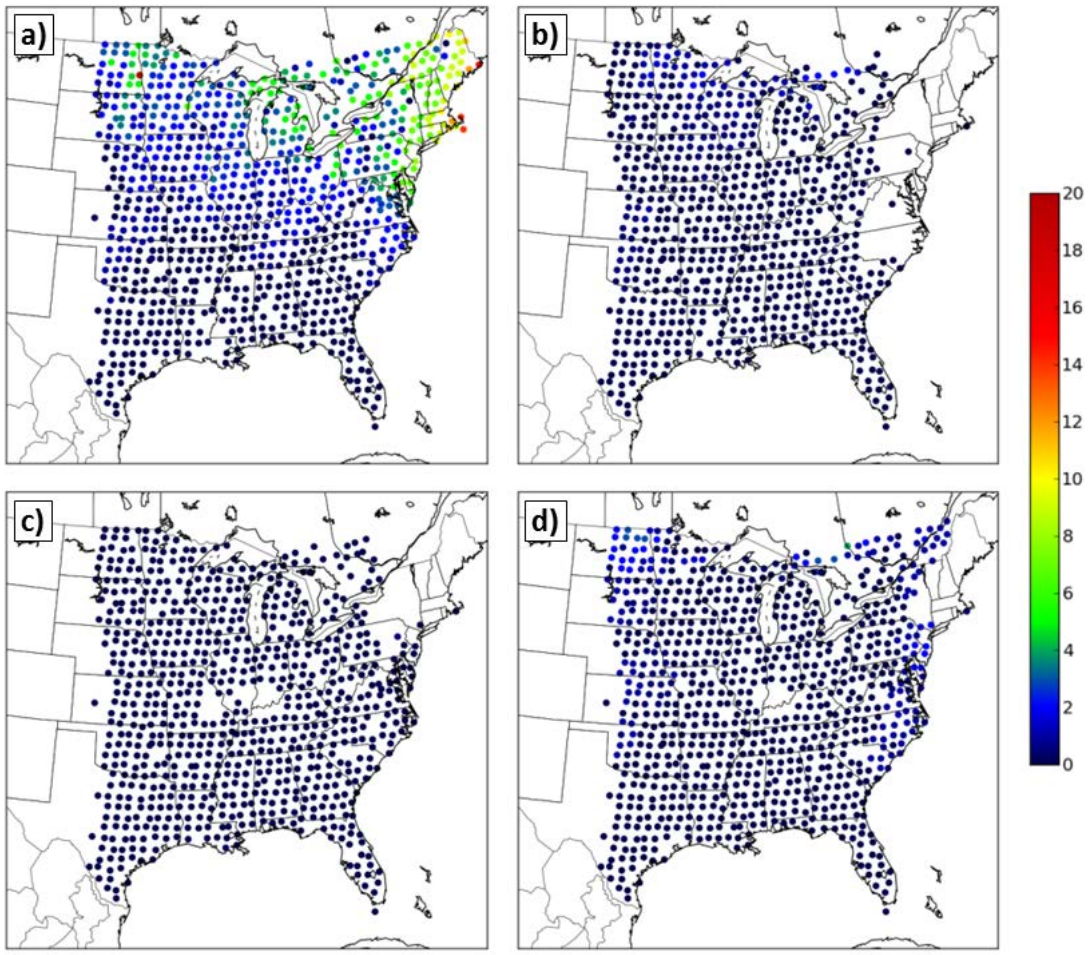

Fig. 3.21. Synoptic pressure signatures per season with pressure rate magnitudes exceeding 18.0 hPa day^{-1} according to the scale on the right during (a) winter (DJF), (b) spring (MAM), (c) summer (JJA), and (d) autumn (SON).

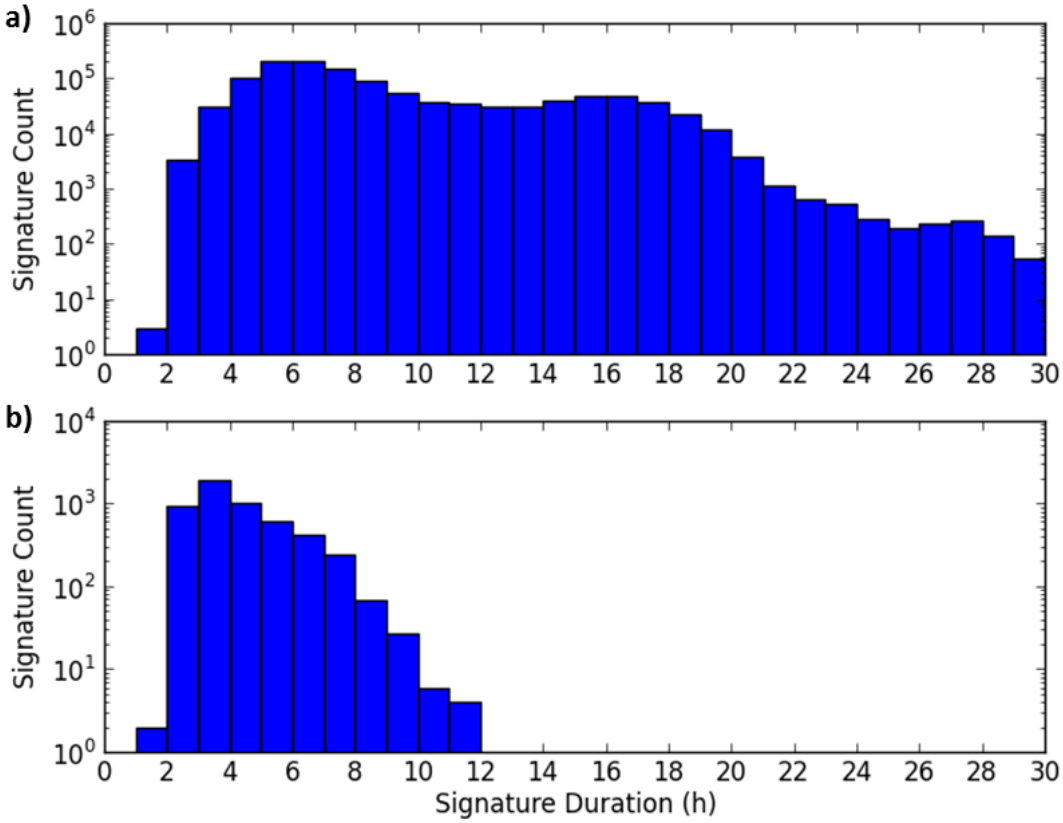

Fig. 3.22. (a) Subsynoptic pressure signature frequencies as a function of signature temporal duration (h) for all signatures detected (pressure change magnitude exceeding 0.5 hPa). (b) As in (a) but for only large signatures (pressure rate magnitude exceeding 1.0 hPa h^{-1}).

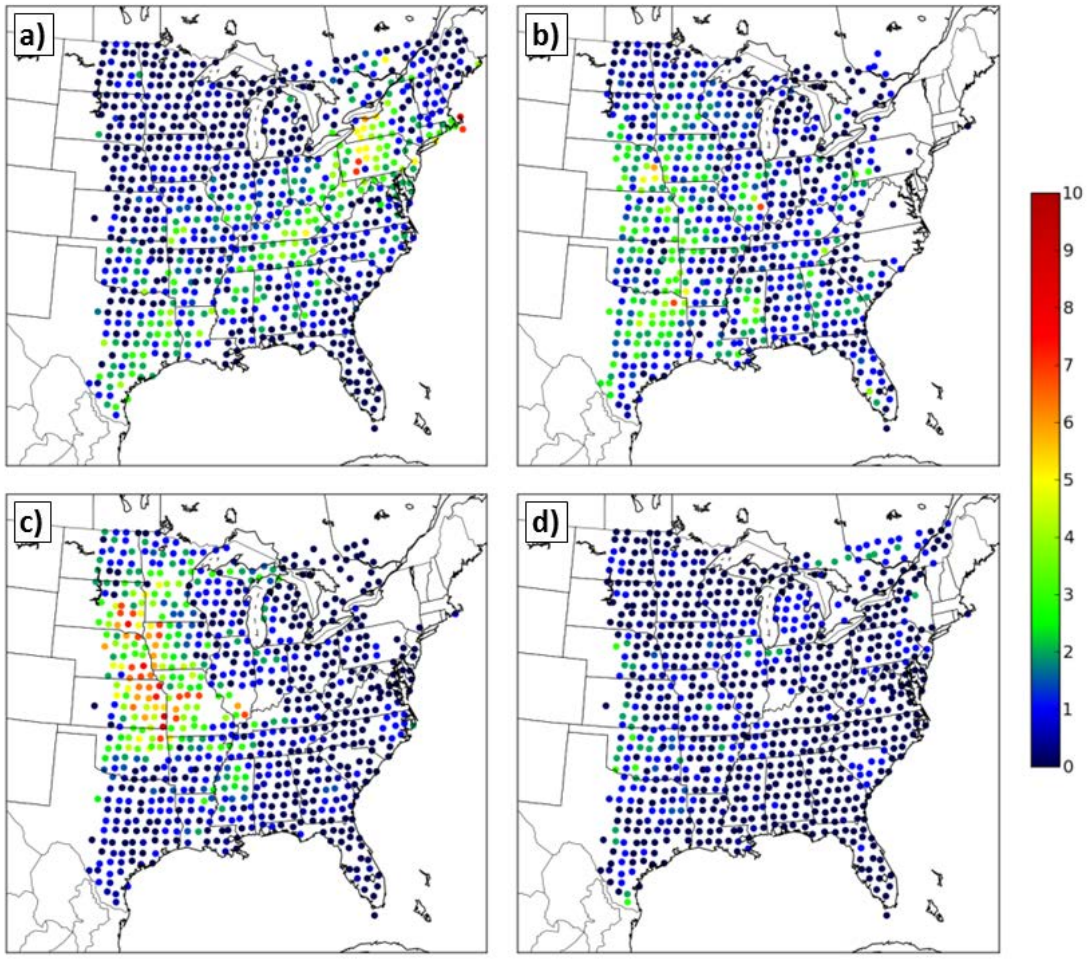

Fig. 3.23. As in Figure 3.21 except for subsynoptic pressure signatures with pressure rate magnitudes exceeding 1 hPa h^{-1}.

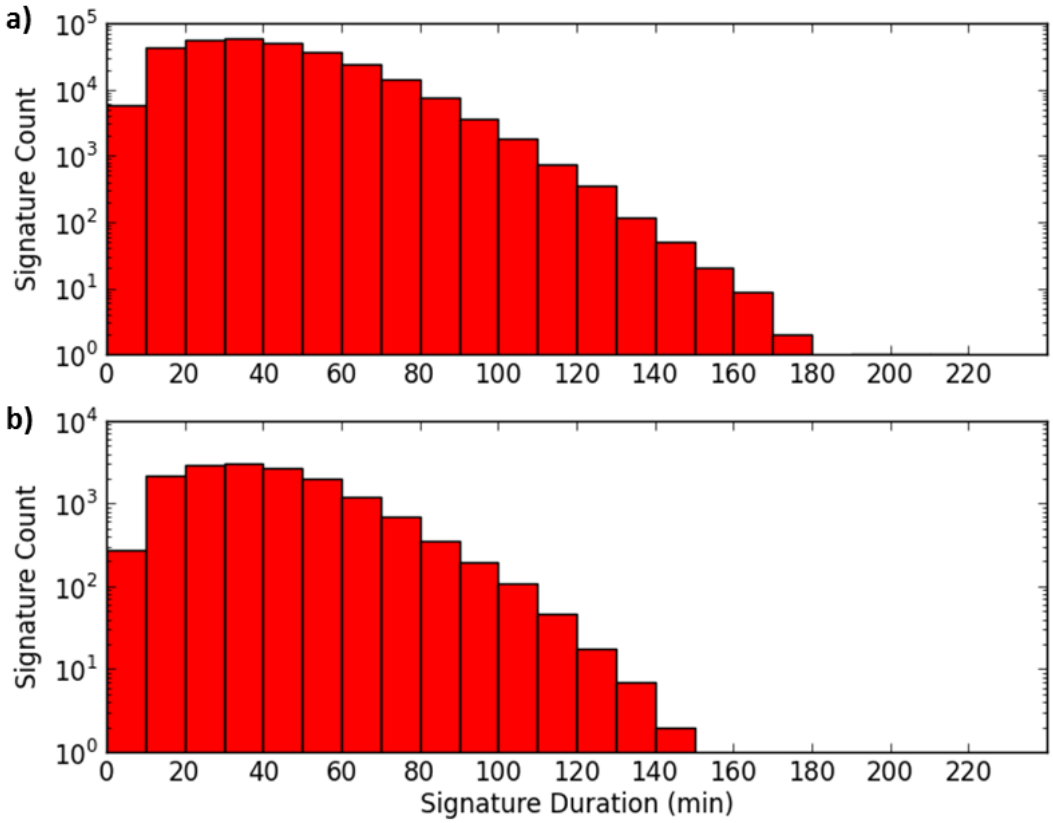

Fig. 3.24. (a) Mesoscale pressure signature frequencies as a function of signature temporal duration (min) for all signatures detected (pressure change magnitude exceeding 1 hPa). (b) As in (a) but for only large signatures (pressure change magnitude exceeding 3 hPa).

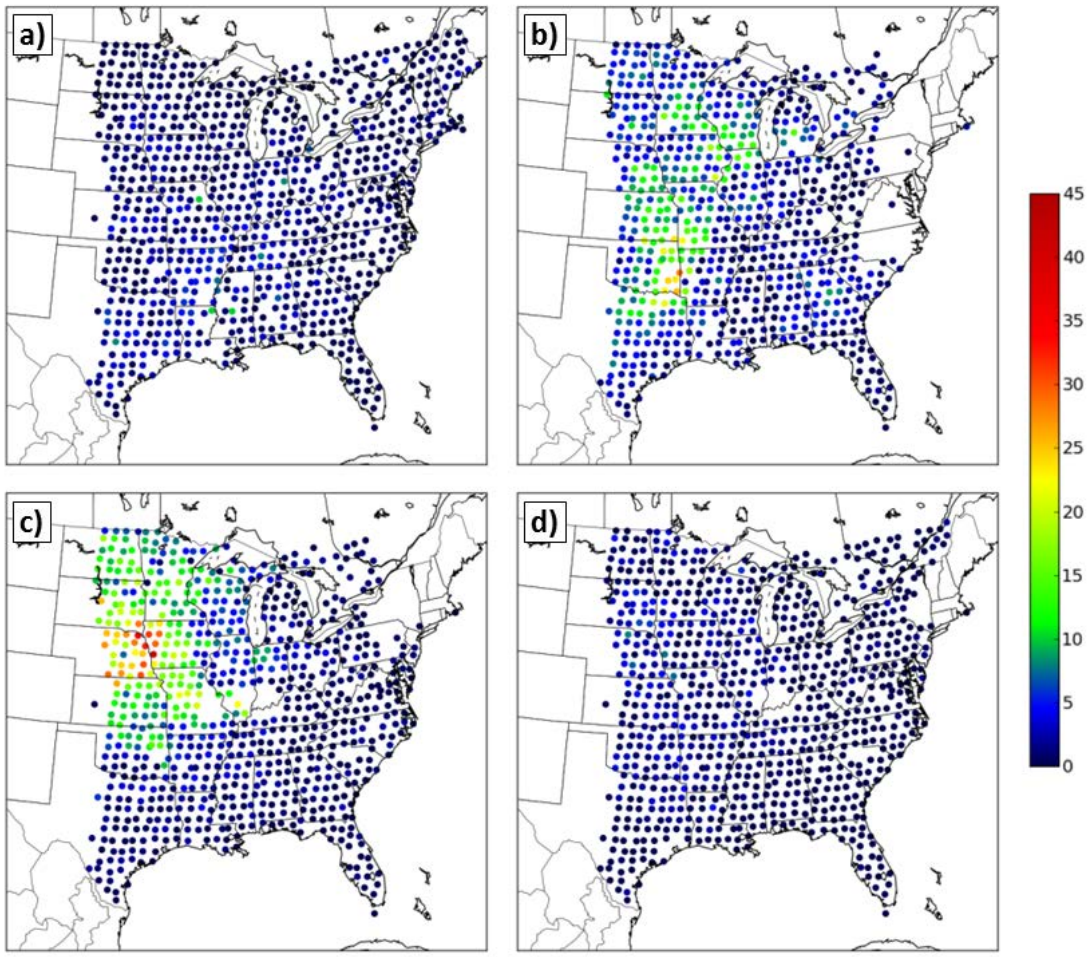

Fig. 3.25. As in Figure 3.21 except for mesoscale pressure signatures with pressure change magnitudes exceeding 3 hPa.

3.9 References

Adams-Selin, R. D., and R. H. Johnson, 2010: Mesoscale surface pressure and temperature features associated with bow echoes. *Mon. Wea. Rev.*, **138**, 212-227.

——, 2013: Examination of gravity waves associated with the 13 March 2003 bow echo. *Mon. Wea. Rev.*, **141**, 3735-3756.

Alexandersson, H., T. Schmith, K. Iden, and H. Tuomenvirta, 1998: Long-term variations of the storm climate over NW Europe. *Global Atmos. Ocean Syst.*, **6**, 97-120.

Bärring, L., and K. Fortuniak, 2009: Multi-indices analysis of southern Scandinavian storminess 1780–2005 and links to interdecadal variations in the NW Europe-North Sea region. *Int. J. Climatol.*, **29**, 373-384.

Bosart, L. F., W. E. Bracken, and A. Seimon, 1998: A study of cyclone mesoscale structure with emphasis on a large-amplitude inertia-gravity wave. *Mon. Wea. Rev.*, **126**, 1497-1527.

Carbone, R. E., J. D. Tuttle, D. A. Ahijevych, and S. B. Trier, 2002: Inferences of predictability associated with warm season precipitation episodes. *J. Atmos. Sci.*, **59**, 2033-2056.

Clark, P. A., K. A. Browning, C. J. Morcrette, A. M. Blyth, R. M. Forbes, B. Brooks, and F. Perry, 2014: The evolution of an MCS over southern England. Part 1: Observations. *Quart. J. Roy. Meteor. Soc.*, **140**, 439-457.

Coleman, T. A., and K. R. Knupp, 2009: Factors affecting surface wind speeds in gravity waves and wake lows. *Wea. Forecasting*, **24**, 1664-1679.

——, and K. R. Knupp, 2010: A nonlinear impedance relation for the surface winds in pressure disturbances. *J. Atmos. Sci.*, **67**, 3409-3422.

Crook, N. A., 1988: Trapping of low-level internal gravity waves. *J. Atmos. Sci.*, **45**, 1533-1541.

Dai, A., and J. Wang, 1999: Diurnal and semidiurnal tides in global surface pressure fields. *J. Atmos. Sci.*, **56**, 3874-3891.

de Groot-Hedlin, C. D., M. A. Hedlin, and K. T. Walker, 2014: Detection of gravity waves across the USArray: A case study. *Earth Planet. Sci. Lett.*, **42**, 12097.

de Pondeca, M., and Coauthors, 2011: The Real-Time Mesoscale Analysis at NOAA's National Centers for Environmental Prediction: Current status and development. *Wea. Forecasting*, **26**, 593-612.

Dirren, S., R. D. Torn, and G. J. Hakim, 2007: A data assimilation case study using a limited-area ensemble Kalman filter. *Mon. Wea. Rev.*, **135**, 1455-1473.

Einaudi, F., A. J. Bedard, and J. J. Finnigan, 1989: A climatology of gravity waves and other coherent disturbances at the Boulder Atmospheric Observatory during March–April 1984. *J. Atmos. Sci.,* **46**, 303-329.

Engerer, N. A., D. J. Stensrud, and M. C. Coniglio, 2008: Surface characteristics of observed cold pools. *Mon. Wea. Rev.*, **136**, 4839-4849.

Fujita, T. T., and H. A. Brown, 1958: A study of mesosystems and their radar echoes. *Bull. Amer. Meteor. Soc.*, **39**, 538-554.

Gaberšek, S., and D. R. Durran, 2006: Gap flows through idealized topography. Part II: Effects of rotation and surface friction. *J. Atmos. Sci.*, **63**, 2720-2739.

Geerts, B., Q. Miao, and J. C. Demko, 2008: Pressure perturbations and upslope flow over a heated, isolated mountain. *Mon. Wea. Rev.*, **136**, 4272-4288.

Grivet-Talocia, S., and F. Einaudi, 1998: Wavelet analysis of a microbarograph network. *IEEE Trans. Geosci. Remote Sens.,* **36,** 418-433.

—, —, W. L. Clark, R. D. Dennett, G. D. Nastrom, and T. E. VanZandt, 1999: A 4-yr climatology of pressure disturbances using a barometer network in central Illinois. *Mon. Wea. Rev.*, **127**, 1613-1629.

Horel, J., and Coauthors, 2002: Mesowest: Cooperative mesonets in the western United States. *Bull. Amer. Meteor. Soc.*, **83**, 211-225.

Jewett, B. F., M. K. Ramamurthy, and R. M. Rauber, 2003: Origin, evolution, and finescale structure of the St. Valentine's Day mesoscale gravity wave observed during STORM-FEST. Part III: Gravity wave genesis and the role of evaporation. *Mon. Wea. Rev.*, **131**, 617-633.

Johns, R. H., and W. D. Hirt, 1987: Derechos: Widespread convectively induced windstorms. *Wea. Forecasting*, **2**, 32-49.

Johnson, R. H., 2001: Surface mesohighs and mesolows. *Bull. Amer. Meteor. Soc.,* **82**, 13-31.

Jones, P. D., T. J. Osborn, and K. R. Briffa, 2003: Pressure-based measures of the North Atlantic Oscillation (NAO): A comparison and an assessment of changes in the strength of the NAO and in its influence on surface climate parameters. *The North Atlantic Oscillation: Climatic Significance and Environmental Impact*, J. W. Hurrell et al., Eds., Amer. Geophys. Union, 173-192.

Koch, S. E., and C. O'Handley, 1997: Operational forecasting and detection of mesoscale gravity waves. *Wea. Forecasting*, **12**, 253-281.

——, and L. M. Siedlarz, 1999: Mesoscale gravity waves and their environment in the central United States during STORM-FEST. *Mon. Wea. Rev.*, **127**, 2854-2879.

——, and S. Saleeby, 2001: An automated system for the analysis of gravity waves and other mesoscale phenomena. *Wea. Forecasting*, **16**, 661-679.

Koppel, L. L., L. F. Bosart, and D. Keyser, 2000: A 25-yr climatology of large-amplitude hourly surface pressure changes over the conterminous United States. *Mon. Wea. Rev.*, **128**, 51-68.

Krueger, O., and H. von Storch, 2012: The informational value of pressure-based single-station proxies for storm activity. *J. Atmos. Oceanic Technol.*, **29**, 569-580.

Lee, X., and A. G. Barr, 1998: Climatology of gravity waves in a forest. *Quart. J. Roy. Meteor. Soc.*, **124**, 1403-1419.

Li, Y., and R. B. Smith, 2010: The detection and significance of diurnal pressure and potential vorticity anomalies east of the Rockies. *J. Atmos. Sci.*, **67**, 2734-2751.

Madaus, L. E., G. J. Hakim, and C. F. Mass, 2014: Utility of dense pressure observations for improving mesoscale analyses and forecasts. *Mon Wea Rev.*, **142**, 2398-2413.

Markowski, P., and Y. Richardson, 2010: *Mesoscale Meteorology in Midlatitudes*. John Wiley & Sons, Ltd, 399 pp.

Mass, C. F., W. J. Steenburgh, and D. M. Schultz, 1991: Diurnal surface-pressure variations over the continental United States and the influence of sea level reduction. *Mon. Wea. Rev.*, **119**, 2814-2830.

——, and L.E. Madaus, 2014: Surface pressure observations from smartphones: A potential revolution for high-resolution weather prediction? *Bull. Amer. Meteor. Soc.*, **95**, 1343-1349.

Metz, N.D., and L.F. Bosart, 2010: Derecho and MCS development, evolution, and multiscale interactions during 3–5 July 2003. *Mon. Wea. Rev.*, **138**, 3048-3070.

National Weather Service Weather Forecast Office Blacksburg, VA, cited 2014: Squall line produces wind damage and large hail June 13th, 2013. Blacksburg, VA. [Available online at http://www.erh.noaa.gov/rnk/events/2013/June13th_SquallLine/summary.php.]

Nappo, C., 2002: *An Introduction to Atmospheric Gravity Waves*. International Geophysics Series, Vol. 85. Academic Press. San Diego, CA. 276 pp.

Nieto Ferreira, R., L. Hall, and T. M. Rickenbach, 2013: A climatology of the structure, evolution, and propagation of midlatitude cyclones in the southeast United States. *J. Climate*, **26**, 8406-8421.

Novak, D. R., and B. A. Colle, 2006: Observations of multiple sea breeze boundaries during an unseasonably warm day in metropolitan New York City. *Bull. Amer. Meteor. Soc.*, **87**, 169-174.

Orlanski, I., 1975: A rational subdivision of scales for atmospheric processes. *Bull. Amer. Meteor. Soc.*, **56**, 527-530.

Pavlis, G. L., K. Sigloch, S. Burdick, M. J. Fouch, and F. Vernon, 2012: Unraveling the geometry of the Farallon Plate: Synthesis of three-dimensional imaging results from the USArray, *Tectonophysics*, **532-535**, 82-102.

Ramamurthy, M. K., R. M. Rauber, B. P. Collins, and N. K. Malhotra, 1993: A comparative study of large-amplitude gravity-wave events. *Mon. Wea. Rev.*, **121**, 2951-2974.

Ray, R. D., and S. Poulose, 2005: Terdiurnal surface-pressure oscillations over the continental United States. *Mon. Wea. Rev.*, **133**, 2526-2534.

Reitan, C. H., 1974: Frequencies of cyclones and cyclogenesis for North America, 1951-1970. *Mon. Wea. Rev.*, **102**, 861-868.

Ruppert, J. H., and L. F. Bosart, 2014: A case study of the interaction of a mesoscale gravity wave with a mesoscale convective system. *Mon. Wea. Rev.*, **142**, 1403-1429.

Sanders, F., and J. R. Gyakum, 1980: Synoptic-dynamic climatology of the “bomb”. *Mon. Wea. Rev.*, **108**, 1589-1606.

Sutherland, B., 2010: *Internal Gravity Waves*. Cambridge University Press. Cambridge, UK. 377 pp.

Thomas, B. C., and J. E. Martin, 2007: A synoptic climatology and composite analysis of the Alberta clipper. *Wea. Forecasting*, **22**, 315-333.

Tian, W., D. J. Parker, S. Mobbs, M. Hill, C. A. D. Kilburn, and D. Ladd, 2004: Observing coherent boundary layer motions using remote sensing and surface pressure measurement. *J. Atmos. Oceanic Technol.*, **21**, 1481-1490.

Torrence, C., and G. P. Compo, 1998: A practical guide to wavelet analysis. *Bull. Amer. Meteor. Soc.*, **79**, 61-78.

Tyndall D., and J. Horel, 2013: Impacts of mesonet observations on meteorological surface analyses. *Wea. Forecasting*, **28**, 254-269.

Tytell, J. E., J. Eakins, and F. Vernon, 2011: Tracking outflows from severe thunderstorms using NSF EarthScope USArray pressure sensors. *Extended Abstracts. 24th Conf. on Weather and Forecasting/20th Conf. on Numerical Weather Prediction*, Seattle, WA, Amer. Meteor. Soc., 2A.3. [Available online at https://ams.confex.com/ams/91Annual/webprogram/Manuscript/Paper180739/AMS_2011_JonTytell_Extended_abstract.pdf.]

Vernon, F. L., J. E. Tytell, and J. Eakins, 2011: Tracking observations of weather phenomena by NSF EarthScope USArray seismic and pressure sensors. *Extended Abstracts. 24th Conf. on Weather and Forecasting/20th Conf. on Numerical Weather Prediction*, Seattle, WA, Amer. Meteor. Soc., P110. [Available online at https://ams.confex.com/ams/91Annual/webprogram/Manuscript/Paper180671/AMS_2011_FrankVernon_Extended_abstract.pdf.]

——, J. E. Tytell, B. Busby, J. Eakins, M. Hedlin, A. Muschinski, K. Walker, and B. Woodward, 2012: Scientific viability of the USArray Transportable Array network as a real-time weather monitoring platform. *Extended Abstracts. 16th Sym. on Met. Observation and Instrumentation*, New Orleans, LA, Amer. Meteor. Soc., 5.3. [Available online at https://ams.confex.com/ams/92Annual/webprogram/Manuscript/Paper200044/AMS_2012_FrankV_Extended_abstract.pdf.]

Wei, J., and F. Zhang, 2014: Mesoscale gravity waves in moist baroclinic jet–front systems. *J. Atmos. Sci.*, **71**, 929-952.

Wheatley, D. M., and D. J. Stensrud, 2010: The impact of assimilating surface pressure observations on severe weather events in a WRF mesoscale ensemble system. *Mon. Wea. Rev.*, **138**, 1673-1694.

Whitaker, J. S., G. P. Compo, X. Wei, and T. M. Hamill, 2004: Reanalysis without radiosondes using ensemble data assimilation. *Mon. Wea. Rev.*, **132**, 1190-1200.

Viana, S., E. Terradellas, and C. Yagüe, 2010: Analysis of gravity waves generated at the top of a drainage flow. *J. Atmos. Sci.*, **67**, 3949-3966.

Yang, Y., and M. H. Ritzwoller, 2008: Teleseismic surface wave tomography in the western U.S. using the transportable array component of USArray. *Geophys. Res. Lett.*, **35**, L04308.

Zishka, K. M., and P. J. Smith, 1980: The climatology of cyclones and anticyclones over North America and surrounding ocean environs for January and July, 1950-77. *Mon. Wea. Rev.*, **108**, 387-401.

CHAPTER 4

ASSESSMENT OF 2011 SPRING AND SUMMER MESOSCALE PRESSURE PERTURBATIONS DETECTED BY THE USARRAY

4.1 Abstract

Mesoscale phenomena, including inertial gravity waves and convective systems, induce pressure perturbations that can alter the strength and magnitude of surface winds, precipitation, and other forms of sensible weather. In some instances, large-magnitude perturbations can produce winds capable of surpassing severe criteria, resulting in concerns for damage to life and property. The research presented in this chapter extends the work conducted in Chapter 3 to identify and characterize prominent pressure perturbations using a unique resource of 1-Hz pressure observations available from the USArray Transportable Array (TA) seismic field campaign that took place across the continental United States.

Using hourly gridded surface pressure from the Real Time Mesoscale Analysis (RTMA) to serve as background fields, the uniformly (~70 km) spaced TA platform observations are incorporated using a two-dimensional variational technique to produce surface pressure analysis grids at temporal frequencies of 5 min and spatial resolution of 5 km from 1 March – 31 August 2011 over the domain covered by TA. Band-pass filtering techniques and feature tracking algorithms are employed to identify prominent

mesoscale pressure perturbations and their properties. Two case studies, one involving mesoscale convective systems and another involving a solitary gravity wave, are shown. Aggregate summary statistics for all detected features over the period sampled indicated a majority of perturbations last for less than 3 h, produce maximum perturbation magnitudes between 2-5 hPa, and move at speeds ranging from 15-35 m s^{-1}. Perturbation occurrence frequencies and their assessed characteristics support previous climatologies of assessed large-amplitude pressure signatures as well as case studies of gravity waves and convective systems. Further, the results show clear potential for utilization of high temporal resolution observations in combination with high spatial resolution to detect mesoscale features such as large-amplitude inertial gravity waves.

4.2 Introduction

Improving the analysis and prediction of mesoscale weather phenomena remains a key goal of atmospheric research. Many prominent mesoscale phenomena, whether present at the surface or aloft within the troposphere, lead to pressure perturbations that can be sensed by surface-based sensors and extracted by temporally removing diurnal, synoptic, and seasonal-scale fluctuations in the measured time series (Chapter 3). Such phenomena at shorter time scales (less than 12 h) include processes within the surface boundary layer (Tian et al. 2004), terrain-induced flows (Gaberšek and Durran 2006; Viana et al. 2010), and differential surface heating (Novak and Colle 2006; Geerts et al. 2008). Many of these processes occur frequently but are not associated with events with high impact concerns for the majority of the population.

However, other mesoscale processes, such as large-amplitude gravity waves and

convective systems, can result in very large pressure perturbations coupled with other sensible weather impacts. Mesoscale convective systems (MCSs), in particular bow echoes and derechos, are often associated with very strong positive mesoscale perturbations induced by the development and maintenance of a local mesohigh within the system such that the leading edge of the perturbation is often associated with strong damaging winds (Przybylinski 1995; Evans and Doswell 2001; Engerer et al. 2008; Metz and Bosart 2010). Following the mesohigh, larger MCSs often have a wake low feature typically characterized by a large negative mesoscale pressure perturbation. While typically less potent, occasionally severe winds are generated towards the back of these wake lows (Loehrer and Johnson 1995). The severe winds produced by such wake low events typically receive less attention due to being relatively rare and less often accompanied by other severe weather concerns compared to mesohighs, which may be associated with damaging hail and flooding in addition to strong winds (Loehrer and Johnson 1995; Coleman and Knupp 2009).

Large-amplitude mesoscale gravity waves have also been extensively studied. The movement, amplification, and decay of such features through generally stable environments has often been a focus for research (Bosart and Seimon 1988; Crook 1988; Ramamurthy et al. 1993; Zhang et al. 2001; Plougonven and Zhang 2014). Additionally, their impacts on precipitation generation or suppression (Bosart et al. 1998), wind field amplification or modification (Bosart and Seimon 1988; Schneider 1990), and convection initiation (Ruppert and Bosart 2014) have also been examined, mainly through analysis of case events that had large impacts. On occasion some large events can enhance the synoptic wind field such that severe criteria can be surpassed (Schneider 1990). While

large-magnitude gravity waves may have significant impacts on winds and convection, they remain difficult to identify and forecast using currently available conventional surface weather observations and numerical guidance.

A suite of observational and numerical resources have been utilized to identify and categorize mesoscale weather features that produce large pressure fluctuations. However, studies have generally focused more on the high wind speeds, rain, hail, and other weather phenomena that attend high-impact weather episodes rather than the associated large pressure fluctuations. In most cases, detailed analyses of perturbation pressure fields have focused on specific cases. Several studies have used time series analysis techniques including frequency filtering (Koch and O'Handley 1997; Koch and Saleeby 2001; Jacques et al. 2015) and wavelet analysis (Grivet-Talocia and Einaudi 1998; Grivet-Talocia et al. 1999) of surface pressure data to isolate the specific pressure perturbation features. Time-to-space conversion techniques have been employed to identify the propagation of such features (Koch and O'Handley 1997; Koch and Saleeby 2001). Phase speeds for features such as MCS and inertial gravity waves are usually within 15-35 m s^{-1} (Koppel et al. 2000). Cases have also been documented involving gravity waves that have moved near or above the upper bound of 35 m s^{-1} (Bosart et al. 1998; Adams-Selin and Johnson 2013).

Other studies have taken more holistic approaches to produce regional climatologies of prominent mesoscale feature occurrences. Koppel et al. (2000) created a 25-year climatology of large pressure fluctuations across the continental United States to identify prominent locations for mesoscale and inertial gravity wave activity. However, Koppel et al. (2000) were restricted by the 1-hr temporal resolution of the available

pressure observations. Bentley et al. (2000) generated a 10-year climatology of derecho events across the northern and central United States from 1986-1995, focusing on feature characteristics and the general synoptic environment to identify typical conditions for formation. A longer, more recent (1996-2013) climatology of derechos was catalogued by Guastini and Bosart (2016), identifying 256 unique events.

Several of the above climatologies relied upon subjective analysis to identify unique characteristics that describe the particular feature of interest. However, objective feature identification and tracking has also been utilized through various methodologies to identify and track synoptic-scale features (König et al. 1993; Hodges 1994; Hoskins and Hodges 2002; Hodges et al. 2003; Raible et al. 2008; Kravtsov et al. 2015).

At the mesoscale and microscale, radar-based algorithms such as the Storm Cell Identification and Tracking (SCIT, Johnson et al. 1998) and Tornado Vortex Signature (TVS, Brown and Wood 2012) algorithms have been employed to identify thunderstorms and storm cell features. Advancements in using satellite imagery to identify and track individual cloud features (e.g., Liu et al. 2014) have also been conducted using image cross-correlation techniques. Within the numerical weather prediction community, the development of the Method for Object-Based Diagnostic Evaluation (MODE) has been a prominent tool for forecast verification (Davis et al. 2006; Davis et al. 2009). MODE utilizes fuzzy logic routines to match regions of forecasted quantities with observed or verification dataset quantities to objectively verify a forecast. An extension known as MODE Time Domain (MODE-TD) incorporates the ability to follow a detected feature over time and assess properties such as speed and direction, in addition to nontemporal properties such as areal extent (Bullock 2011). MODE and MODE-TD have been

utilized for verification of mesoscale features in many studies (Bullock 2011; Mittermaier and Bullock 2013; Clark et al. 2014; McMillen and Steenburgh 2015).

Within the computing science and image processing disciplines, methodologies have taken correlative approaches to match features across time by considering the scalar field (in this case the pressure perturbation data) as an isosurface, where positive perturbations constitute “mountains” and negative perturbations “valleys”. Tracking graphs and merge-split hierarchal trees are then computed as the features morph and move for different scalar thresholds (Bremer et al. 2010; Widanagamaachchi et al. 2012).

Research has also been conducted using surface pressure observations for data assimilation into numerical weather prediction models to improve accuracy regarding mesoscale features. Advancements in aggregation and dissemination of surface observations, such as those via MesoWest (Horel et al. 2002), have made surface observational data outside of conventional observations (including atmospheric pressure) much more readily available. Lacking the representativeness errors other state variables can contain, atmospheric pressure data are a much more viable candidate for data assimilation from diverse resources. This includes nontraditional resources for pressure data such as mobile phones (Mass and Madaus 2014). Typical errors of pressure observations arise from unavailable or inaccurate metadata, instrument error, or propagation of errors due to conversion of the measurement to sea level or other elevations (Mohr 2004). Surface pressure also can provide additional vertical information regarding propagation of nonsurface atmospheric waves, further enhancing its use (Madaus et al. 2014; Lei and Anderson 2014). Surface pressure data or their derived forms (e.g., corrected sea-level pressure and pressure tendency) have been used

in many reanalysis and data assimilation studies. Numerical reanalysis projects, including the 20th Century Reanalysis Project, utilized archived pressure observations to provide more accurate representation of past phenomena (Whitaker et al. 2004; Compo et al. 2006; Compo et al. 2011). Data assimilation studies with a focus on improving forecasting at the global and mesoscale levels have also used pressure observations (Anderson et al. 2005; Ingleby 2014; Lei and Anderson 2014; Madaus et al. 2014).

Pertinent to this work is a unique resource of high temporal resolution pressure observations originating from an extensive field campaign within the geosciences. As part of the National Science Foundation EarthScope initiative, over 400 surface-based instrument platforms were deployed in a Cartesian-type fashion across the western portion of the continental United States (CONUS) beginning in 2004 (Tytell et al. 2016). Platforms reported for 1-2 years, after which the western-most units were retrieved, repaired, and redeployed further east of the main grid. This initiative, known as the USArray Transportable Array (TA), was designed to provide geoscientists with a detailed dataset of the subsurface to better understand the North American continent (Tytell et al. 2016). The retrieval and redeployment of platforms farther east results in a "temporal rolling" appearance across the CONUS from 2004-2015, where the majority of stations were retrieved along the eastern CONUS in 2015. Atmospheric pressure sensors, reporting at 1 and 40 Hz, were installed in late 2009 while the TA was located over the central US to aid in identifying signals in seismic observations induced by nonseismic phenomena (de Groot-Hedlin et al. 2008; Hedlin et al. 2010; Hedlin et al. 2012; de Groot-Hedlin et al. 2014). Figure 4.1 illustrates the positions of the primary TA deployment during the March-April-May (MAM) and June-July-August (JJA) seasons of 2011, the

period of interest for this study. Chapter 1 provides the full distribution of TA stations with pressure sensors from 1 Jan 2010 – 22 Jul 2016, including platforms that are presently being installed in Alaska and the adjacent Canadian provinces.

Time series analyses on a per station basis were executed for TA data collected between 1 Jan 2010 – 28 Feb 2014 by Jacques et al. (2015) to assess the distribution of mesoscale (10 min - 4 h), subsynoptic (4 - 30 h), and synoptic (30 h - 5 day) pressure fluctuations as a function of geographic location and season. The resultant mesoscale analyses indicated a prominent region of mesoscale activity across the central portion of the CONUS, consistent with past climatologies of MCSs and some gravity wave case studies. Mesoscale signature frequencies, defined as the pressure rises (falls) associated with the existing perturbations, also occurred most frequently during the spring (MAM) and summer (JJA) months.

Since the time series analyses conducted by Jacques et al. (2015) treated all resultant signatures as independent events, they were not able to characterize perturbation size, speed, direction, and other characteristics of features rippling across the TA domain. This work extends the analyses conducted by Jacques et al. (2015) to identify and characterize mesoscale perturbations, focusing on the most prominent period of mesoscale activity the TA detected from 1 Mar – 31 Aug 2011. Section 4.3 details both the observational and gridded datasets as well as the methods to merge the observations and grids together into analyses at high spatial and temporal frequencies. Section 4.3 also outlines the temporal filtering and feature detection and tracking procedures to assess the resultant mesoscale perturbations. Section 4.4 provides a review of two contrasting case events, highlighting the identification and tracking of the pressure perturbations with

respect to additional data resources. Section 4.5 aggregates and describes all of the detected mesoscale features in terms of geographic origin, feature size, perturbation magnitude, phase speed, and direction. Finally, Section 4.6 provides additional conclusions on the results and discussion on how this work may provide further future evaluations of perturbations produced by mesoscale phenomena.

4.3 Data and Methods

4.3.1 Data Resources

4.3.1.1 TA Observations

Described further by Tytell et al. (2016), the TA stations contained several different pressure sensors within their vault system, including the Setra-278 pressure transducer. Tubing extending from the vault allowed for adequate sampling of the atmospheric surface pressure. Data from the Setra-278 were recorded and available at interval rates of 1 and 40 Hz. Jacques et al. (2016) describe the methods used to collect and archive data in an efficient format from the Incorporated Research Institutions for Seismology (IRIS) systems. Further, archives from 1 Jan 2010 – 31 Dec 2015 are available as a dataset via the Research Data Archive at the National Center for Atmospheric Research (Jacques et al. 2016). The same archived pressure observations can also be visualized via several web products (http://meso1.chpc.utah.edu/usarray) developed as a part of the time series analysis work (Jacques et al. 2015).

Advantages for using the TA in this research include the uniformity of instrumentation, deployment methods used across the sites, temporal resolution, and data quality. Jacques et al. (2015) provide information on the objective rate-of-change checks

of 2 hPa s^{-1} (2 hPa min^{-1}) used to indicate suspect (or potentially suspect) periods of data for each TA site. Results from these objective checks, in combination with subjective checks for incorrect data or metadata, are stored as temporal start and end periods of suspect data. Thus, no actual data are removed from the archives; they are simply ignored for any subsequent analyses. Sensor performance for the TA in general from 1 Jan 2010 – 31 Dec 2015 is very high, with a median 99.79% uptime per site (Jacques et al. 2016). When considering suspect observations, this median value only drops to 99.68%. Problems were typically limited to just a few sites with recurring issues due to sensor power or inlet tubing concerns (Jacques et al. 2016).

4.3.1.2 Real Time Mesoscale Analysis Grids

The TA observations provide enhanced temporal resolution compared to many other conventional datasets that are readily accessible. Additionally, the uniformity of the spatial distribution of the TA is a unique property compared to conventional and other observation networks that tend to be clustered in more urban areas (Tyndall and Horel 2013). However, the spatial resolution of the TA (~70 km) is neither perfectly regular nor adequate on its own for spatial assessment for all mesoscale features with typical length scales varying between 50-500 km. Thus, another resource with higher spatial resolution was required.

The NOAA Real Time Mesoscale Analysis (RTMA) product is used to provide surface pressure data on a regular grid with 5 km horizontal resolution and 1 h temporal resolution from 1 Mar – 31 Aug 2011. During the period of interest, the RTMA pressure grids were created by using a 1 h surface pressure forecast from the Rapid Update Cycle

(RUC) model (de Pondeca et al. 2011). According to Benjamin et al. (2007), the RTMA grids were created by interpolating from the RUC 13-km horizontal resolution to 5 km and then executing a process to incorporate surface observations to produce hourly analysis grids. Metadata information, including a 5-km grid of surface elevation, was also available for deriving sea-level pressure. TA observations from 2011 were not incorporated into any RTMA analyses and hence represent an independent dataset for this study. Beginning Mar 2012, TA observations were made available in real time via MesoWest to NOAA entities, and thus could be incorporated into the RTMA procedures (Jacques et al. 2016)

4.3.1.3 Ancillary Datasets

To better illustrate some of the findings of this research, additional datasets are leveraged. Radar reflectively imagery mosaics, courtesy of the Iowa Environmental Mesonet, are acquired to align mesoscale pressure perturbation features with ongoing precipitation activity. For select case studies, web-based analysis products for the 40-km North American Regional Reanalysis (NARR) are obtained from Pennsylvania State University's e-WALL web-based system. Atmospheric soundings are acquired to assess the vertical stability for selected events, as the vertical structure of the atmosphere is known to help maintain and sometimes amplify propagating atmospheric gravity waves (e.g., Ruppert and Bosart 2014). Finally, in situ temperature, dewpoint, and wind observations are also acquired using data available in MesoWest (Horel et al. 2002).

Severe thunderstorm and nonthunderstorm wind reports are acquired from the National Climatic Data Center (NCDC) publication *Storm Data*. While it is well

documented that *Storm Data* wind and damage reports can be problematic (Trapp et al. 2006; Smith et al. 2013), the reports have been heavily used in previous works to assist in identification and classification of severe weather events (e.g., Coniglio et al. 2004; Ashley and Mote 2005). The *Storm Data* reports are used here to assist in classification of mesoscale perturbation features associated with either severe wind speeds or wind damage reported within spatial and temporal boundaries of the feature existence.

4.3.2 Five Minute Analysis Generation

Figure 4.2 summarizes the steps utilized to generate the analysis dataset used in this study to identify prominent mesoscale pressure features. Blending of the RTMA surface pressure grids with TA observations is necessary to generate a dataset with high enough spatial and temporal resolution to better assess mesoscale features. Due to some temporal inconsistencies with the hourly grids (potentially due to inaccurate depiction of mesoscale features in the RUC 1 h forecasts when compared to incorporated observations), the grids are corrected as necessary through temporally filtering inconsistencies in the RTMA analyses that would have been mesoscale perturbation noise in the final dataset. Corrected grids are interpolated using a cubic spline from hourly to 5-min intervals for the entire 6-month period to increase their temporal resolution, where the cubic spline provides a higher order, and perhaps more realistic, estimation of pressure variations between hours compared to a linear interpolation scheme. As shown in Figure 4.1, the positioning of the main portion of the TA from 1 Mar – 31 Aug 2011 was located across the Great Plains of the CONUS, stretching from the Canadian border south to the western Gulf of Mexico coastline. Post-quality-controlled observations,

initially at a sampling interval of 1 Hz, are subsampled to 5 min to match the temporal resolution of the gridded datasets.

The gridded and observational datasets are blended together using a two-dimensional variational technique. The University of Utah Two Dimensional Variational Analysis (UU2DVAR), further described by Tyndall and Horel (2013), generates analysis grids for several state variables using observations and numerical analysis grids. The model grids function as a "background first guess" with assumed error covariances, while errors for the observations are also assigned based on knowledge of instrumentation reliability, representativeness, and other factors. Using the innovations between the background values interpolated to the observation locations and the observations, an analysis grid is produced by adjusting the background grids by those innovations (Tyndall and Horel 2013). The extent the observations result in analysis modifications is in part dependent on several tunable parameters within UU2DVAR. The first is the observation to background error covariance ratio, which describes a measure of "trust" in the observations with respect to the background first guess field (where a larger ratio means less trust in the observations). The second is the horizontal decorrelation length scale, which defines the horizontal extent beyond an observation location where the observation can influence the analysis. The influence decreases exponentially beyond the observation location and asymptotes to zero beyond the defined length. Similarly, a vertical decorrelation length scale can also be defined to restrict vertical influence if desired (Tyndall and Horel 2013).

A modified version of the UU2DVAR technique is applied for use with these datasets. In order to remove concerns regarding mismatches or inaccuracies in

observation and numerical grid elevation data, the numerical grids and observations are converted from surface pressure into 5 min pressure tendency. The vertical decorrelation length scale of the background error covariance is increased to a value so that terrain elevation influences on the analysis were removed. A horizontal decorrelation length scale of 80 km is used, slightly larger than the spatial resolution of the TA. The observation to background error covariance ratios are set to unity for the TA sites, implying that the observations are trusted to the same degree as the background grids.

At each 5-min interval, the UU2DVAR technique is applied to generate an analysis grid of 5-min pressure tendency using the interpolated RTMA background grids and the TA observations. Pressure tendency analysis grids are converted back to standard surface pressure once the analysis grid generation is complete. Thus, the primary dataset used for identification of mesoscale features is a gridded analysis dataset at 5-km spatial resolution and 5-min temporal resolution for the entire 6-month period and region of interest.

4.3.3 Temporal Filtering and Feature Identification

Similar to Jacques et al. (2015), temporal band-pass filtering techniques are utilized to isolate mesoscale pressure perturbations. A Butterworth band-pass filter with period bounds corresponding to 10 min and 12 h is applied to each time series at every analysis grid point to produce a second dataset of filtered analysis grids at 5-min intervals. Grids are also used before 1 Mar 2011 and after 31 Aug 2011 to allow the filtering technique to produce mesoscale pressure perturbations at the bounds of the 6-month period. The filtered analysis grids are stored with the surface pressure analyses for

comparison. Figure 4.3 provides an example of the final analysis and band-pass filtered grids for 0200 UTC 27 Jun 2011 centered over Iowa, with MCS activity ongoing.

Prominent mesoscale features are first identified for each analysis grid independently. Beginning with principals similar to how numerical forecast and observed grids have been evaluated (e.g., Clark et al. 2014), regions of mesoscale activity are identified as areas of conjoined grid cells where a pressure perturbation larger than 1 hPa in absolute magnitude was detected. Attributes, including the areal extent of the 1-hPa absolute magnitude region, are calculated for each independent region.

Similar to Hoskins and Hodges (2002), the dataset utilized here has already been filtered to isolate the specific frequencies of interest. For this study, an iterative approach is utilized to temporally match detected regions of interest over successive analysis grids. Temporal matching is first conducted using analysis grids separated by only 5 min. Given the feature sizes of interest, grid spatial resolution (5 km), temporal resolution (5 min), and climatological propagation speeds of such features (15-35 m s^{-1}), it was expected that propagating features would encompass a large region of the same horizontal space over periods of 20 min or less. Thus, an overlap approach is applied to match like regions of interest between timestamps as the same feature, similar to the spatiotemporal overlap approaches that have been utilized in feature detection algorithms for both radar (e.g., Johnson et al. 1998; Jung and Lee 2015) and MODE-TD (e.g., Bullock 2011; Clark et al. 2014).

For situations when splitting and merging of features occur in this dataset, feature centroid distance to the location of maximum magnitude is utilized as a means to determine those features that continue, form, or dissipate. After initial features are

matched between successive analysis grids, this same process is executed for grids 10, 15, and 20 min apart. This allows for additional detection and tracking of features that occasionally fall below the 1-hPa threshold for a small period of their lifetime but are clearly the same feature as previously discovered. Subjective reviews with ancillary datasets are also conducted to address situations where merging and splitting features appeared to be unphysical. An identification schema for each feature is compiled using unique identifiers, similar to how radar algorithms keep track of individual thunderstorm cells (Johnson et al. 1998).

Prominent mesoscale features are defined as those with an absolute perturbation magnitude of at least 1 hPa, detected for at least 1 h, and with an areal extent of at least 10,000 km^2 at some point during their existence. The temporal and spatial thresholds are defined to help isolate instances of large magnitude events that could be accurately assessed and tracked using the analyses. Feature metrics, including feature geographic centroid position, maximum absolute magnitude position, maximum absolute pressure perturbation magnitude, and other statistics, are saved for each prominent feature at each 5-min interval of its existence.

An adaptation of the methodology used by MODE-TD is applied to determine feature speed and direction. As described by Bullock (2011), the MODE-TD tool utilizes information for the feature in question across all horizontal (x, y) and temporal (t) periods. Using a linear regression technique, components of velocity u (v) can be determined through statistical relationships generated with x (y) and t. An adaptation to the technique is applied here to allow the speed and direction of a feature to vary with time. For a given timestamp, only position and time information for a feature within 30

min are utilized to determine the particular phase speed and direction at that timestamp. This allows for the identified features to change direction, speed up, and slow down, which is often seen with mesoscale systems that move large distances and through varying environments.

4.4 Case Studies

4.4.1 Event Overviews

To demonstrate the technique to identify and track large mesoscale pressure perturbation features, two cases are chosen within the 1 Mar – 31 Aug 2011 period. An initial constraint for these cases is that the phenomena of interest are required to remain within the longitudinal bounds of the primary array of TA stations for the majority of their existence, which according to Figure 4.1 requires perturbations to be located within the Great Plains region of the central CONUS. Due to the orientation of the TA deployment, the two cases have phenomena with a substantive meridional propagation component so they can be assessed across the TA domain for longer periods of time.

The first case involves the development and movement of two successive MCS complexes that formed overnight on 11 Aug 2011 over the northern and central Great Plains. The second case involves a mesoscale gravity wave that formed in association with the synoptic system responsible for a deadly tornado outbreak across the southeastern CONUS on 27 Apr 2011, when the negative perturbation associated with the gravity wave propagated northward away from the primary synoptic system and across much of the Great Plains region. For each case, a discussion of the synoptic environment using reanalysis grids, conventional surface observations, and upper-air soundings is

provided. Mesoscale pressure perturbation identification and tracking for each event is then discussed using the feature identification results, radar imagery, and TA band-pass filtered pressure perturbations. Finally, the impact of each case on surface wind fields is assessed using conventional surface observations and reports courtesy of *Storm Data* when appropriate.

4.4.2 11-12 August 2011 Successive Northern Plains MCS Events

4.4.2.1 Environment Synopsis

The analysis for this case focuses on two semilinear convective complexes that initially formed over South Dakota and moved to the southeast over several hours into Nebraska and western Iowa before continuing southeast at varying intensities into northeast Kansas and northwest Missouri. NARR analysis at 1800 UTC 11 Aug 2011, a few hours prior to the organization of the first MCS, shows mid-level geostrophic flow at 700 (Fig. 4.4c) and 500 (Fig. 4.4a) hPa from west-northwest to northwest across the central to northern Great Plains. Geostrophic southerly flow at low levels (Fig. 4.4b,d) appears to be southerly across the north-central Great Plains based on the surface region of high pressure centered across Illinois. Finally, a digging shortwave trough was quickly propagating into Montana at this time (Fig. 4.4a), serving as a potential source to organize convection upstream of the trough location.

Figure 4.5 depicts air temperature, dewpoint, and wind observations from surface-based National Weather Service (NWS) Automated Surface and Weather Observing System (ASOS/AWOS) and Bureau of Land Management Remote Automated Weather Station (RAWS) platforms at 1800 UTC 11 Aug 2011. A clear southerly surface flow

can be assessed across much of eastern and central Nebraska and South Dakota with temperatures ≥ 25 ºC and relatively high dewpoints ≥ 16 ºC. Thus, a warm and moist low-level environment is in place. The 0000 UTC 12 Aug 2011 atmospheric soundings from Aberdeen, South Dakota (Fig. 4.6a) and North Platte, Nebraska (Fig. 4.6b) show elevated Convective Available Potential Energy (CAPE) values in excess of 1500 and 2400 J kg^{-1}, respectively. Both soundings exhibit the presence of low-mid-level wind shear supporting the development of organized multicellular structures as well as drier mid-levels (600-700 hPa) that support enhanced downdrafts (e.g., Coniglio et al. 2011). Further, the North Platte sounding had a veering wind profile in the low levels (Fig. 4.6b), indicating the potential for convective development with some potential for updraft rotation. Perhaps most noticeable is the presence of a strong low-level capping inversion in Figure 4.6b, which likely prevented any surface-based convective development upstream of the first complex. The Rapid City, South Dakota sounding at 0000 UTC 12 Aug 2011 (Fig. 4.7) illustrates the environment behind the initiation point of the first MCS, which took place over central South Dakota shortly before this time. Elevated CAPE values over 1800 J kg^{-1} are present, as is a low-level capping inversion that likely precluded additional convective development until the second MCS complex developed several hours later.

4.4.2.2 Perturbation Feature Analysis

The first MCS initially forms over central South Dakota and then organizes and moves southeastward into the western periphery of the deployed TA. By 0100 UTC 12 Aug 2011, the complex forms a classic bow echo structure (Fig. 4.8a). A region of

positive mesoscale pressure perturbations lies near the apex of the bow echo, where the expected mesohigh would reside, and several TA stations, including J32A (Parkston, SD), experience large positive mesoscale pressure perturbations (Fig. 4.9a).

By 0400 UTC (Fig. 4.8b), the first MCS expands, with the detected mesohigh expanding as well. The dashed red line shows the general movement of the feature through assessment of feature speed and direction every 5 min using the modified MODE-TD-based technique described in Section 4.3.3. The median speed for this assessed mesohigh feature is 22.4 m s^{-1} traveling in a generally southeast direction. Initial detection of a wake low feature also occurs at 0400 UTC associated with the northern mesovortex that developed as a part of this MCS (Fig. 4.8b). Large negative pressure perturbations are recorded at TA stations such as H33A near Clear Lake, South Dakota (Fig. 4.9b). Initial generation of the second MCS can also begin to be detected at 0400 UTC in South Dakota west of the TA deployment.

The first MCS continues moving south-southeastward and by 0900 UTC lies over northeastern Kansas and northwest Missouri, with a large positive mesoscale pressure perturbation still in place. The eastern edge of the bow echo has significantly weakened while the southern and southwestern edges of the complex continued to maintain strength and move south. The weakened portion of the MCS can still be seen via radar in southern Minnesota at 0900 UTC (Fig. 4.8c), though the region of positive mesoscale pressure perturbations has weakened, as shown by the TA observations. The remaining prominent mesohigh region instead shifted southwest to accompany the stronger convection associated with the western portion of the original complex. The western edges of the complex have begun to weaken as well, but the positive mesoscale pressure

perturbation remains intact along the general outflow boundary of the complex as seen in Figure 4.8c. Further, a wake low feature is well established behind the first MCS, as indicated by a collocated track (blue dashed line) behind the mesohigh track (red dashed line) with a similar median speed of 22.1 m s^{-1}. The second MCS has also formed and is beginning to move into the bounds of the TA domain.

The large mesohigh region with the first MCS dissipates and is no longer detected by 1200 UTC (Fig. 4.8d). The negative pressure perturbation associated with the trailing wake low region remains. The positive perturbation associated with the second complex expands in coverage as the system propagates farther into the TA domain with a median speed of 20.8 m s^{-1}, despite this complex remaining less organized than the first, with a smaller leading line of convection and larger stratiform region remaining further back over much of eastern Nebraska. Stations K32A and M33A in northeast and east-central Nebraska, respectively, show the passage of the first MCS mesohigh, wake low, and second complex mesohigh structures quite well via time series of pressure perturbation observations (Fig. 4.9).

4.4.2.3 Surface Wind Impacts

Examination of NWS and RAWS observations yields wind gusts for both complexes that were approaching, if not surpassing, NWS severe wind criteria of 25.9 m s^{-1}. Figure 4.10 shows wind observations at 0415 UTC during the first complex passage near the intersection of Nebraska, Iowa, and South Dakota. Wind direction observations are as expected along the boundaries of the leading convective line, with a peak wind gust of 24 m s^{-1} recorded at ASOS station KODX (Ord, NE) along the southwestern edge.

However, winds backing from southerly to easterly with time can be seen behind the initial convective line in association with the wake low region, with an equally intense 24 m s^{-1} wind gust recorded by ASOS station KBKX (Brookings Municipal Airport, SD) on the back edge of the precipitation associated with the first MCS. Figure 4.11 shows surface observations for 1200 UTC in association with the second complex, with a 24 m s^{-1} peak wind gust recorded at ASOS site KLNK (Lincoln Municipal Airport, NE).

Although the first MCS presents a classic bow echo structure, wind damage reports via *Storm Data* are not extensive (not shown). Most of the wind damage reports are focused in central South Dakota when the complex first initiated and also when individual cells formed on the southwestern tail end of the complex between 0100-0300 UTC 12 Aug 2011. A few tornado reports are also found along this southwestern tip. The second MCS produced a few wind reports in Nebraska, though once again they are not extensive (not shown).

4.4.3 26-27 April 2011 Propagating Mesoscale Gravity Wave

4.4.3.1 Environment Synopsis

The second case involves the development of a mesoscale gravity wave across the south-central CONUS which propagated northward through the majority of the TA domain early (0000-0600 UTC) 27 Apr 2011. The wave originated as a strong negative pressure perturbation across southeast Oklahoma. The feature moved northward through the central Great Plains as a fairly intense negative pressure perturbation, where it was sampled well by the TA stations. The wave maintained amplitude until reaching the northern portion of the Great Plains, where it then began to dissipate.

The general synoptic environment that was present during the generation of this feature has been reviewed extensively, as the same synoptic setup was in place during an extremely devastating and deadly tornado outbreak that occurred across Alabama and surrounding states later on 27 Apr 2011 (Knupp et al. 2014; Yussouf et al. 2015). Through analyzing NARR analysis data at 0000 UTC 27 Apr 2011, strong positive vorticity advection can be inferred in the highlighted region centered on northern Texas (Fig. 4.12a) as short-wave troughs propagate through the slightly negatively tilted longwave trough across the central CONUS. The development of a surface cyclone over northeastern Texas is shown in Figure 4.12b. The general flow direction at the 850 (700) hPa levels (Figs. 4.12c-d) near the generation point of the wave in southeast Oklahoma is southerly (southwesterly).

Surface observations at 2100 UTC 26 Apr 2011, with annotated surface low pressure and warm frontal boundary, are given in Figure 4.13. The surface boundary appears to provide a focal point for convective initiation that occurs simultaneously with gravity wave generation. South of the boundary, southerly flow from the Gulf of Mexico draws a warm and moist surface air mass into Louisiana, Mississippi, and Alabama. North of the boundary cooler air exists, with general northeasterly flow. Further north, the surface flow becomes quite complicated, with strong southwesterly winds across Missouri and Illinois, whereas across Kansas and Oklahoma winds relax and reverse to southeasterly and northeasterly, respectively.

Knupp et al. (2014) provide an in-depth sounding analysis of the upper level environment associated with the warm sector of the synoptic system, including reviews of instability and shear parameters that supported the development of supercells

associated with the tornadic outbreak. The soundings provided here (Fig. 4.14) focus on the environment upstream of the mesoscale gravity wave generation region. The 0000 UTC 27 Apr 2011 sounding at Springfield, Missouri indicates an inversion layer between 900-800 hPa, with weaker stability aloft from 800-600 hPa (Fig. 4.14a). Winds within the inversion layer were generally light, while above the inversion layer strong south-southwesterly flow can be seen. Further north at Topeka, Kansas (Fig. 4.14b) the inversion layer is higher (based just below 800 hPa) and sharper but remained surmounted by a layer of weaker stability above. Winds within the thin inversion layer are relatively light, with west-southwesterly flow observed in the above layer of weaker stability. The Omaha, Nebraska sounding (Fig. 4.14c) depicts an inversion layer beginning just below 750 hPa with a layer of weaker stability above the inversion. Winds were northwest backing to westerly through the inversion layer and the layer above. Finally, the 0000 UTC sounding recorded at Chanhassen, Minnesota no longer has a sharp inversion layer present, with northeasterly flow backing to northwesterly dominating the lower and mid-levels (Fig. 4.14d).

Previous literature (Lindzen and Tung 1976; Bosart et al. 1998; Ruppert and Bosart 2014) has described wave ducting through the presence of an inversion layer as well as a potential critical level in the layer above the inversion. The combination of a strong stable inversion layer with a critical level above the inversion layer (in a layer of weaker stability) can lead to the trapping and ducting of vertically propagating gravity waves, allowing for the feature to maintain strength and in some cases amplify. As shown in Figure 4.15, the general movement of the negative pressure perturbation associated with the gravity wave (blue contoured region and blue dashed feature track) is

northerly. Reviewing the upper-air sounding winds, flow within the layer above the inversion has a large zonal component as opposed to meridional at Topeka and Omaha (Figs. 4.14b-c), resulting in very low magnitudes of flow component in the direction of wave propagation. This may have aided in the development of a critical level which could maintain wave amplitude as the feature moved northward. The Chanhassen sounding (Fig. 4.14d) no longer has a well-established inversion layer and opposing flow, likely explaining the dissipation of the wave as it continued to move north into Minnesota.

4.4.3.2 Perturbation Feature Analysis

Convective initiation within the warm sector of the synoptic system begins around 2000 UTC 26 Apr 2011 in southern Arkansas, as seen on radar imagery (Fig. 4.15a). By 2200 UTC (Fig. 4.15b) convection continues to develop near the surface boundary structure identified in Figure 4.13 in Arkansas, southeastern Oklahoma, and northeastern Texas. Coincident with the convective initiation was the generation of a large negative mesoscale pressure perturbation in southeastern Oklahoma, signifying the birth of the mesoscale gravity wave. It is unclear whether this perturbation was responsible for the convective initiation or vice versa, as described in previous cases (e.g., Bosart et al. 1998). The gravity wave expands and moves north through much of the TA across eastern Kansas, Missouri, and into Iowa from 0000-0400 UTC 27 Apr 2011 (Figs. 4.15c-e). Precipitation is not associated with this northward-moving feature compared to other stronger gravity wave cases that have modified precipitation distributions (e.g., Ruppert and Bosart 2014; Jacques et al. 2015). This feature moves rather quickly, with a median

speed of 36.6 m s^{-1} when computed using the modified MODE-TD speed algorithm. By 0600 UTC, the feature begins to dissipate as it moves into Minnesota (Fig. 4.15f).

Pressure perturbation time series at several TA sites along the path of the gravity wave depict the negative mesoscale perturbation experienced as the wave passes (Fig. 4.16). TA station P36A northwest of Atchison, Kansas depicts the sharpest pressure decrease associated with the wave (Fig. 4.16a), with subsequent TA stations further north (Figs. 4.16b-d) showing the sharpness of the pressure fall and overall wave amplitude decreasing, implying weakening of the feature over time.

4.4.3.3 Surface Wind Impacts

The gravity wave was not intense enough to produce any wind damage impacts, although surface winds were modified as the wave propagated northward. While not critical from a life or property endangerment standpoint, the wave did move through a region of the CONUS where wind turbines are abundant. Thus, identification and tracking of these features have potential applications within the wind energy industry for identification of potential wind ramp (increase and decrease) events, impacting power production and costs.

Figure 4.17 provides ASOS/AWOS and RAWS surface wind observations in conjunction with the detected gravity wave from 0200-0500 UTC 27 Apr 2011. Wave passage is coincident with enhancement of north-northwesterly winds as it translated north (e.g., northwestern Iowa; Figs. 4.17c-d), but of perhaps greater impact was the relaxing of wind speeds behind the gravity wave. In some cases the winds relaxed from gusting 5-8 m s^{-1} during the gravity wave passage (Missouri and Kansas; Fig 4.17a) to

near calm conditions just an hour later (Fig 4.17b).

4.5 Summary Statistics

4.5.1 Feature Occurrences

All mesoscale pressure perturbation features lasting at least 1 h and having spatial coverage exceeding 10,000 km^2 at one point during their lifetime are considered "prominent" features and are included in the aggregated statistics described here. Table 4.1 provides a monthly summary of detected events for the 627 unique features identified from 1 Mar – 31 Aug 2011. June is the most active month for prominent mesoscale features over the TA domain, with 156 features detected (24.9%). April, May, and August are also active, with July (12.0%) and March (5.4%) exhibiting the fewest features across the TA domain. Roughly equal numbers of positive and negative pressure perturbations are identified. Using *Storm Data* wind reports, features are considered associated with strong winds if the reports occurred within 50 km of the feature boundaries and within 30 min of the feature existence time, to allow for some of the ambiguity concerning the time and location of the wind reports (Trapp et al. 2006). Using these thresholds, 294 (46.9%) of the detected features are associated with *Storm Data* wind reports.

Figure 4.18 highlights the regions of the TA domain where the features are detected. For each 5-km grid cell, the number of unique perturbation feature events are shown over the period of record assessed (1 Mar – 31 Aug 2011). In the context of the area contained by the TA stations (see Fig. 4.1), a region of enhanced activity extends from South Dakota/Iowa southward to Oklahoma/Arkansas, where over 35 unique

features are evaluated at each 5-km grid cell. The maximum number of occurrences is across eastern Kansas and western Missouri, with over 80 unique features. The distribution relates well to the station-based climatology for this period presented by Jacques et al. (2015), despite the methodology differences and variations in filtering parameters. Considering the climatologies of gravity waves (e.g., Koppel et al. 2000) and derecho-type events (e.g., Bentley et al. 2000; Guastini and Bosart 2016), maxima across the central Great Plains were also expected.

Figure 4.19 summarizes the features during spring (MAM) and summer (JJA). A clear latitudinal shift can be seen as the majority of events in spring 2011 are concentrated across the central and southern Great Plains, compared to summer 2011, when prominent mesoscale features were relatively rare south of northern Oklahoma. The summer months of 2011 were also generally more active than the spring months, as evidenced by the accrued statistics in Table 4.1 and distribution of event occurrences in Figure 4.19b. This seasonal shift also follows the well-known climatological shift of severe weather events away from the southeast and south central CONUS in spring to the central and north central CONUS during summer. The two case studies in Section 4.4 illustrate this well, with the 26-27 Apr 2011 gravity wave event indirectly associated with a deadly tornado outbreak across the southeast CONUS and the 11-12 Aug 2011 MCS events located across the north central CONUS.

Positive and negative pressure perturbations (Fig. 4.20) have relatively similar frequencies. This result is not surprising since coupling of positive and negative pressure perturbations are often seen for events that produce both mesohigh and wake low-type structures, as shown by the 11-12 Aug 2011 MCS case (Section 4.4.2). Figure 4.21

shows a similar breakdown for events associated with strong wind reports from *Storm Data*. An increase in the number of events associated with strong wind reports is seen in Figure 4.21a, despite the aggregate total of features with and without strong wind reports being similar (Table 4.1). This discrepancy may arise from both the geographic location and areal coverage of the features with strong wind reports, where spatial extent is considered for the results in Figure 4.21 but not in Table 4.1.

Figure 4.22 provides a monthly distribution of propagating feature tracks for positive (red) and negative (blue) events. Distinct patterns and seasonal shifts can be assessed. For example, during April and May (Figs. 4.22b-c) most features are generated in the south-central to central CONUS and then move in a general southwest to northeast direction. This is not uncommon for mid-to-late-spring convective episodes often tied to developing synoptic systems over the Great Plains, where convection initiates in the warm sector and moves east to northeast along or near established baroclinic zones under general southwest flow. Mesoscale and inertial gravity wave events also typically have similar propagation patterns given their preferred area of genesis relative to synoptic systems (e.g., Koppel et al. 2000). In contrast, a shift to the north and change in orientation of the tracks is evident from July to August (Figs. 4.22e-f). Clear northwest to southeast patterns are seen in August, providing evidence that events similar to the 11-12 Aug 2011 MCS cases (Section 4.4.2) dominate this portion of the study period.

4.5.2 Characteristic Distributions

A further breakdown of prominent feature characteristics was conducted for 1 Mar – 31 Aug 2011 using histograms. Figure 4.23 summarizes the lifetime of detected

features. Most of the features last for less than 3 h (72.9%), with an additional 21.4% of detected features lasting from 3-6 h. Features lasting greater than 6 h are composed of primarily long-lived MCS events moving across the TA domain with consistent pressure perturbations. The two case studies examined earlier are a part of this latter group of features, with the gravity wave lasting 7.4 h (97th percentile) and the mesohigh of the primary MCS lasting 10.1 h (99th percentile).

Figure 4.24 summarizes the maximum amplitude of each feature based on band-pass filtered (10 min - 12 h) perturbation data for TA stations within the spatial bounds of each feature. Distributions for both positive (Fig. 4.24a) and negative (Fig. 4.24b) features are generally similar, with many features having a maximum observed perturbation magnitude of 2-4 hPa. Band-pass filtered perturbations with magnitudes larger than 5 hPa are relatively rare for both positive (7.3% of positive perturbations) and negative (9.7%) events.

Figure 4.25 illustrates the maximum areal extent of the detected features. As anticipated, features with smaller areal extent are more common, with 70.5% less than 40,000 km^2 and only 5.3% larger than 80,000 km^2 during their lifetime. The prominent mesohigh found in the 11-12 Aug 2011 MCS events achieved a maximum areal extent of 62,556 km^2, placing it in the 87th percentile of this distribution. The 26-27 Apr 2011 gravity wave is within the 99th percentile (128,078 km^2).

Summarizing the total distance traveled by the features (Fig. 4.26), most moved fewer than 200 km. The distance traveled is calculated by assessing the movement of the feature every 5 min. The combination of shorter lifespan (Fig. 4.23) and small propagation velocity (Section 4.5.3) is in part responsible for the majority moving less

than 200 km. Very few events (5.3%) propagate further than 500 km, many of which relate well with features with longer duration periods (not shown). An extreme case for this period was the 26-27 Apr 2011 gravity wave, which moved 1,140 km away from its generation point, the maximum distance assessed for any feature in this study.

4.5.3 Feature Speeds and Directions

The distributions of median speed and direction for all assessed mesoscale features are provided in Figure 4.27. Consistent with phase speeds noted in the literature, 76.1% of the features have a median speed between 15-35 m s^{-1}. Features with median speeds less than 15 m s^{-1} (greater than 35 m s^{-1}) comprise 11.2% (12.7%) of the distribution, respectively. A general eastward progression of the features is also evident (Fig. 4.27b), with most features moving in a general eastward to southeastward direction, with northeasterly movement a secondary maximum. Few features have a median direction over their lifespan that was northwesterly during this period.

Rather than summarizing only one general speed and direction for each feature, the speeds and directions of features during their entire lifetime are also determined (Fig. 4.28) as they varied over their lifespan. All calculated feature speeds and directions are collected and binned into geographic sectors over the TA domain based on their geographic centroid location. Normalized feature speed and direction roses are created for each sector to quantify the distribution of speeds and directions of features within that region and time period (features that last longer or remain in a particular sector may be weighted more heavily in this analysis). As summarized overall in Figure 4.28, speeds of 15-35 m s^{-1} occur the most frequently in all sectors and for all movement directions.

Interesting variations in favored directions are evident as well. For example, features in the northeast sector of the TA domain appear to favor propagation directions that are northeasterly to easterly, whereas further west and south an easterly to southeasterly propagation direction is favored.

Figure 4.29 provides similar roses for datasets limited to positive and negative perturbation events. Most noticeable is the shift in preferred directions across the northern sectors, where positive perturbations favor east to southeast directions (Fig. 4.29a) and negative perturbations favor east to northeast movement (Fig. 4.29b). This is likely related to phenomena type, where the prominent positive perturbations are more associated with convective systems such as the MCS events of 11-12 Aug 2011 (propagated southeast) and the negative events are more associated with gravity wave-like features such as the 26-27 Apr 2011 case (propagated north). Directional variation is less noticeable for several of the southern sectors. Some increase in speed is noticed for negative perturbations, with more instances falling within the 35-55 m s^{-1} region of the normalized roses.

Figure 4.30 depicts the propagation speeds divided by season with spring (MAM) and summer (JJA) in Figures 4.30a and 4.30b, respectively. Shifts in preferred direction are seen in all sectors between the two seasons, with east-northeast movement preferred in spring and east-southeast movement during summer. These results follow the monthly distributions of feature tracks, as shown in Figure 4.22. Also noticeable is a decrease in speeds from spring to summer, with fewer features moving above 35 m s^{-1} at some point in their lifetime in summer compared to spring. This result could be related to the general lack of established synoptic mid-to-upper-level flow during the summer months,

with mesoscale processes instead being the more dominant phenomena under generally quiescent synoptic conditions across the Great Plains.

4.6 Summary and Discussion

Prominent mesoscale pressure perturbation features, some of which were associated with high-impact sensible weather phenomena, are assessed for the 1 Mar – 31 Aug 2011 period across the central conterminous United States through the combination of two distinct resources of surface pressure data. Observations at 1-Hz temporal resolution are collected from sensors deployed as part of the USArray TA seismic field campaign, which was located across the central CONUS during the study period (Fig. 4.1). While having very high temporal resolution and excellent data quality, the spatial resolution of the TA deployments (~70 km) was not sufficient for a more complete assessment of propagating pressure perturbations produced by phenomena such as mesoscale gravity waves, inertial gravity waves, and MCS events. Thus, hourly RTMA surface pressure analyses, at 5-km horizontal resolution, are incorporated as an additional resource of background surface pressure data due to the increased spatial resolution.

As described in Fig. 4.2, the background grids (1-Hz observations) are quality controlled and then interpolated (subsampled) to 5-min intervals to match the temporal resolution between the two resources. Background grids and observations are converted to 5-min tendency values to avoid elevation discrepancies between the observation platforms and gridded terrain. A set of 5-min tendency analysis grids is computed by blending the background grids and observations using a modified version of UU2DVAR (Tyndall and Horel 2013). Conversion of the analysis grids back to surface pressure

results in a set of surface pressure grids that incorporates the observations sensed by the TA stations, available every 5 min for the period of interest. Temporal band-pass filtering (10 min – 12 h) of the analysis grids isolates perturbations produced by prominent mesoscale phenomena. A perturbation feature tracking algorithm, based on principles employed by other algorithms used for various meteorological datasets (e.g., MODE-TD), is developed to isolate prominent mesoscale perturbation features over the region of interest and evaluate their characteristics over time (e.g., propagation speed and direction). Two case studies of differing mesoscale phenomena are described with respect to their atmospheric environments in Section 4.4. Distributions of characteristics for all detected features are assessed as a function of location, season, and other properties in Section 4.5.

The results shown in this study highlight the advantages of using both surface observations and numerical gridded products in a cohesive manner to better evaluate the detection and propagation of such mesoscale features, which may or may not be accompanied by variations in other sensible weather fields (e.g., temperature, wind, or precipitation). Surface pressure observation networks typically have adequate temporal resolution (20 min or less between recordings) to provide an accurate depiction of the passage of a mesoscale feature, with the TA dataset a case of very fine temporal resolution (1 Hz). However, the observations themselves often lack the spatial distribution (e.g., horizontal spacing such as the TA uniformity of ~70 km, urban clustering, etc.) required to properly assess feature spatial characteristics. In contrast, numerical analysis grids provide adequate spatial resolution (5 km or less) but typically lack better temporal resolution (at best 1 h). This approach produces a dataset

highlighting the advantages of both (5 km horizontal; 5 min temporal).

The two case studies in Section 4.4 provide examples of inherently different phenomena (MCS and gravity waves) that are assessed with a filtered analysis grid dataset and adequate feature detection and tracking algorithm. The 11-12 Aug 2011 MCS features evaluated in the first case (Figs. 4.8, 4.10, 4.11) highlight the ability to detect and track mature mesohighs and wake lows. While conventional techniques have often focused on identification and tracking of feature boundaries to signify feature propagation (e.g., Ruppert and Bosart 2014), the perturbations associated with the first MCS highlight an example where the dynamically evolving nature of a large MCS leads to shifts and variations in the perturbation speed and direction, as shown in Fig. 4.8. The algorithm developed here considers those deviations, resulting in the nonlinear tracks that better explain the movement of such features. The 26-27 Apr 2011 gravity wave case (Figs. 4.15 and 4.17) provides an example where a coherent mesoscale feature can be tracked for long distances and time periods while still remaining collocated with fluctuations in other surface measurements (e.g., surface wind variations shown in Fig. 4.17), despite general broadening of the feature as shown in the time series of TA stations (Fig. 4.16).

The aggregate statistics for all prominent mesoscale features detected and described in Section 4.5 are consistent with climatologies derived for various mesoscale phenomena types (Koppel et al. 2000; Bentley et al. 2000; Guastini and Bosart 2016) as well as specific case studies (Bosart and Seimon 1988; Schneider 1990; Bosart et al. 1998; Ruppert and Bosart 2014). With regards to Koppel et al. (2000), which assessed 25 years of mesoscale pressure features but was restricted by observation temporal

resolution, this study identifies many more prominent mesoscale pressure perturbations (primarily due to higher temporal resolution TA observations) despite a shorter period and restricted geographic region of assessment (6 months over the central CONUS). Further, the results build upon Jacques et al. (2015) by applying a more Lagrangian perspective to the mesoscale perturbations detected by each TA station when using a more Eulerian approach. Rather than assess perturbation rises and falls at each site to categorize mesoscale feature frequency, these results provide three-dimensional (x, y, t) information assessing both feature occurrences, which were geographically consistent with the results of Jacques et al. (2015), as well as spatial properties, including preferred movement characteristics (i.e., speed and direction). Table 4.1 and Figures 4.18-4.21 all provide general conclusions that mesoscale feature occurrences during the spring and summer of 2011, within the deployment region of the TA, were most frequent across the central Great Plains region of the CONUS. Feature propagation tracks (Fig. 4.22) show the seasonal transitions from spring convection and east-northeastward gravity wave propagation to summer easterly and southeasterly propagating MCS events as the general positioning of the jet stream shifts north and ridging dominates the southern Great Plains. Histograms of lifetime (Fig. 4.23), maximum areal coverage (Fig. 4.25), and distance traveled (Fig. 4.26) show that many of the detected features have brief lifespans (less than 3 h), small areal extent (less than 40,000 km^2), and short propagation distances (less than 200 km), with the case studies of Section 4.4 being more extreme cases. According to perturbation data from the TA stations, many of the detected features had maximum pressure perturbations from 2-4 hPa, with very few events exceeding 5 hPa in perturbation magnitude irregardless of sign.

The calculated phase speeds and directions of the assessed features agree well with the few perturbation climatologies and multiple case studies in the literature, of which most assessed the general speeds of mesoscale features to be within 15-35 m s^{-1}. The histograms of median propagation speeds (Fig. 4.27a) place over 76% of the detected features within those limits. Roses computed from speeds and directions evaluated for features over their entire lifetime show the geographic (Fig. 4.28), pressure magnitude sign (Fig. 4.29), and seasonal (Fig. 4.30) variations in speeds and directions. Those results support previous work describing general speed and direction characteristics for MCS, derecho, and large-magnitude gravity wave phenomena (Bosart et al. 1998; Koppel et al. 2000; Adams-Selin and Johnson 2013).

The algorithms and results demonstrated here highlight the potential for further research and development of additional enhanced algorithms for more accurate detection of mesoscale pressure perturbations that can, directly or indirectly, result in impacts on life, property, and industry. The location and temporal period of this study were restricted by the deployment strategy of the TA. As the TA migrated eastward after Aug 2011, the frequency of mesoscale pressure perturbations decreased as described by Jacques et al. (2015), resulting in a smaller sample size, despite large-magnitude inertial gravity waves also occurring from the Great Lakes eastward as well (Bosart et al. 1998; Koppel et al. 2000). Future research to expand geographic and temporal boundaries could involve the incorporation of additional observational resources, provided the temporal resolution of the observational data is sufficient. Further, the development and enhancements of the RTMA post-2011, and the introduction and utilization of the High Resolution Rapid Refresh (HRRR) numerical weather prediction model, provide

additional resources to more accurately depict mesoscale features.

Automated gravity wave detection algorithms have been explored previously in several studies (Koch and O'Handley 1997; Koch and Saleeby 2001). However, those studies highlight issues associated with acquiring real-time observations with adequate temporal resolution as well as the time required to process and detect mesoscale features. As described in Section 4.2, the addition of pressure observations from additional resources should be more simplistic due to fewer concerns about representativeness of the data. Inclusion of wind observations from trusted resources and analysis grids should also be considered to better isolate high-impact events through analysis of both mesoscale wind and pressure perturbations, in addition to other resources such as radar imagery for events that modulate precipitation. Conventional ASOS/AWOS observations, while available in an archived state at sufficient temporal resolution, are presently not widely distributed with adequate temporal resolution to more accurately evaluate such events. Advances in dissemination of higher temporal resolution ASOS/AWOS observations (e.g., 5 min temporal resolution), incorporation of other observational datasets and numerical gridded products such as the RTMA or HRRR, and continual advancements in computing power make the automated operational detection of mesoscale features much more realistic.

4.7 Acknowledgements

Funding for this research was provided by National Science Foundation Grant 1252315. USArray pressure data access was provided by the Incorporated Research Institutions of Seismology Web Services and the Array Network Facility at Scripps

Institution of Oceanography, University of California San Diego. Access to RMTA surface pressure grids was courtesy of web products available via the National Centers for Environmental Prediction. NARR reanalysis imagery, atmospheric sounding imagery, and radar imagery were from web services courtesy of Pennsylvania State University, University of Wyoming, and Iowa Environmental Mesonet. Surface weather observations provided via API services courtesy of MesoWest/SynopticLabs. The authors acknowledge the University of Utah Center for High Performance Computing (CHPC) for computational hardware and software.

Table 4.1. Prominent mesoscale pressure perturbation feature counts (percentages) were detected from 1 Mar – 31 Aug 2011 over the TA domain, by month and the period totals. Row columns indicate total perturbations, positive and negative perturbations, and perturbations associated and not associated with *StormData* wind reports. Percentages are relative to total number of features for each time period shown, with the exception of the first row, which is relative to 627 total features detected.

Description	**Mar**	**Apr**	**May**	**Jun**	**Jul**	**Aug**	**Total**
Perturbation Features	34 (5)	119 (19)	117 (19)	156 (25)	75 (12)	126 (20)	627 (100)
Positive	12 (35)	54 (45)	61 (52)	78 (50)	43 (57)	65 (52)	313 (50)
Negative	22 (65)	65 (55)	56 (48)	78 (50)	32 (43)	61 (48)	314 (50)
StormData Winds	8 (24)	50 (42)	61 (52)	80 (51)	34 (45)	61 (48)	294 (47)
No *StormData* Winds	26 (76)	69 (58)	56 (48)	76 (49)	41 (55)	65 (52)	333 (53)

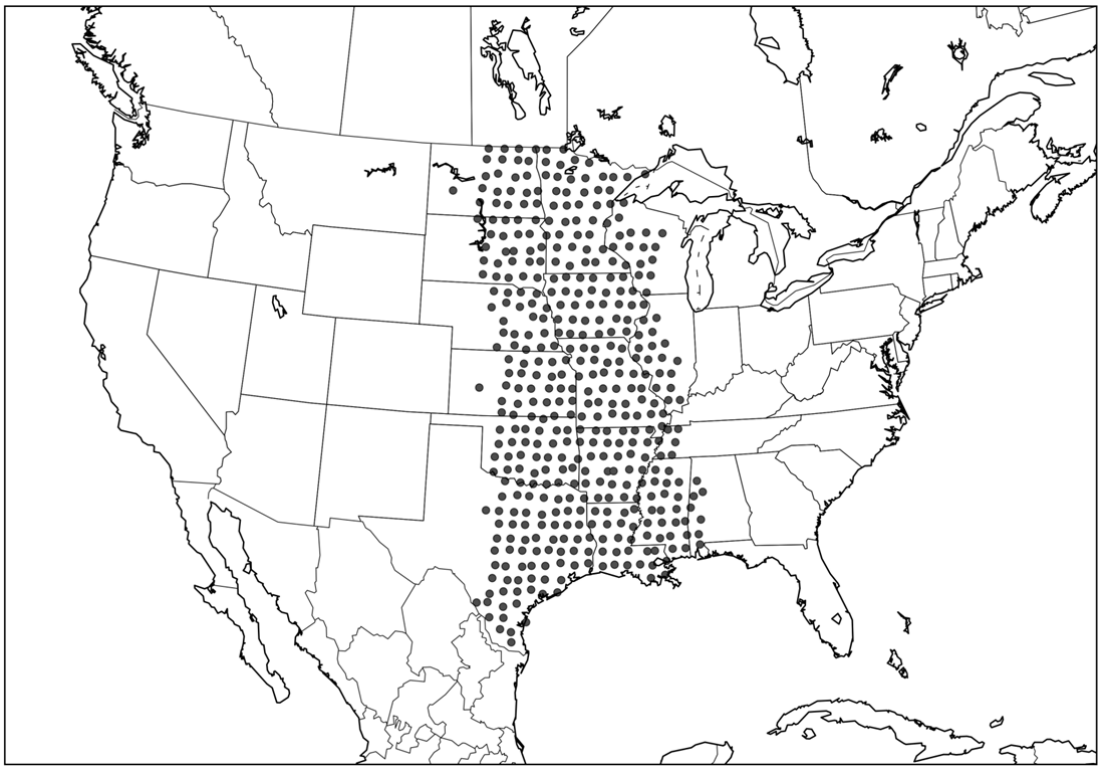

Fig. 4.1. Locations of primary TA platforms with pressure observations from 1 Mar 2011 – 31 Aug 2011.

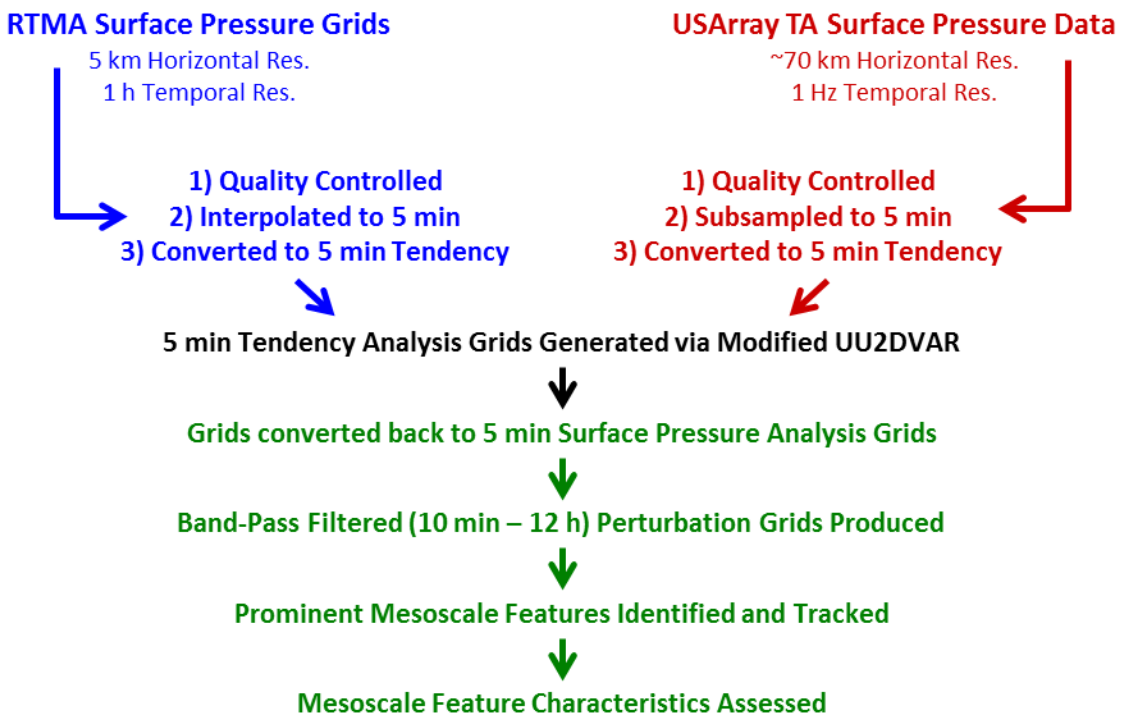

Fig. 4.2. Flowchart of the analysis methodology outlined in Section 4.3, summarizing the steps taken to produce the 5-min pressure analysis grids used in this study, band-pass filtering to isolate mesoscale perturbations, and steps to identify and track mesoscale pressure perturbation features.

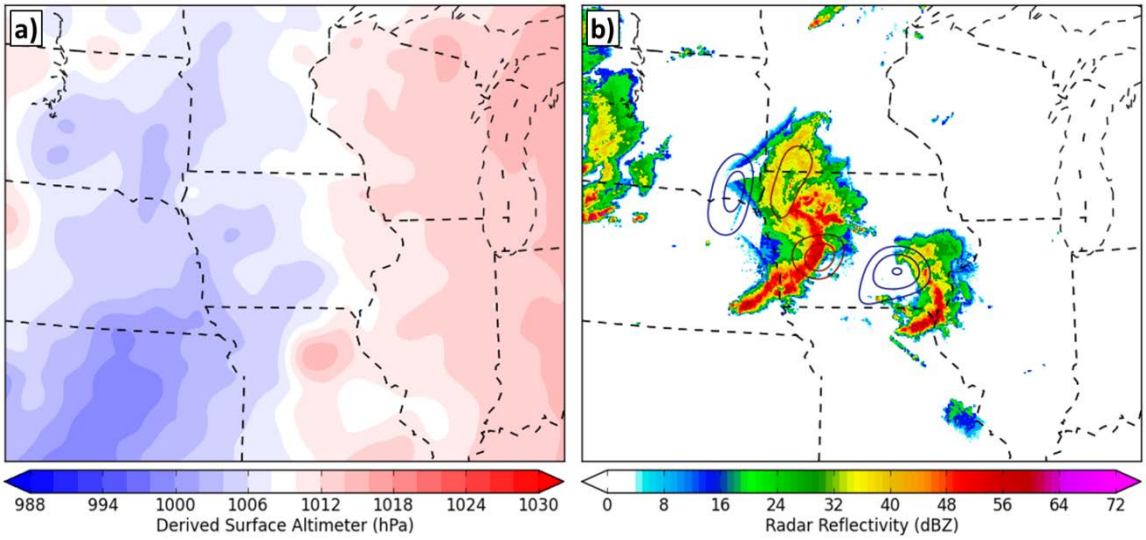

Fig. 4.3. (a) Gridded analysis of derived surface altimeter centered on northern Iowa at 0200 UTC 27 Jun 2011. (b) Base radar reflectivity with contours of band-pass filtered (10 min - 12 h) mesoscale pressure perturbations across the same region at 0200 UTC 27 Jun 2011. Perturbation contours at 0.5 hPa are shown in dark red (blue) for positive (negative) perturbations. Radar reflectivity imagery courtesy the Iowa Environmental Mesonet web services.

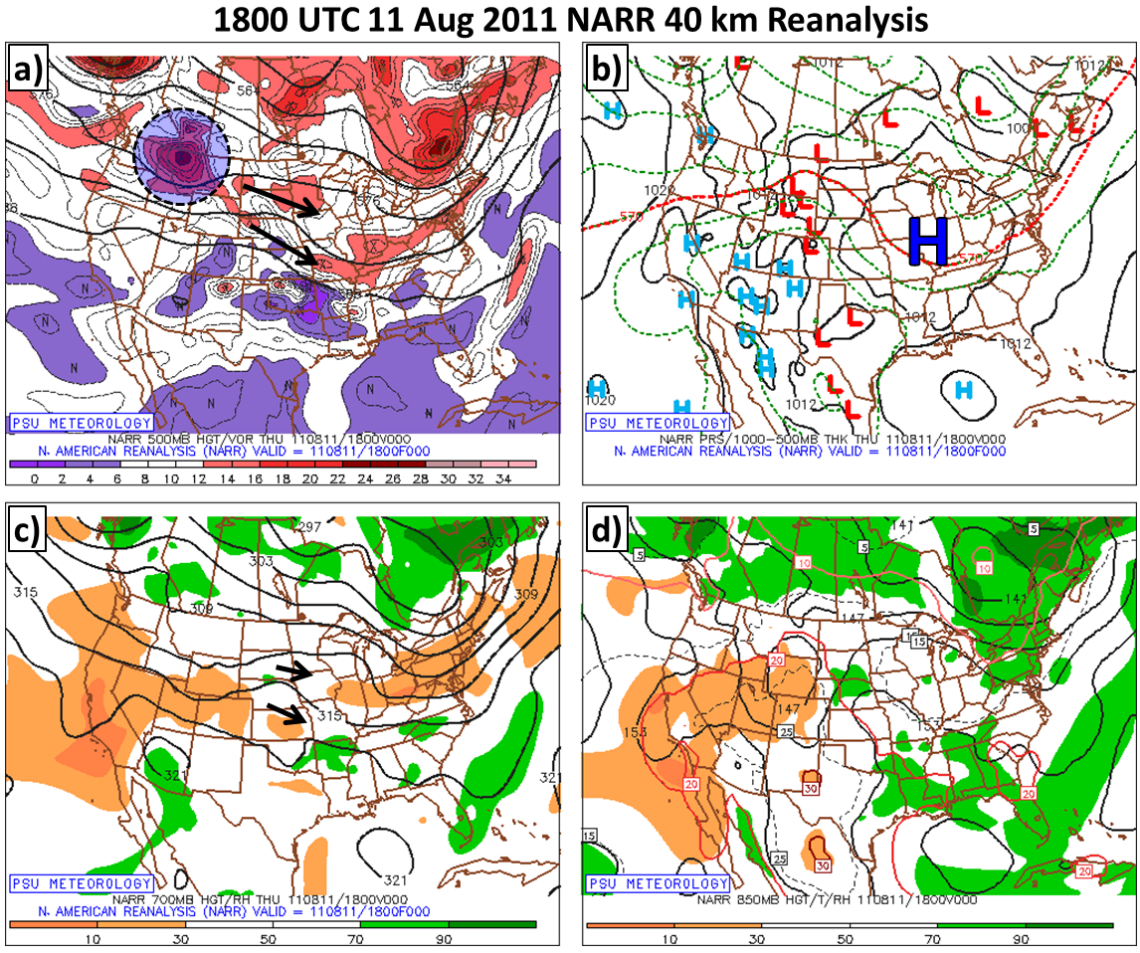

Fig. 4.4. North American Regional Reanalysis (NARR) 40-km gridded analyses valid 1800 UTC 11 Aug 2011. (a) 500-hPa geopotential height (solid) and vorticity (shaded) with arrows denoting flow pattern and dashed shaded circle denoting shortwave trough. (b) Sea-level pressure (solid black) and 1000-500-hPa thickness (dashed) with annotated pressure locations. (c) 700-hPa geopotential height (solid) and relative humidity (shaded) with arrows showing flow direction. (d) 850-hPa geopotential height (solid), relative humidity (shaded), and temperature (dashed). Image courtesy of Pennsylvania State University's e-WALL web-based system.

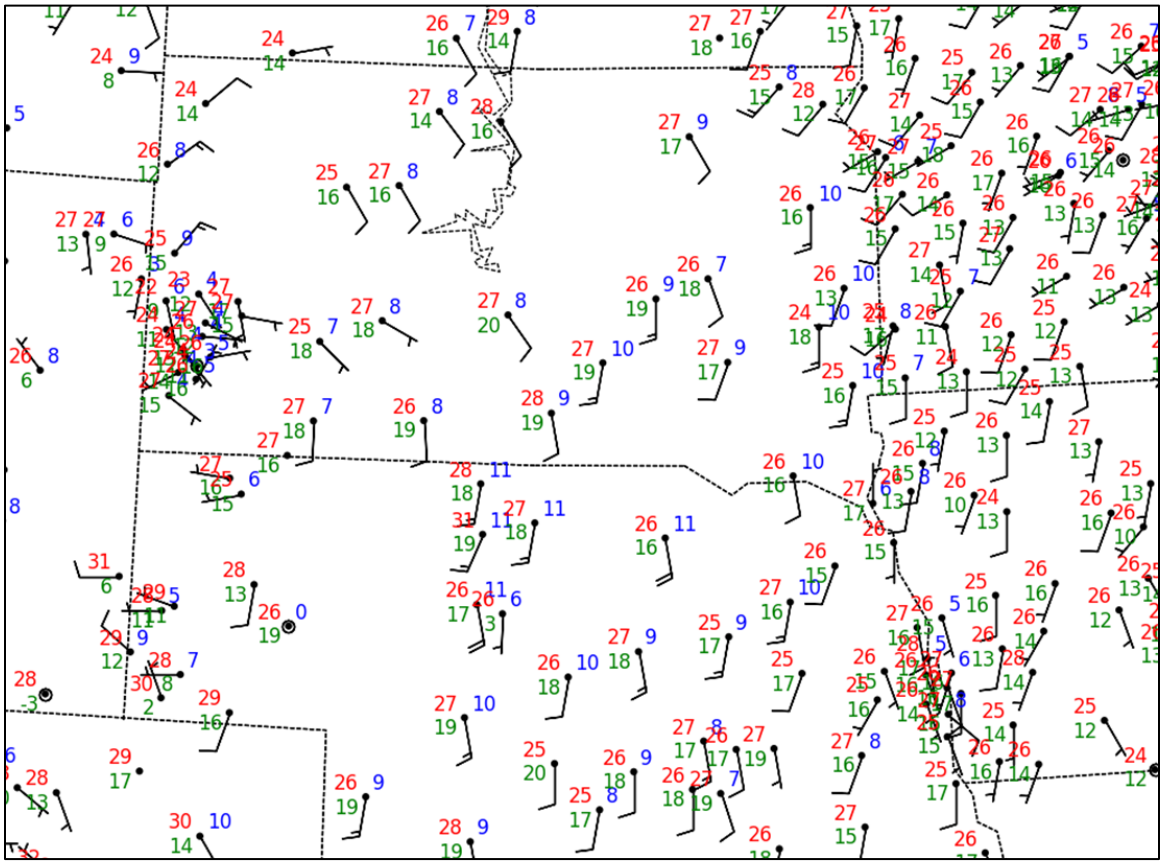

Fig. 4.5. NWS ASOS/AWOS and BLM RAWS surface observations valid 1800 UTC 11 Aug 2011 over South Dakota and Nebraska. Station plots depict surface temperature (C, red), dewpoint (C, green), wind barbs (full barb 5 m s^{-1}), and peak wind gust (m s^{-1}, blue) recorded within an hour of the valid time.

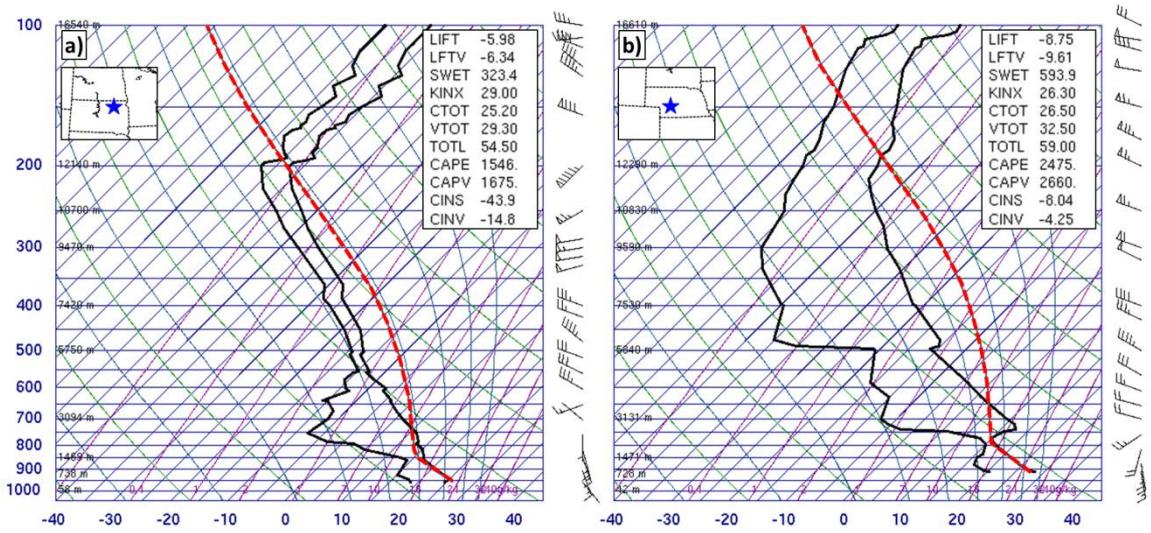

Fig. 4.6. Skew-T, log-p diagrams from (a) Aberdeen, South Dakota and (b) North Platte, Nebraska valid 0000 UTC 12 Aug 2011. Solid black lines denote temperature and dewpoint sounding profiles with observed winds provided to the right of the plot (full barb 5 knots ~ 2.6 m s^{-1}). Hypothetical surface parcel trajectory annotated as red dashed line with subset list of derived indices given in top right text box. Sounding geographic location shown with blue star on inset geographic map. Sounding images courtesy University of Wyoming Upper Air Sounding Analysis web products.

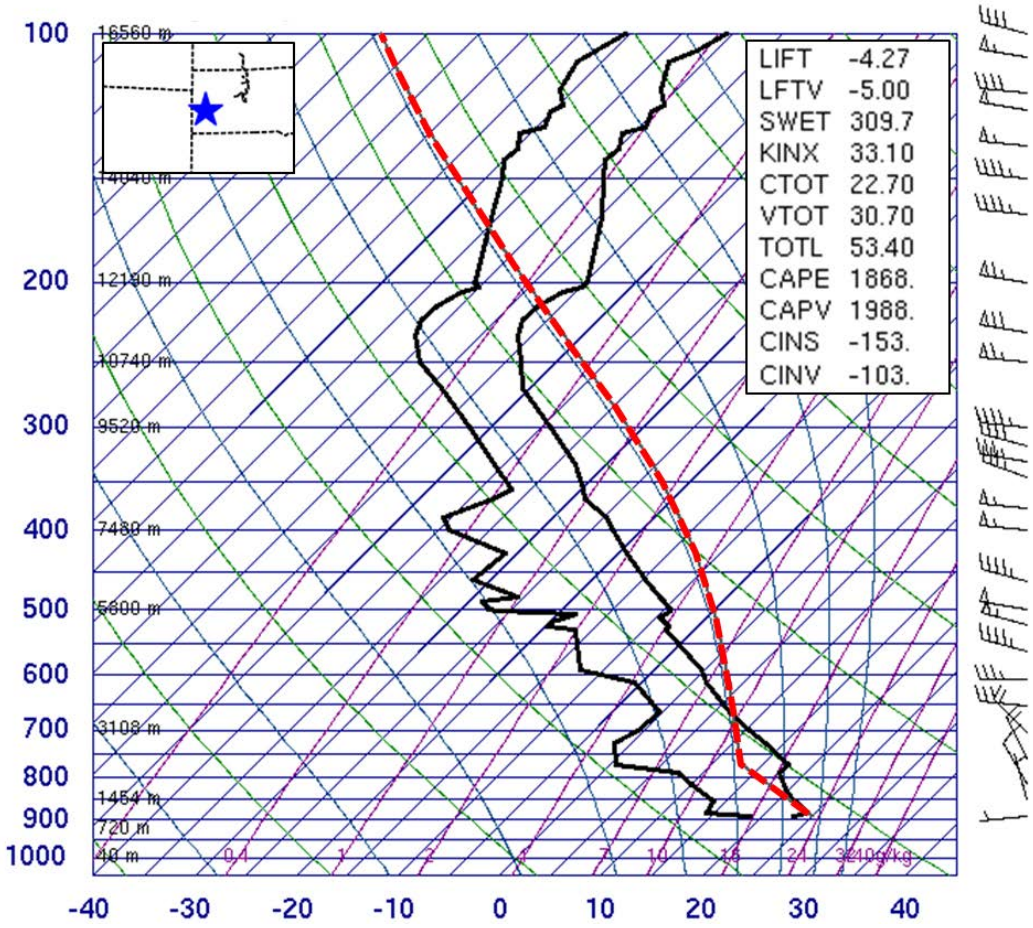

Fig. 4.7. As in Figure 4.6 except for Rapid City, South Dakota valid 0000 UTC 12 Aug 2011.

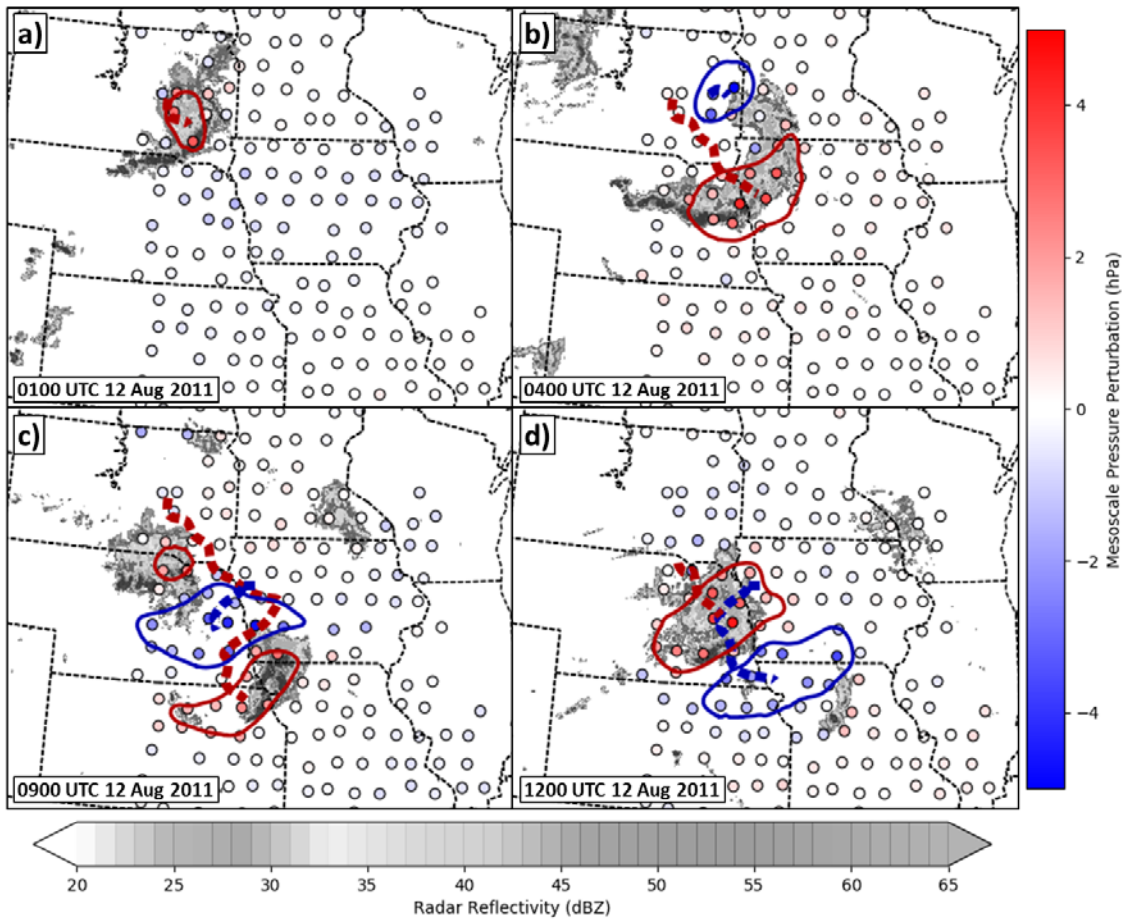

Fig. 4.8. Mesoscale feature identification analyses valid (a) 0100, (b) 0400, (c) 0900, (d) 1200 12 Aug 2011 over the north-central CONUS. Base radar reflectivity larger than 20 dBZ given in grayscale coloring. Detected perturbation features shown as dark red (blue) contours for positive (negative) perturbations, with feature tracks shown as dashed dark red (blue) lines. TA locations plotted as circle markers with red (blue) coloring denoting magnitude of positive (negative) mesoscale perturbation recorded.

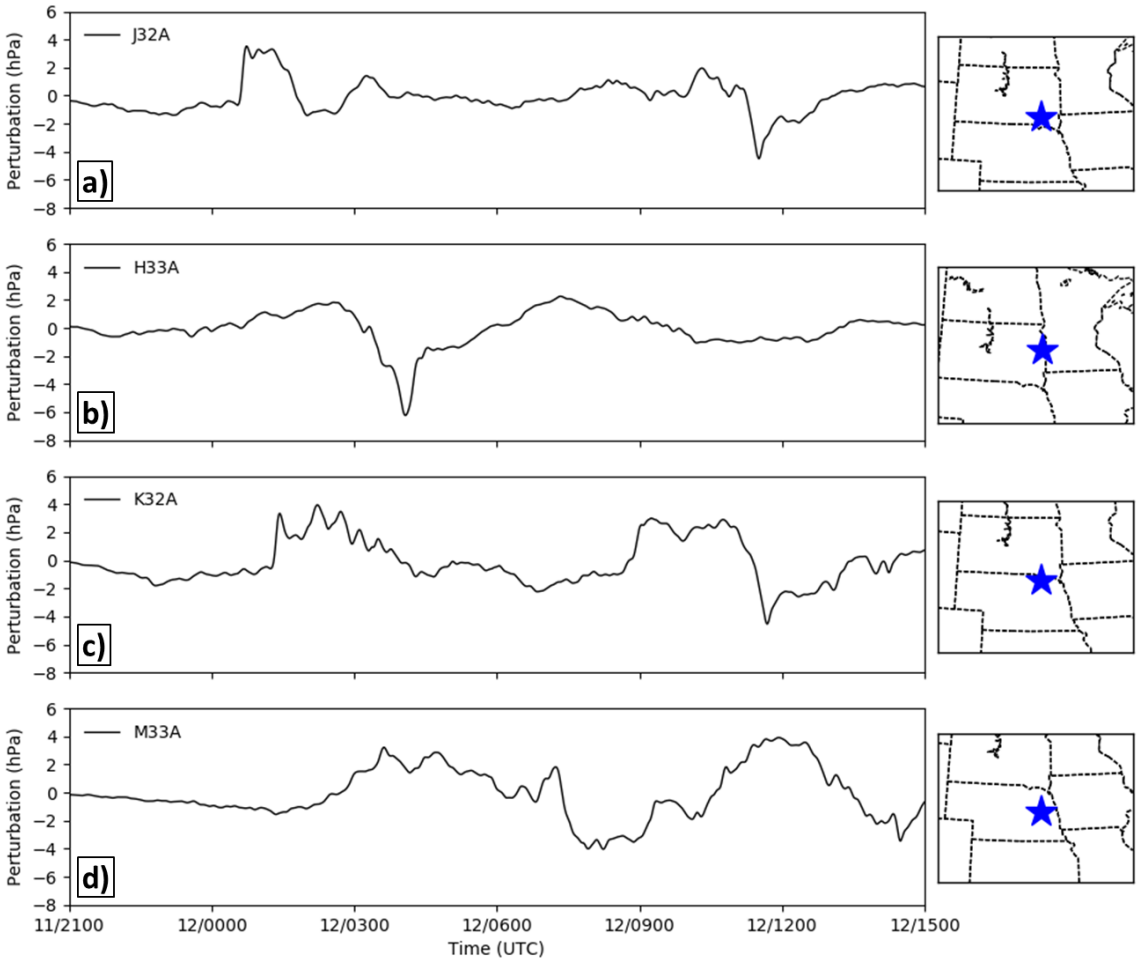

Fig. 4.9. Band-pass filtered (10 min – 12h) mesoscale pressure perturbation time series valid 2100 UTC 11 Aug 2011 – 1500 UTC 12 Aug 2011 at TA stations (a) J32A, (b) H33A, (c) K32A, and (d) M33A. Location of stations shown as blue stars on geographic maps to the right of the time series.

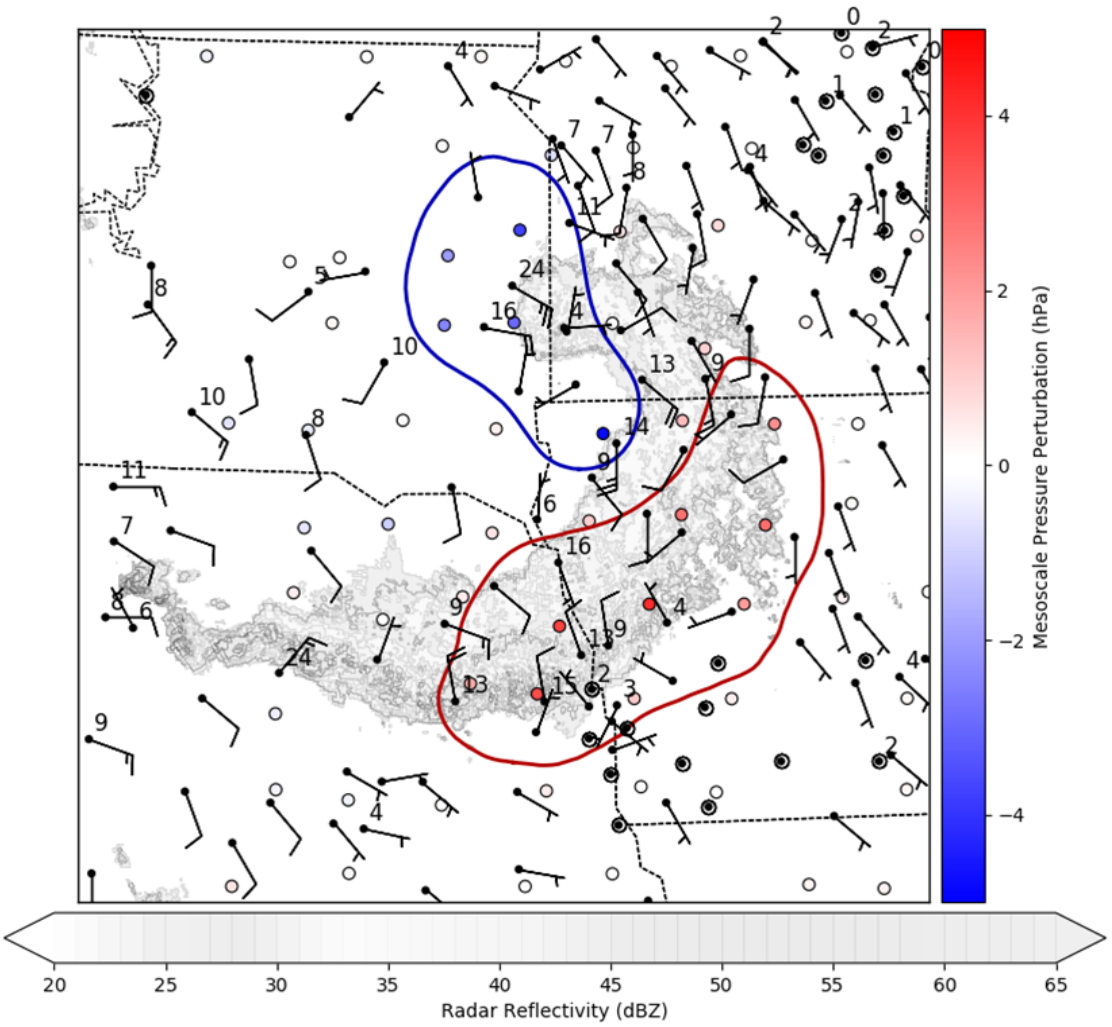

Fig. 4.10. Detected positive (negative) mesoscale features in red (blue), radar imagery (faded grayscale), TA mesoscale pressure perturbations (colored circle markers), and NWS ASOS/AWOS and BLM RAWS surface winds (barbs, full barb 5 m s^{-1}) valid 0415 UTC 12 Aug 2011 over intersection of Nebraska, Iowa, and South Dakota. Surface station peak wind gusts provided in black text if recorded (m s^{-1}).

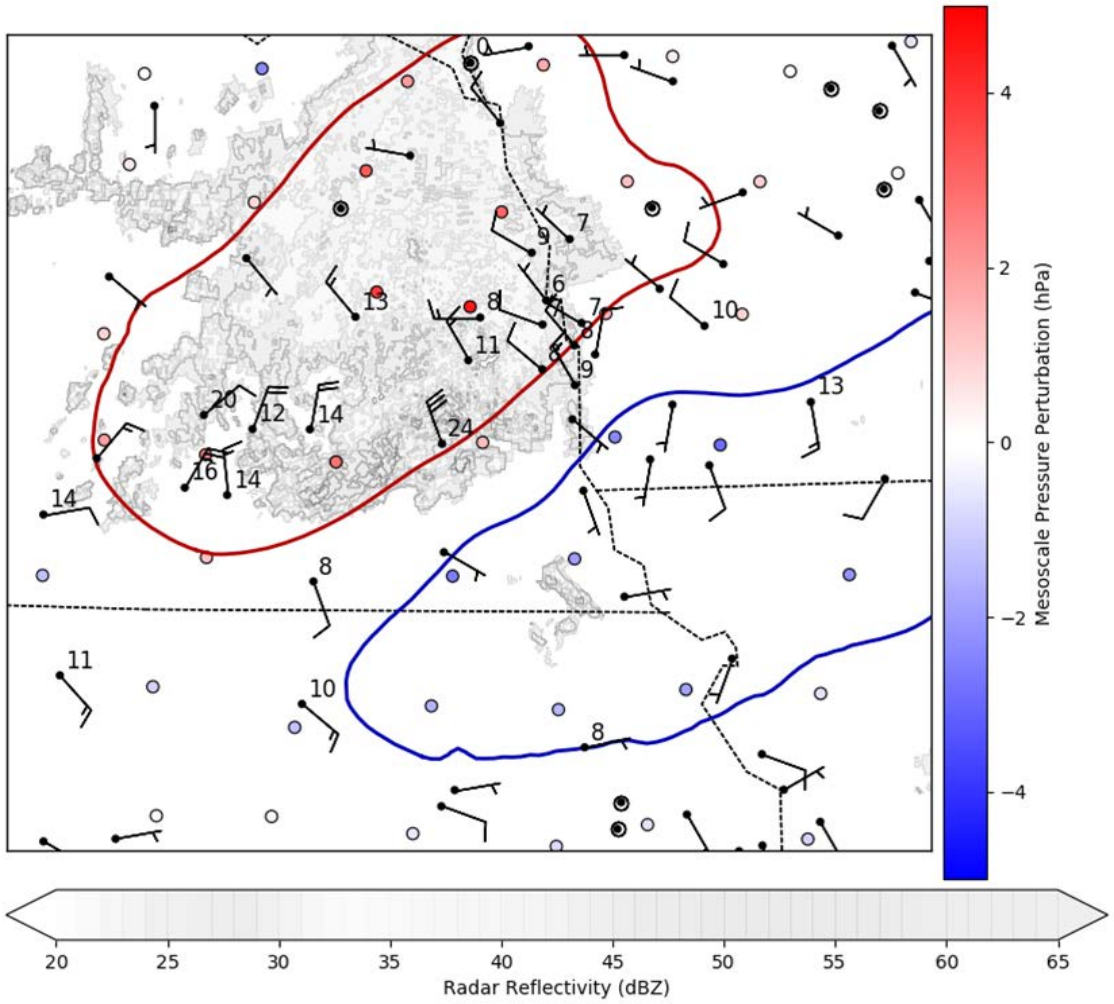

Fig. 4.11. As in Figure 4.10, except at 1200 UTC 11 Aug 2011 over southeast Nebraska and southwest Iowa.

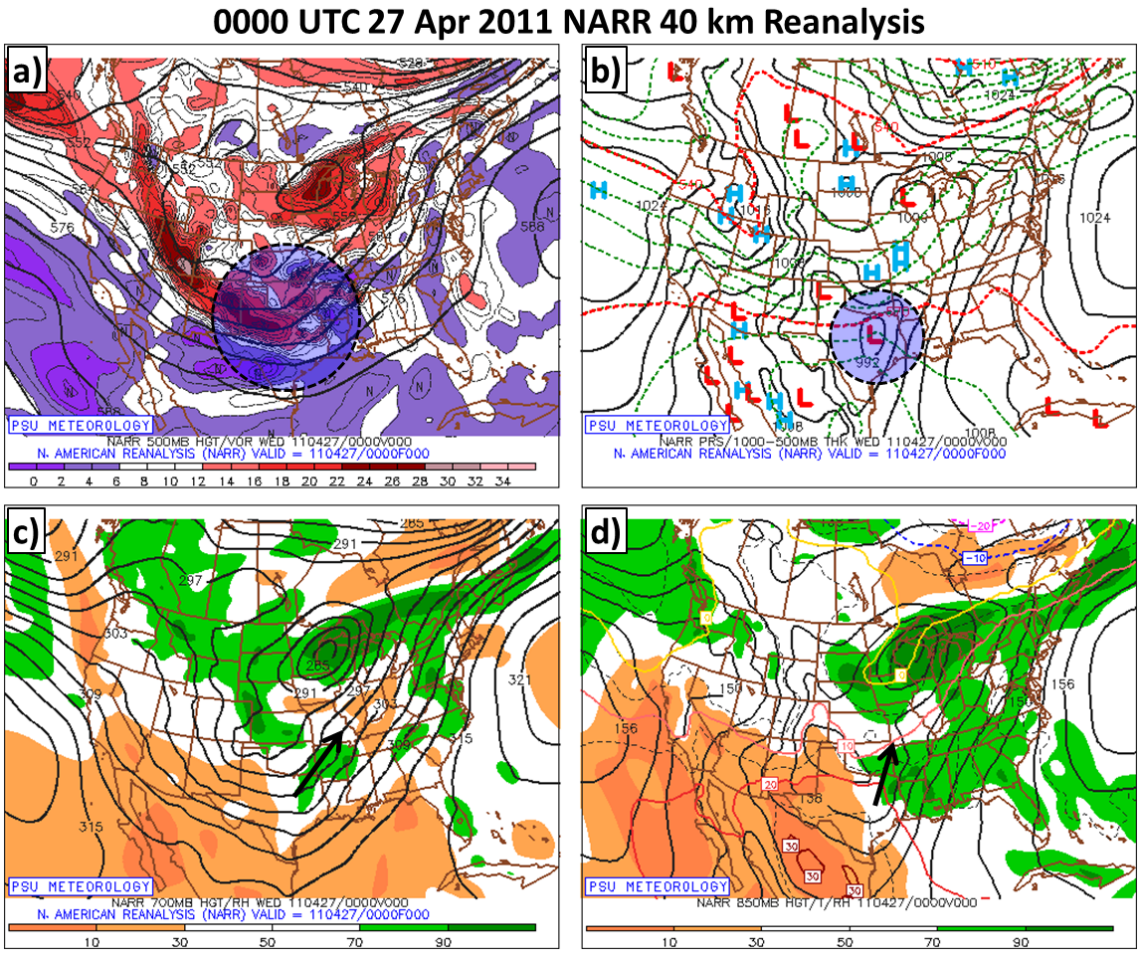

Fig. 4.12. As in Figure 4.4, except at 0000 UTC 27 Apr 2011. Region of prominent cyclonic vorticity advection annotated in (a). Surface cyclone development annotated in (b). General 700 and 850 hPa flow patterns annotated in (c) and (d), respectively.

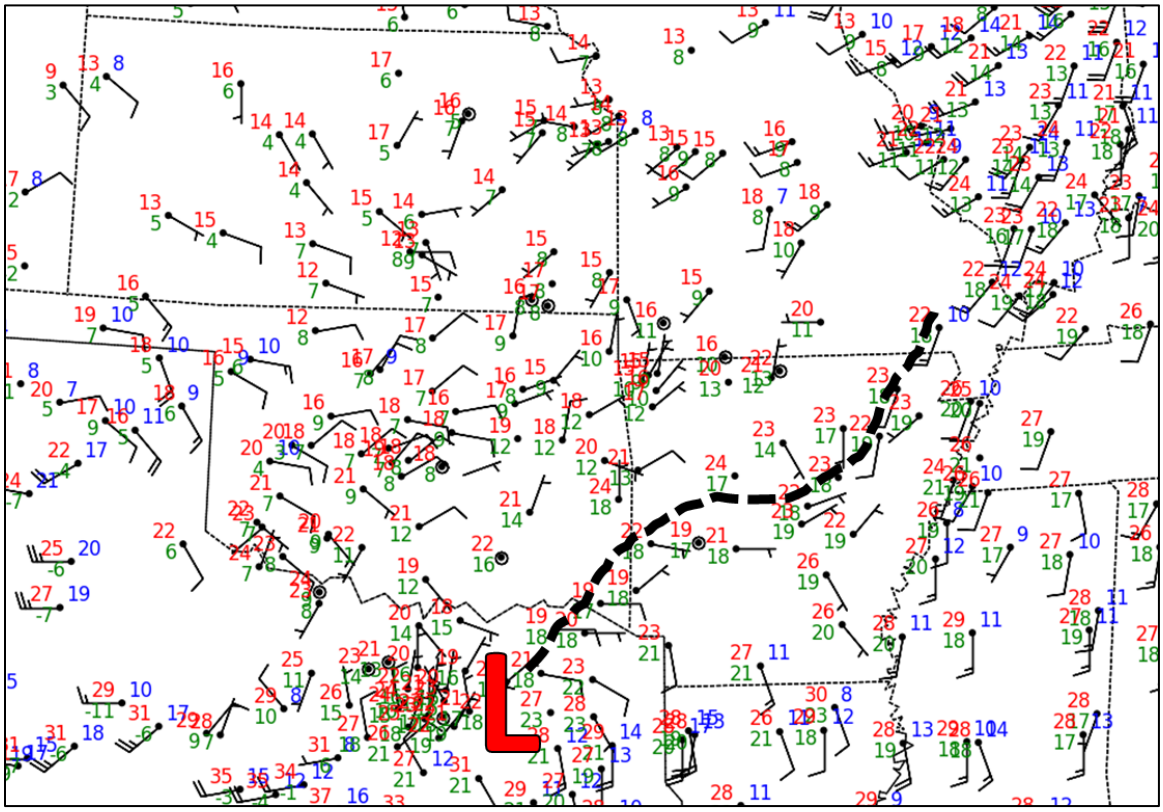

Fig. 4.13. As in Figure 4.5, except at 2100 UTC 26 Apr 2011 centered over south-central CONUS. Surface low pressure and baroclinic boundary extending northeast annotated as red ‘L’ and dashed line, respectively.

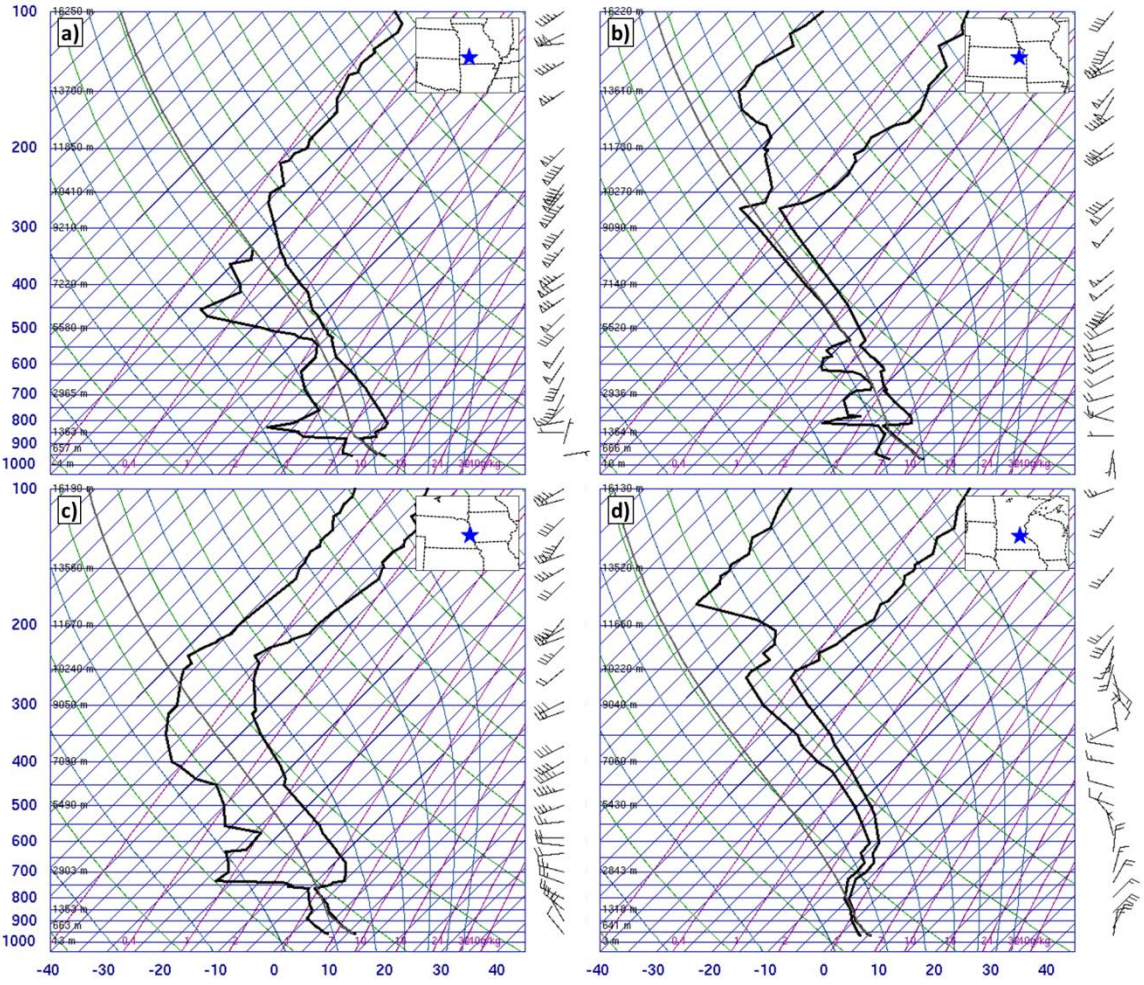

Fig. 4.14. Skew-T, log-p diagrams from (a) Springfield, Missouri, (b) Topeka, Kansas, (c) Omaha, Nebraska, and (d) Chanhassen, Minnesota valid 0000 UTC 27 Apr 2011. Solid black lines denote temperature and dewpoint sounding profiles with observed winds provided to the right of the plot (full barb 5 knots ~ 2.6 m s^{-1}). Sounding geographic location shown with blue star on inset geographic map. Sounding images courtesy University of Wyoming Upper Air Sounding Analysis web products.

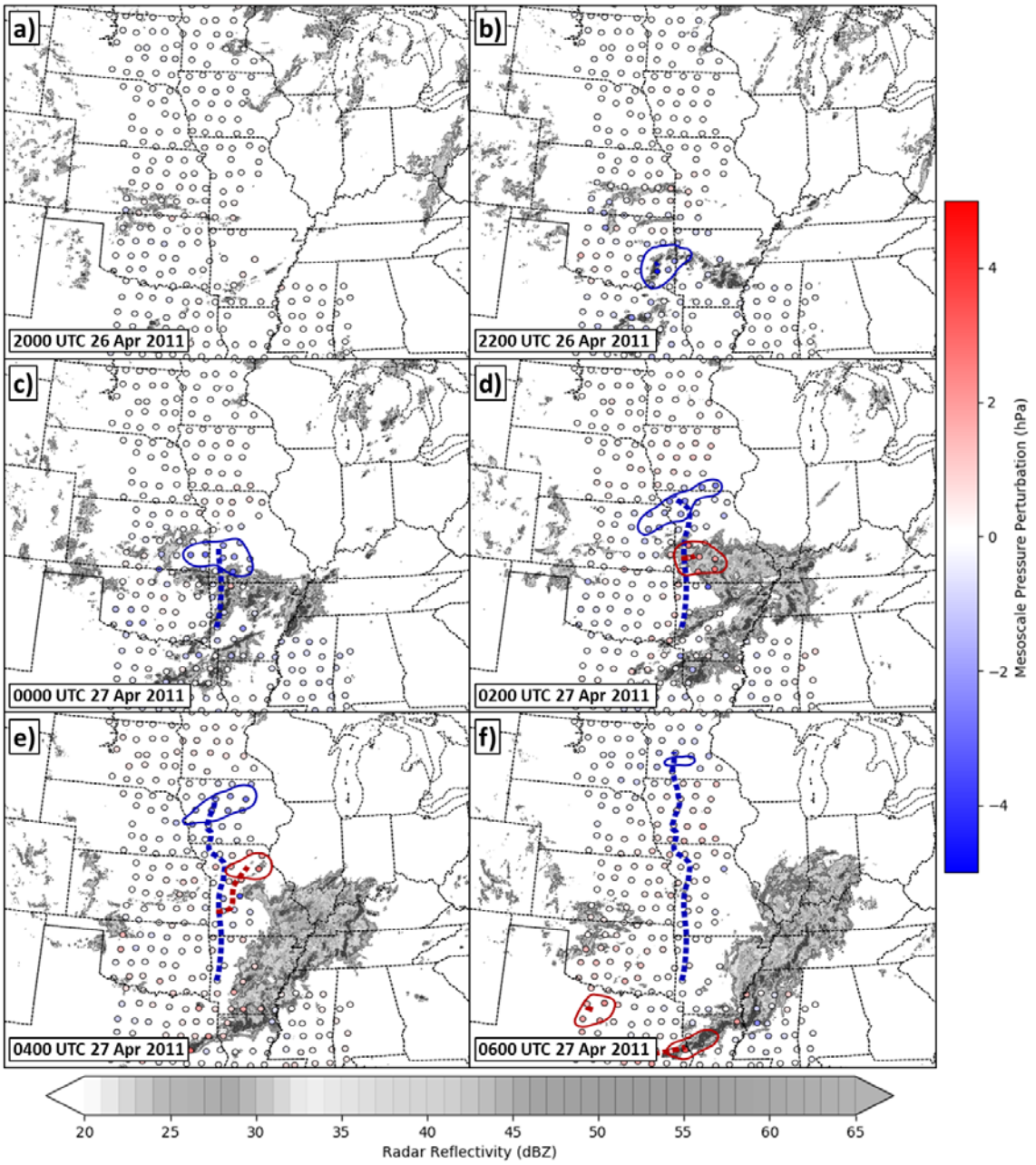

Fig. 4.15. As in Figure 4.8, except at (a) 2000 UTC 26 Apr 2011, (b) 2200 UTC, (c) 0000 UTC 27 Apr 2011, (d) 0200 UTC, (e) 0400 UTC, and (f) 0600 UTC across the central CONUS.

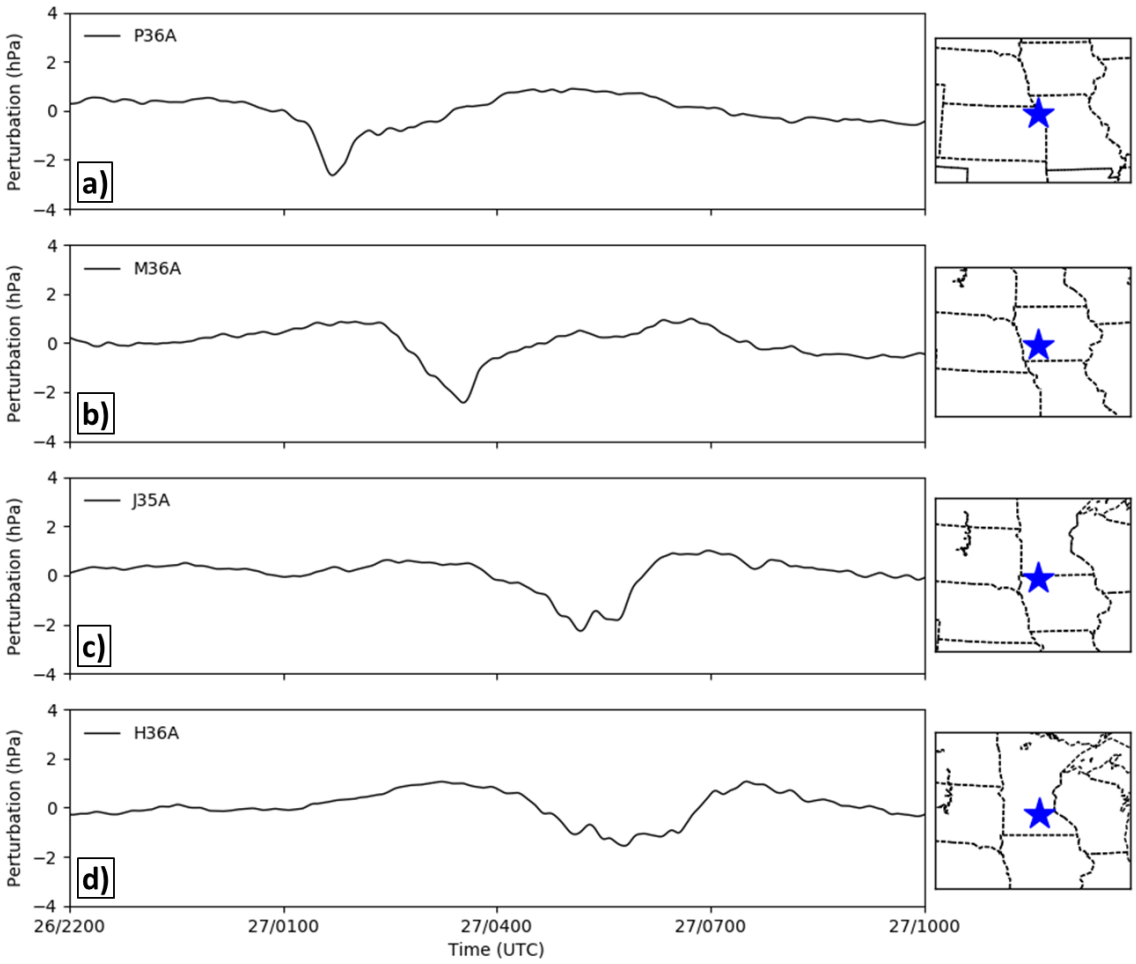

Fig. 4.16. As in Figure 4.9, except valid 2200 UTC 26 Apr 2011 – 1000 UTC 27 Apr 2011 at TA stations (a) P36A, (b) M36A, (c) J35A, and (d) H36A.

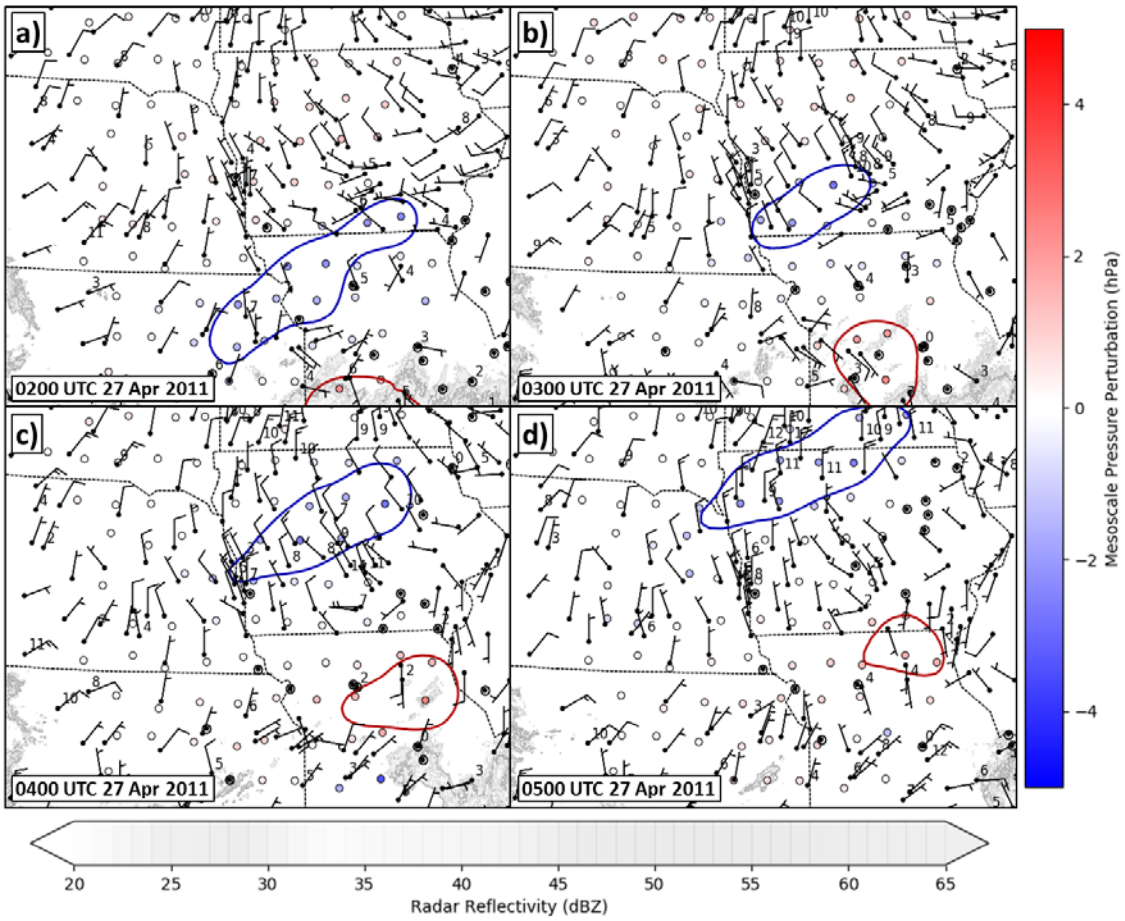

Fig. 4.17. As in Figure 4.10, except at (a) 0200 UTC, (b) 0300 UTC, (c) 0400 UTC, and (d) 0500 UTC 27 Apr 2011 centered at intersection of Nebraska, Iowa, and Missouri.

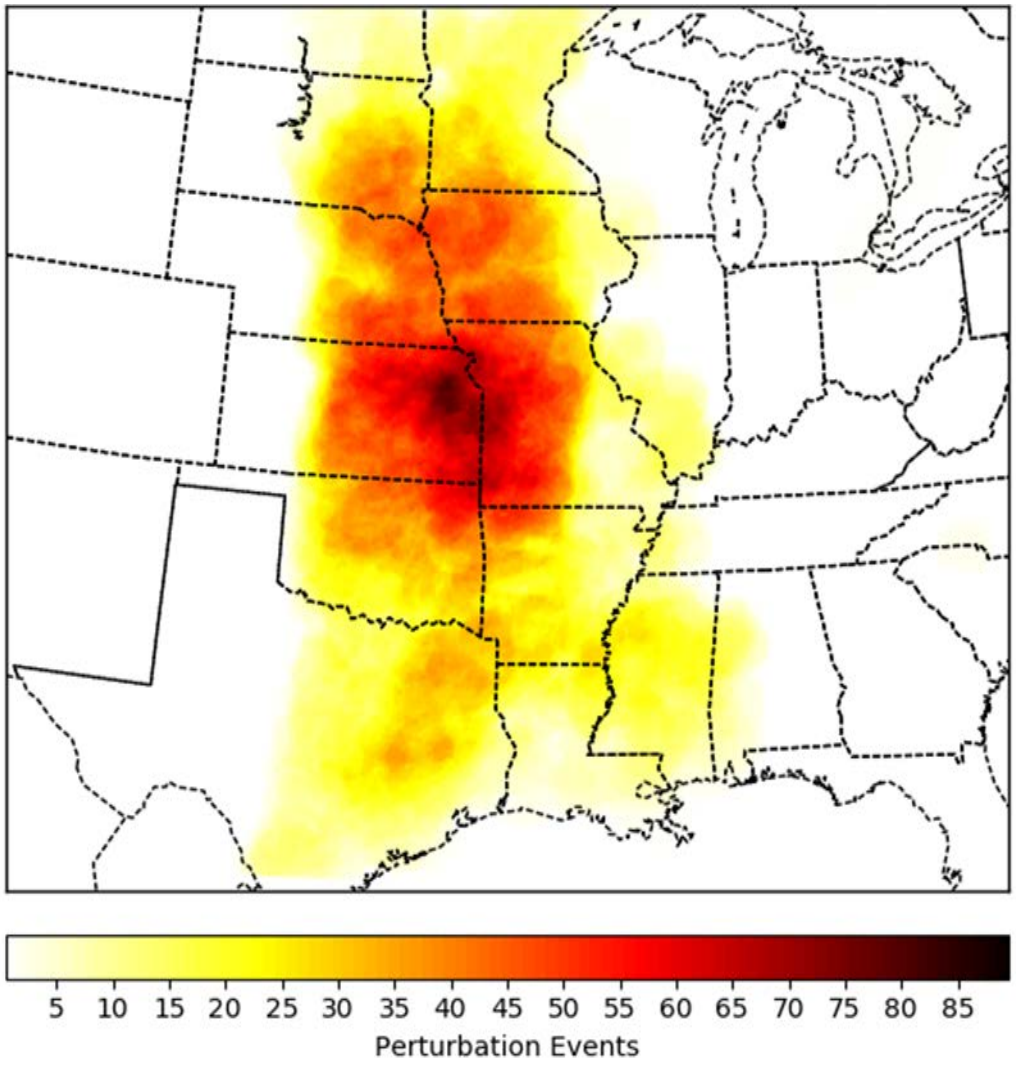

Fig. 4.18. Mesoscale pressure perturbation feature occurrences as a function of location for 1 Mar – 31 Aug 2011 across the TA domain. Values are expressed as number of unique features transecting across a 5-km horizontal grid cell for the region encompassed by the TA (see Figure 4.1).

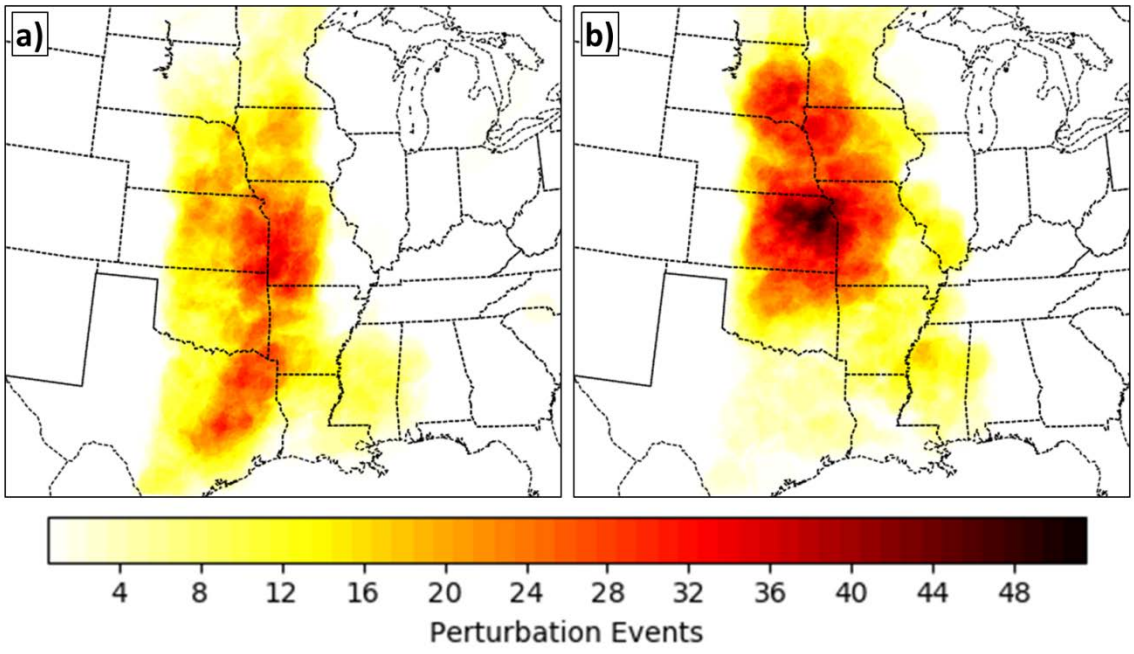

Fig. 4.19. As in Figure 4.18, except for features during the (a) spring (MAM) and (b) summer (JJA) seasons.

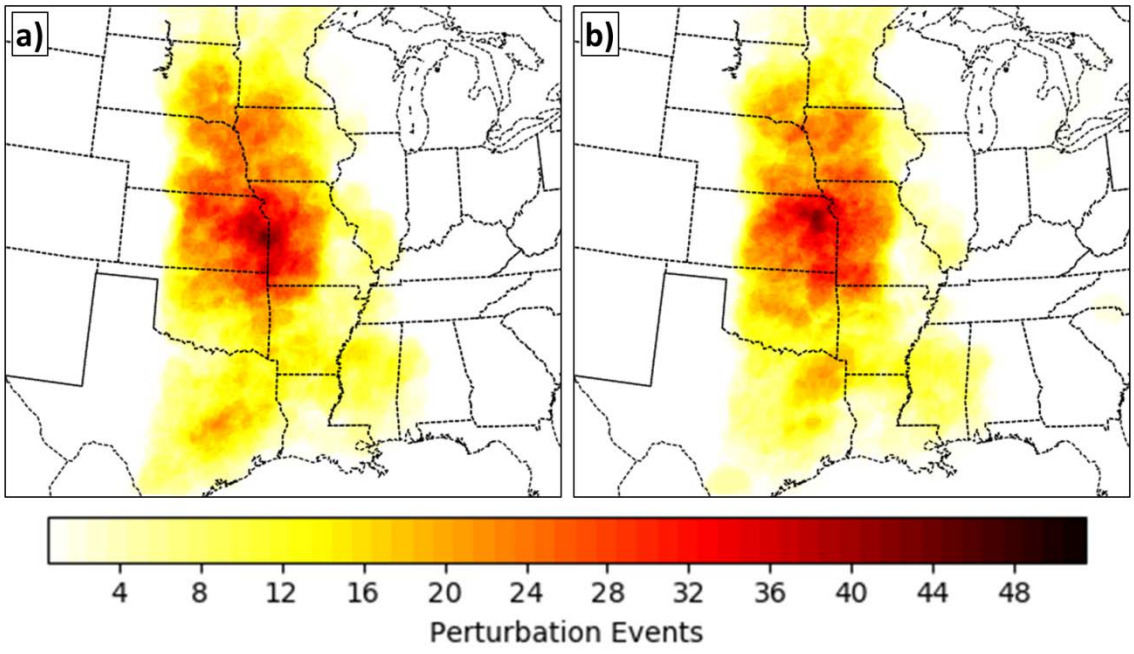

Fig. 4.20. As in Figure 4.18, except for features associated with (a) positive and (b) negative pressure perturbations.

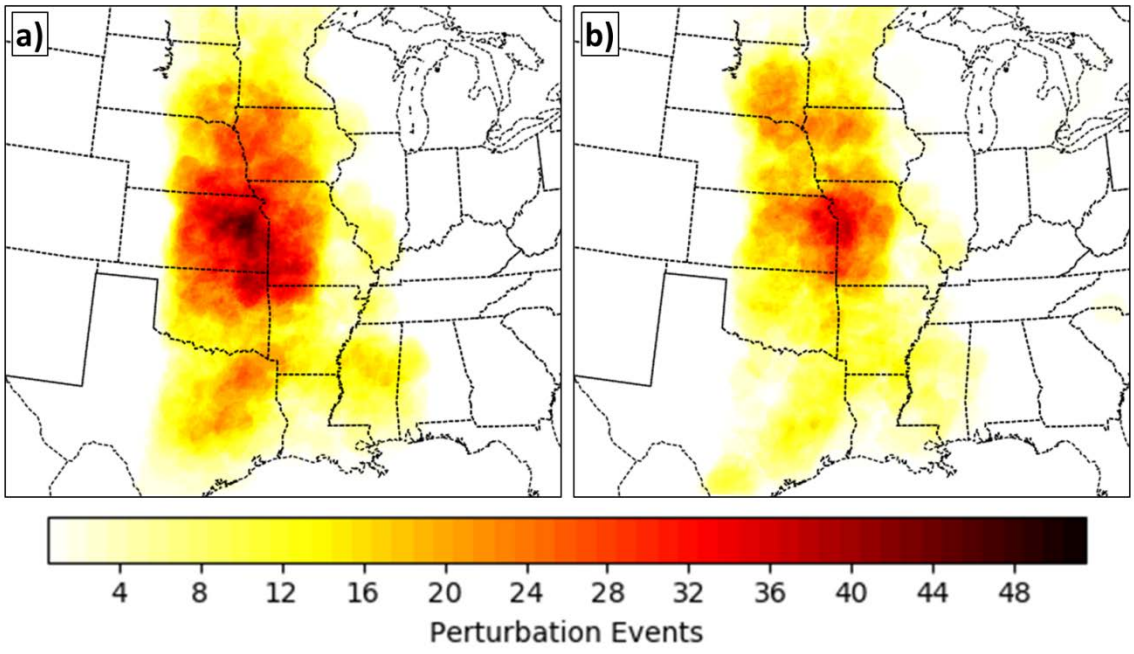

Fig. 4.21. As in Figure 4.18, except for features (a) associated with *StormData* wind reports and (b) not associated with wind reports from *StormData*.

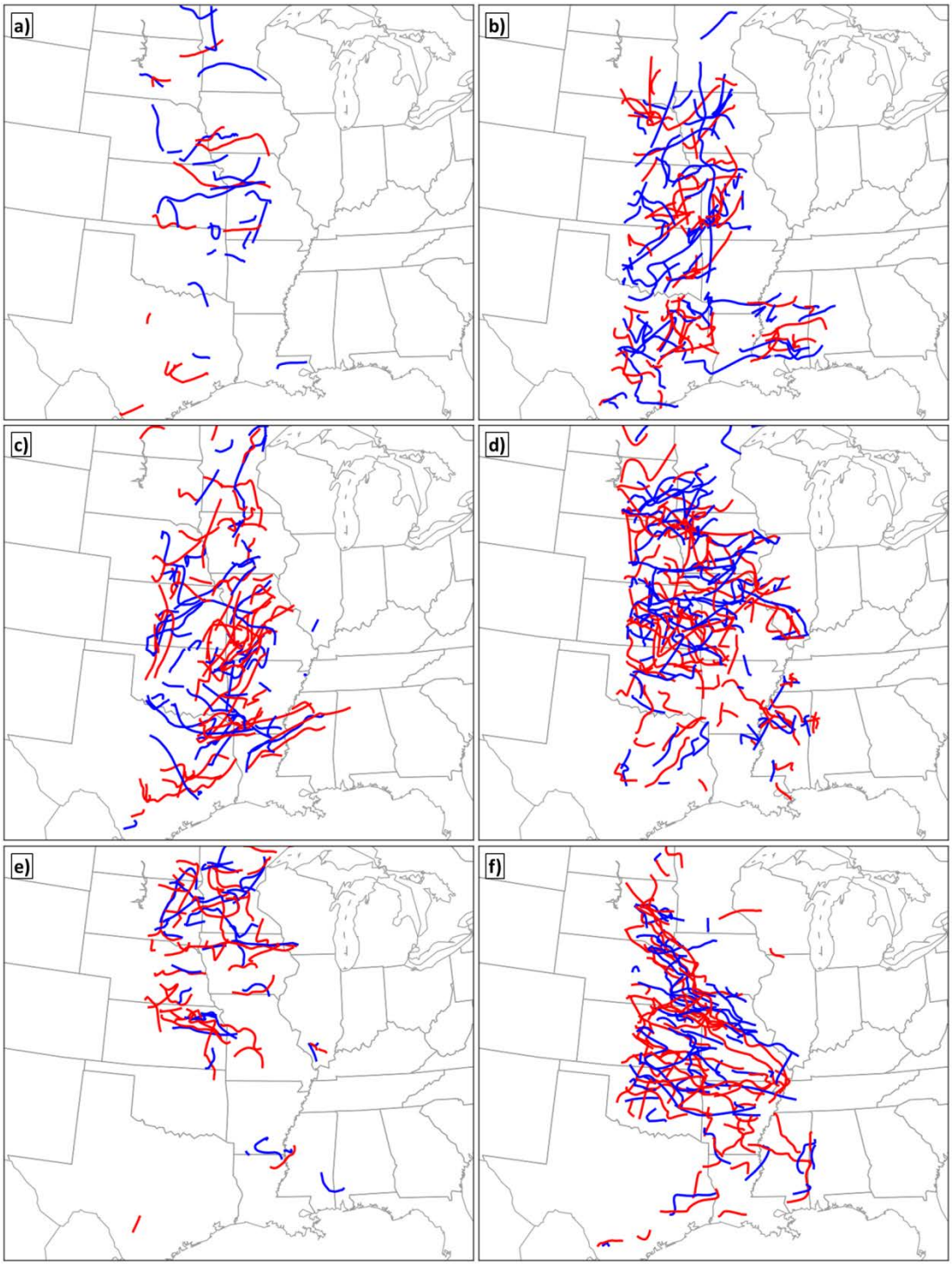

Fig. 4.22. Mesoscale feature tracks for positive (red) and negative (blue) perturbations for (a) March, (b) April, (c) May, (d) June, (e) July, and (f) August 2011.

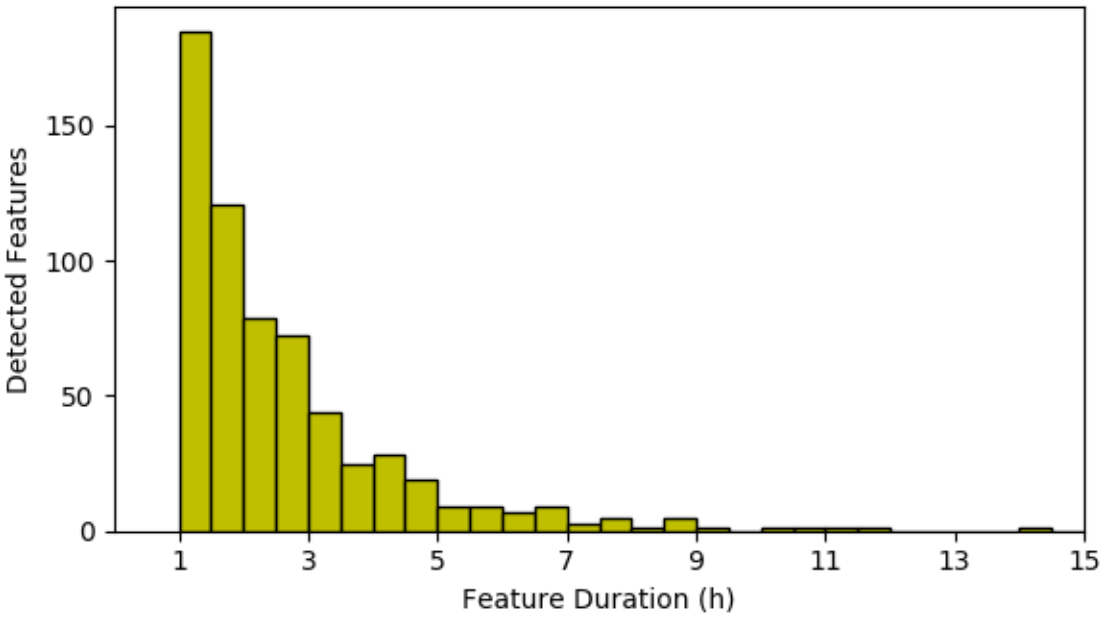

Fig. 4.23. Histogram of detected mesoscale feature occurrences by duration of feature existence (h) for the full period examined.

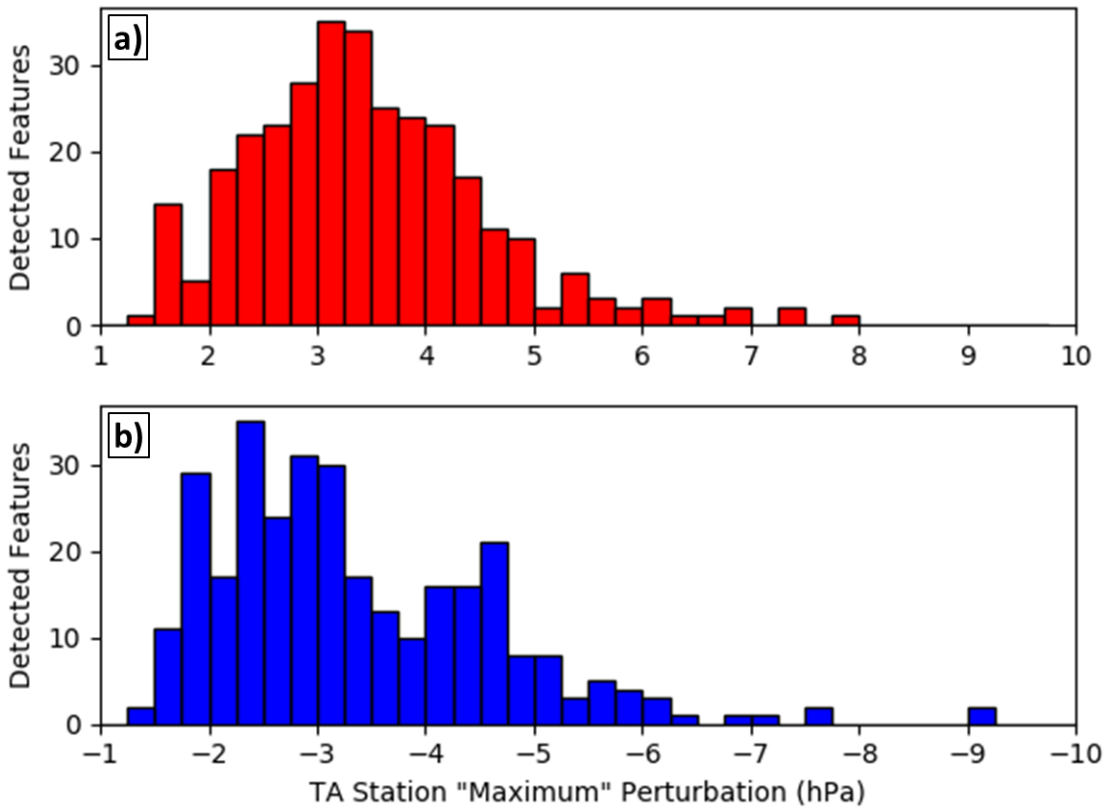

Fig. 4.24. Histograms of detected mesoscale feature occurrences by maximum magnitude reported by TA observations for (a) positive and (b) negative perturbations.

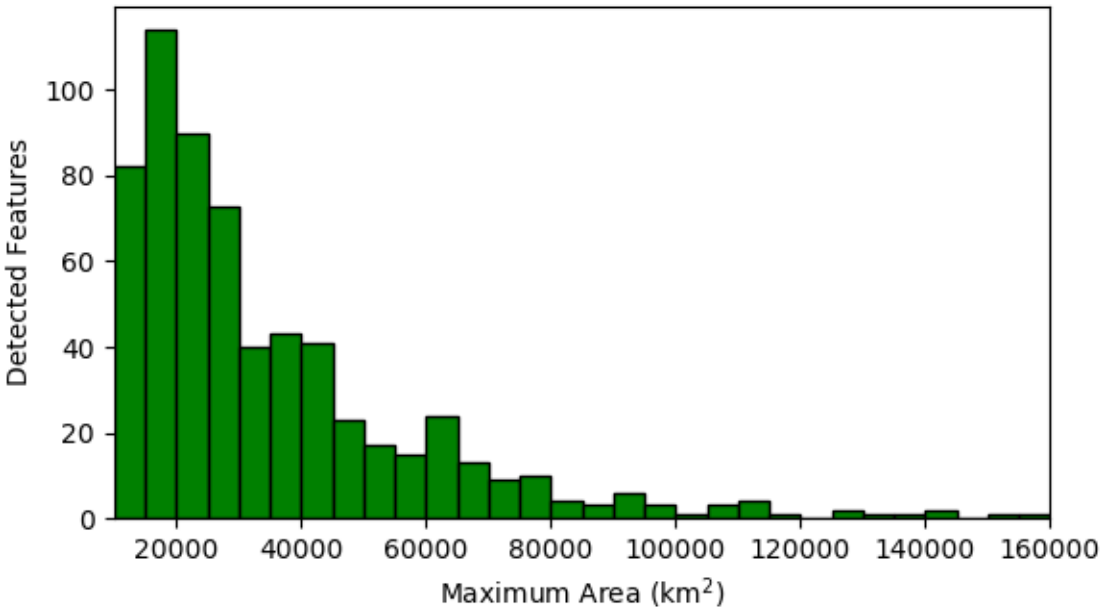

Fig. 4.25. Histograms of detected mesoscale feature occurrences by maximum 1-hPa perturbation areal extent during feature existence (km^2) for the full period examined.

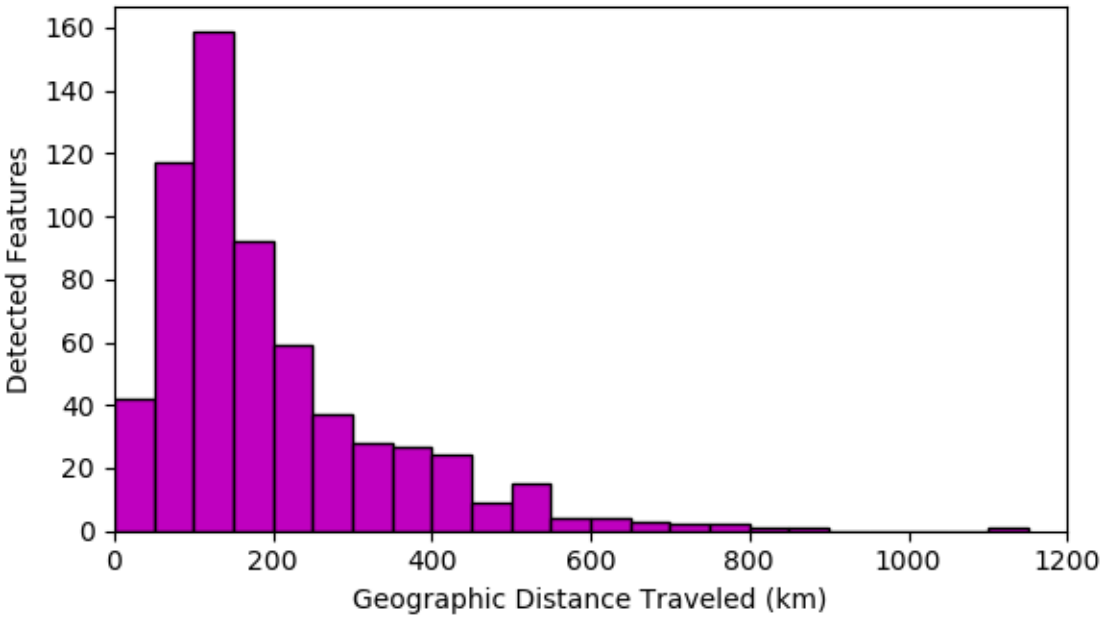

Fig. 4.26. Histograms of detected mesoscale feature occurrences by geographic distance traveled (km) for the full period examined.

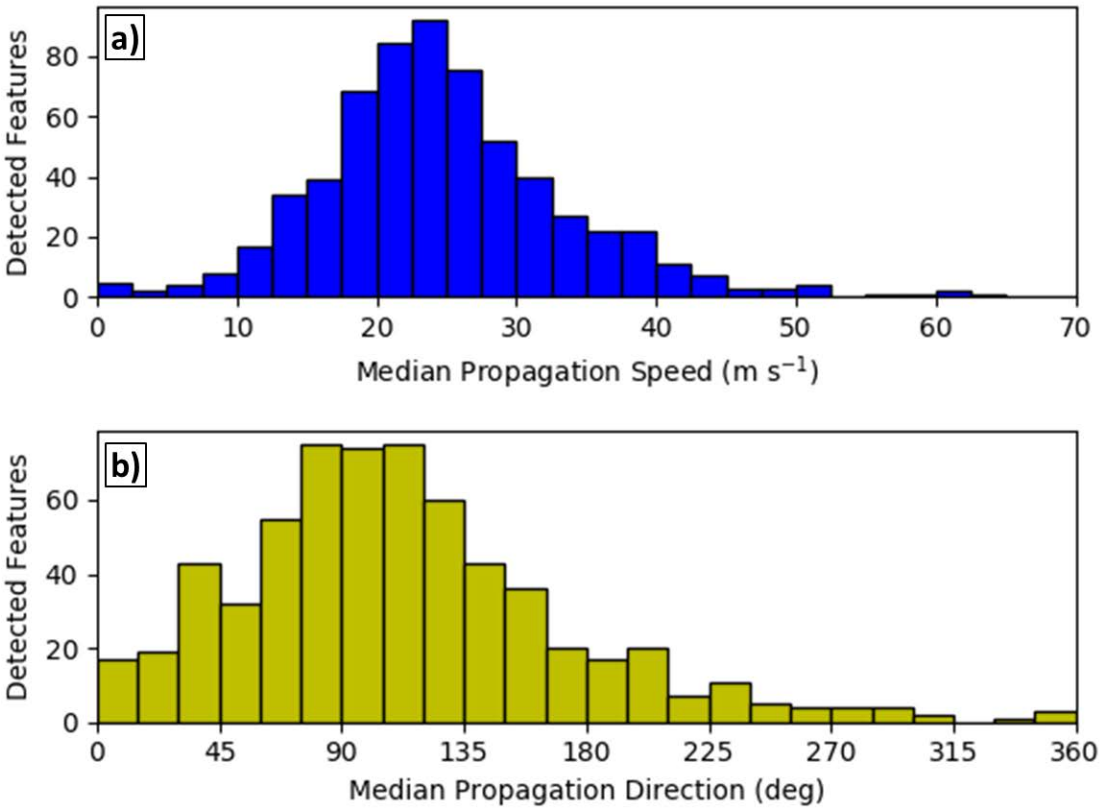

Fig. 4.27. Histograms of detected mesoscale feature occurrences by (a) median feature speed and (b) median direction.

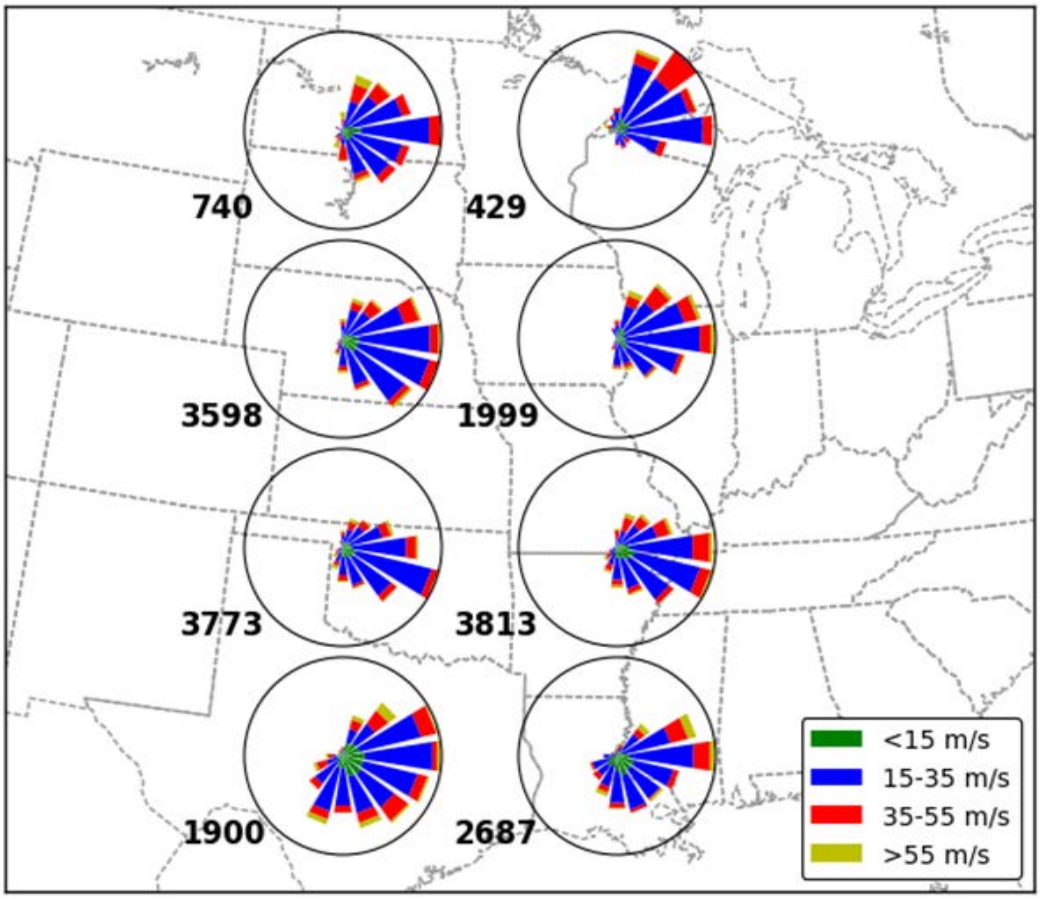

Fig. 4.28. Mesoscale feature speed and direction roses for all features detected from 1 Mar – 31 Aug 2011. Features are split into 8 geographic sectors as shown by the general rose locations, with sample counts indicating the number of assessed feature speeds and directions per bin to the lower left of each sector. Samples are composed of speeds and directions calculated at all timestamps for a specific feature's existence period.

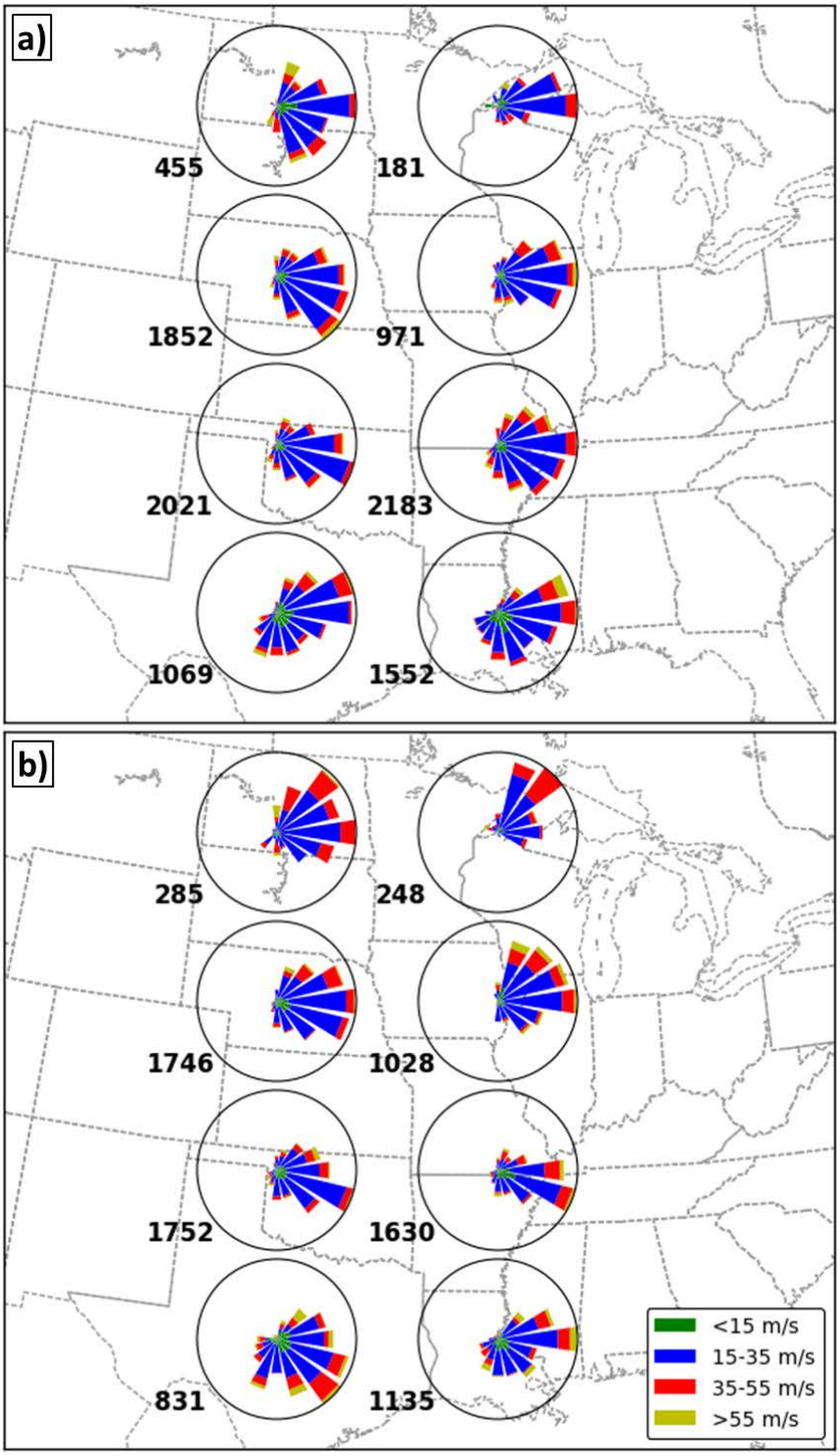

Fig. 4.29. As in Figure 4.28, except divided into (a) positive and (b) negative mesoscale pressure features.

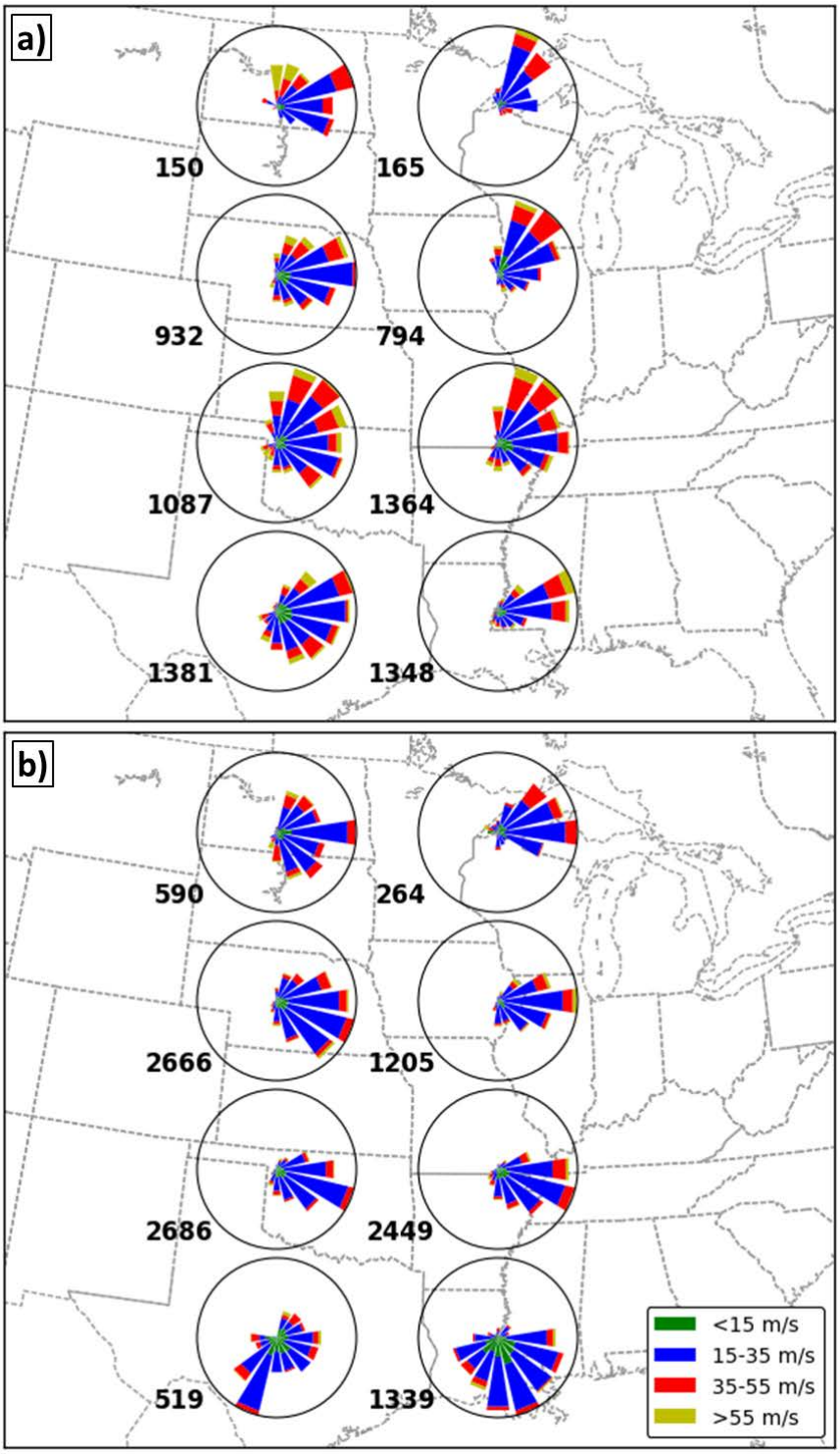

Fig. 4.30. As in Figure 4.28, except divided into (a) spring (MAM) and (b) summer (JJA) mesoscale pressure features.

4.8 References

Adams-Selin, R. D., and R. H. Johnson, 2013: Examination of gravity waves associated with the 13 March 2003 bow echo. *Mon. Wea. Rev.*, **141**, 3735-3756.

Anderson, J. L., B. Wyman, S. Zhang, and T. Hoar, 2005: Assimilation of PS observations using an ensemble filter in an idealized global atmospheric prediction system. *J. Atmos. Sci.*, **62**, 2925-2938.

Ashley, W. S., and T. L. Mote, 2005: Derecho hazards in the United States. *Bull. Amer. Meteor. Soc.*, **86**, 1577-1592.

Benjamin, S. G., J. M. Brown, G. Manikin, and G. Mann, 2007: The RTMA background-Hourly downscaling of RUC data to 5-km detail. *Preprints, 22nd Conf. on Weather Analysis and Forecasting/18th Conf. on Numerical Weather Prediction*, Park City, UT, Amer. Meteor. Soc., 4A.6. [Available online at http://ams.confex.com/ams/pdfpapers/124825.pdf.]

Bentley, M. L., T. L. Mote, and S. F. Byrd, 2000: A synoptic climatology of derecho producing mesoscale convective systems in the north-central Plains. *Int. J. Climatol.*, **20**, 1329-1349.

Bosart, L. F., and A. Seimon, 1988: A case study of an unusually intense atmospheric gravity wave. *Mon. Wea. Rev.*, **116**, 1857-1886.

——, W. E. Bracken, and A. Seimon, 1998: A study of cyclone mesoscale structure with emphasis on a large-amplitude inertia-gravity wave. *Mon. Wea. Rev.*, **126**, 1497-1527.

Bremer, P.-T., G. Weber, V. Pascucci, M. Day, and J. Bell, 2010: Analyzing and tracking burning structures in lean premixed hydrogen flames. *IEEE Trans. Vis. Comp. Graph.*, 16, 248-260.

Brown, R. A., and V. T. Wood, 2012: The Tornadic Vortex Signature: an update. *Wea. Forecasting*, **27**, 525-530.

Bullock, R., 2011: Development and implementation of MODE time domain object-based verification. Preprints, *24th Conf. on Weather and Forecasting/20th Conf. on Numerical Weather Prediction*, Seattle, WA, Amer. Meteor. Soc., 96. [Available online at https://ams.confex.com/ams/91Annual/webprogram/Paper182677.html.]

Clark, A. J., R. G. Bullock, T. L. Jensen, M. Xue, and F. Kong, 2014: Application of object-based time-domain diagnostics for tracking precipitation systems in convection-allowing models. *Wea. Forecasting*, **29**, 517-542.

Coleman, T. A., and K. R. Knupp, 2009: Factors affecting surface wind speeds in gravity waves and wake lows. *Wea. Forecasting*, **24**, 1664-1679.

Compo, G. P., J. S. Whitaker, P. D. Sardeshmukh, 2006: Feasibility of a 100-year reanalysis using only surface pressure data. *Bull. Amer. Meteor. Soc.*, **87**, 175-190.

Compo, G. P., and Coauthors, 2011: The Twentieth Century Reanalysis Project. *Quart. J. Roy. Meteor. Soc.*, **137**, 1-28.

Coniglio, M. C., D. J. Stensrud, and M. B. Richman, 2004: An observational study of derecho-producing convective systems. *Wea. Forecasting*, **19**, 320-337.

—, S. F. Corfidi, and J. S. Kain, 2011: Environment and early evolution of the 8 May 2009 Derecho-producing convective system. *Mon. Wea. Rev.*, **139**, 1083-1102.

Crook, N. A., 1988: Trapping of low-level internal gravity waves. *J. Atmos. Sci.*, **45**, 1533-1541.

Davis, C. A., B. Brown, and R. Bullock, 2006: Object-based verification of precipitation forecasts. Part I: Methodology and application to mesoscale rain areas. *Mon. Wea. Rev.*, **134**, 1772-1784.

—, —, —, and J. Halley-Gotway, 2009: The Method for Object-Based Diagnostic Evaluation (MODE) applied to numerical forecasts from the 2005 NSSL/SPC Spring Program. *Wea. Forecasting*, **24**, 1252-1267.

de Groot-Hedlin, C. D., M. A. H. Hedlin, K. Walker, D. P. Drob, and M. Zumberge, 2008: Study of propagation from the shuttle Atlantis using a large seismic network. *J. Acoustic Soc. Amer.*, **124**, 1442-1451.

de Groot-Hedlin, C. D., M. A. H. Hedlin, and K. T. Walker, 2014: Detection of gravity waves across the USArray: A case study. *Earth Planet. Sci. Lett.*, **402**, 346-352.

de Pondeca, M., and Coauthors, 2011: The Real-Time Mesoscale Analysis at NOAA's National Centers for Environmental Prediction: Current status and development. *Wea. Forecasting*, **26**, 593-612.

Engerer, N. A., D. J. Stensrud, and M. C. Coniglio, 2008: Surface characteristics of observed cold pools. *Mon. Wea. Rev.*, **136**, 4839-4849.

Evans, J. S., and C. A. Doswell III, 2001: Examination of derecho environments using proximity soundings. *Wea. Forecasting*, **16**, 329-342.

Gaberšek, S., and D. R. Durran, 2006: Gap flows through idealized topography. Part II: Effects of rotation and surface friction. *J. Atmos. Sci.*, **63**, 2720-2739.

Geerts, B., Q. Miao, and J. C. Demko, 2008: Pressure perturbations and upslope flow over a heated, isolated mountain. *Mon. Wea. Rev.*, **136**, 4272-4288.

Grivet-Talocia, S., and F. Einaudi, 1998: Wavelet analysis of a microbarograph network. *IEEE Trans. Geosci. Remote Sens.*, **36,** 418-433.

—, —, W. L. Clark, R. D. Dennett, G. D. Nastrom, and T. E. VanZandt, 1999: A 4-yr climatology of pressure disturbances using a barometer network in central Illinois. *Mon. Wea. Rev.*, **127**, 1613-1629.

Guastini, C. T., and L. F. Bosart, 2016: Analysis of a Progressive Derecho Climatology and Associated Formation Environments. *Mon. Wea. Rev.*, **144**, 1363-1382.

Hedlin, M. A. H., D. Drob, K. Walker, and C. D. de Groot-Hedlin, 2010: A study of acoustic propagation from a large bolide in the atmosphere with a dense seismic network. *J. Geophys. Res.*, **115**, B11312.

Hedlin, M. A. H., C. D. de Groot-Hedlin, and D. P. Drob, 2012: A study of infrasound propagation using dense seismic network recordings of surface explosions. *Bull. Seismological Soc. of Amer.*, **102**, 1927-1937.

Hodges, K. I., 1994: A general method for tracking analysis and its application to meteorological data. *Mon. Wea. Rev.*, **122**, 2573-2586.

—, B. J. Hoskins, J. Boyle, and C. Thorncroft, 2003: A comparison of recent reanalysis datasets using objective feature tracking: storm tracks and tropical easterly waves. *Mon. Wea. Rev.*, **131**, 2012-2037.

Horel, J., and Coauthors, 2002: Mesowest: Cooperative mesonets in the western United States. *Bull. Amer. Meteor. Soc.*, **83**, 211-225.

Hoskins, B. J., and K. I. Hodges, 2002: New perspectives on the Northern Hemisphere winter storm tracks. *J. Atmos. Sci.*, **59**, 1041-1061.

Ingleby, B., 2014: Global assimilation of air temperature, humidity, wind and pressure from surface stations. *Quart. J. Roy. Meteor. Soc.*, **141**, 504-517.

Jacques A. A., J. D. Horel, E. T. Crosman, and F. L. Vernon, 2015: Central and eastern United States surface pressure variations derived from the USArray network. *Mon. Wea. Rev.*, **143,** 1472-1493.

—, —, —, —, and J. Tytell, 2016: The Earthscope US Transportable Array 1 Hz surface pressure dataset. *Geoscience Data J.*, **3**, 29-36.

Johnson, J. T., P. L. MacKeen, A. Witt, E. D. Mitchell, G. J. Stumpf, M. D. Eilts, and K. W. Thomas, 1998: The Storm Cell Identification and Tracking Algorithm: an enhanced WSR-88D algorithm. *Wea. Forecasting*, **13**, 263-276.

Jung, S., and G. Lee, 2015: Radar-based cell tracking with fuzzy logic approach. *Meteor. Applications*., **22**, 716-730.

Knupp, K. R., and Coauthors, 2014: Meteorological Overview of the Devastating 27 April 2011 Tornado Outbreak. *Bull. Amer. Meteor. Soc.*, **95**, 1041-1062.

Koch, S. E., and C. O'Handley, 1997: Operational forecasting and detection of mesoscale gravity waves. *Wea. Forecasting*, **12**, 253-281.

——, and S. Saleeby, 2001: An automated system for the analysis of gravity waves and other mesoscale phenomena. *Wea. Forecasting*, **16**, 661-679.

König, W., R. Sausen, and F. Sielmann, 1993: Objective identification of cyclones in GCM simulations. *J. Climate*, **6**, 2217-2231.

Koppel, L. L., L. F. Bosart, and D. Keyser, 2000: A 25-yr climatology of large-amplitude hourly surface pressure changes over the conterminous United States. *Mon. Wea. Rev.*, **128**, 51-68.

Kravtsov, S., I. Rudeva, and S. K. Gulev, 2015: Reconstructing sea level pressure variability via a feature tracking approach. *J. Atmos. Sci.*, **72**, 487-506.

Lei, L., and J. L. Anderson, 2014: Impacts of frequent assimilation of surface pressure observations on atmospheric analyses. *Mon. Wea. Rev.*, **142**, 4477-4483.

Lindzen, R. S. and K. Tung, 1976: Banded Convective Activity and Ducted Gravity Waves. *Mon. Wea. Rev.*, **104**, 1602-1617.

Liu, Y., D. Xi, Z. Li, and C. Shi, 2014: Automatic tracking and characterization of cumulonimbus clouds from FY-2C geostationary meteorological satellite images. *Advances in Met.*, **2014**, 1-18.

Loehrer, S. M., and R. H. Johnson, 1995: Surface pressure and precipitation life cycle characteristics of PRE-STORM mesoscale convective systems. *Mon. Wea. Rev.*, **123**, 600-621.

Madaus, L. E., G. J. Hakim, and C. F. Mass, 2014: Utility of dense pressure observations for improving mesoscale analyses and forecasts. *Mon Wea Rev.*, **142**, 2398-2413.

Mass, C. F., and L.E. Madaus, 2014: Surface pressure observations from smartphones: A potential revolution for high-resolution weather prediction? *Bull. Amer. Meteor. Soc.*, **95**, 1343-1349.

McMillen, J. D., and W. J. Steenburgh, 2015: Capabilities and limitations of convection-permitting WRF simulations of lake-effect systems over the Great Salt Lake. *Wea. Forecasting*, **30**, 1711-1731.

Metz, N.D., and L.F. Bosart, 2010: Derecho and MCS development, evolution, and multiscale interactions during 3-5 July 2003. *Mon. Wea. Rev.*, **138**, 3048-3070.

Mittermaier, M. P., and R. Bullock, 2013: Using MODE to explore the spatial and temporal characteristics of cloud cover forecasts from high-resolution NWP models. *Met. Applications*, **20**, 187-196.

Mohr, M., 2004: Problems with the mean sea level pressure field over the western United States. *Mon. Wea. Rev.*, **132**, 1952-1965.

Novak, D. R., and B. A. Colle, 2006: Observations of multiple sea breeze boundaries during an unseasonably warm day in metropolitan New York City. *Bull. Amer. Meteor. Soc.*, **87**, 169-174.

Plougonven, R., and F. Zhang, 2014: Internal gravity waves from atmospheric jets and fronts, *Rev. Geophys.*, **52**, 33-76.

Przybylinski, R. W., 1995: The bow echo: observations, numerical simulations, and severe weather detection methods. *Wea. Forecasting*, **10**, 203-218.

Raible, C. C., P. M. Della-Marta, C. Schwierz, H. Wernli, and R. Blender, 2008: Northern Hemisphere extratropical cyclones: A comparison of detection and tracking methods and different reanalyses. *Mon. Wea. Rev.*, **136**, 880-897.

Ramamurthy, M. K., R. M. Rauber, B. P. Collins, and N. K. Malhotra, 1993: A comparative study of large-amplitude gravity-wave events. *Mon. Wea. Rev.*, **121**, 2951-2974.

Ruppert, J. H., and L. F. Bosart, 2014: A case study of the interaction of a mesoscale gravity wave with a mesoscale convective system. *Mon. Wea. Rev.*, **142**, 1403-1429.

Schneider, R. S., 1990: Large-amplitude mesoscale wave disturbances within the intense midwest extratropical cyclone of 15 December 1987. *Wea. Forecasting*, **5**, 533-558.

Smith, B. T., T. E. Castellanos, A. C. Winters, C. M. Mead, A. R. Dean, and R. L. Thompson, 2013: Measured Severe Convective Wind Climatology and Associated Convective Modes of Thunderstorms in the Contiguous United States, 2003-09. *Wea. Forecasting*, **28**, 229-236.

Tian, W., D. J. Parker, S. Mobbs, M. Hill, C. A. D. Kilburn, and D. Ladd, 2004: Observing coherent boundary layer motions using remote sensing and surface pressure measurement. *J. Atmos. Oceanic Technol.*, **21**, 1481-1490.

Trapp, R. J., D. M. Wheatley, N. T. Atkins, R. W. Przybylinski, and R. Wolf, 2006: Buyer Beware: Some Words of Caution on the Use of Severe Wind Reports in Postevent Assessment and Research. *Wea. Forecasting*, **21**, 408-415.

Tyndall D., and J. Horel, 2013: Impacts of mesonet observations on meteorological surface analyses. *Wea. Forecasting*, **28**, 254-269.

Tytell J., F. Vernon, M. Hedlin, C. de Groot Hedlin, J. Reyes, B. Busby, K. Hafner, and J. Eakins J, 2016: The USArray Transportable Array as a platform for weather observation and research. *Bull. Amer. Meteor. Soc.*, **97**, 603-619.

Viana, S., E. Terradellas, and C. Yagüe, 2010: Analysis of gravity waves generated at the top of a drainage flow. *J. Atmos. Sci.*, **67**, 3949-3966.

Whitaker, J. S., G. P. Compo, X. Wei, and T. M. Hamill, 2004: Reanalysis without radiosondes using ensemble data assimilation. *Mon. Wea. Rev.*, **132**, 1190-1200.

Widanagamaachchi, W., C. Christensen, P.-T. Bremer, and V. Pascucci, 2012: Interactive exploration of large-scale time-varying data using dynamic tracking graphs. *IEEE Symposium on Large Data Analysis and Visualization (LDAV)*, **2012**, 9-17.

Yussouf, N., D. C. Dowell, L. J. Wicker, K. H. Knopfmeier, and D. M. Wheatley, 2015: Storm-Scale Data Assimilation and Ensemble Forecasts for the 27 April 2011 Severe Weather Outbreak in Alabama. *Mon. Wea. Rev.*, **143**, 3044-3066.

Zhang, F., S. E. Koch, C. A. Davis, and M. L. Kaplan, 2001: Wavelet analysis and the governing dynamics of a large-amplitude mesoscale gravity-wave event along the East Coast of the United States. *Quart. J. Roy. Meteor. Soc.*, **127**, 2209-2245.

CHAPTER 5

CONCLUSION

5.1 Summary of Findings

The addition of atmospheric pressure sensors to the EarthScope USArray Transportable Array (TA) in order to eliminate atmospheric pressure noise from seismic signatures resulted in a dataset of high temporal frequency surface pressure observations over the eastern half of the United States never before available to the atmospheric science community. As an initial task for this research, these 1-Hz observations have been collected and averages over 5-min intervals have been distributed to MesoWest and MADIS users. Distribution to MADIS allows for the real-time pressure data to be included in NCEP data assimilation procedures. The 1-Hz pressure data from 1 Jan 2010 to the present is available for research purposes with graphical products to access the 1-Hz data available via the web (http://meso1.chpc.utah.edu/usarray/). An official repository for the 1-Hz data has been established within the NCAR Research Data Archive, which contains data through 31 Dec 2015 and will be updated annually. Having the data available in an official data repository is increasingly important for research projects funded by the National Science Foundation and other federal agencies.

The high temporal resolution, platform uptime, and data quality made this dataset an ideal candidate for time series analyses to quantify the occurrences of mesoscale,

subsynoptic, and synoptic phenomena that produce large pressure perturbations. Perturbation pressure variance analyses for stations across the central and eastern United States reveal geographic regions of prominent variations consistent with prior pressure feature climatologies. As should be expected, synoptic-scale weather systems dominate during winter, with the synoptic pressure variance increasing with increasing latitude. Diurnal and semidiurnal tides tend to dominate the frequency band referred to as subsynoptic, with decreasing variance with increasing latitude. Mesoscale variations are most prevalent during spring and summer across the central United States, which is consistent with climatologies related to mesoscale convective systems. Analyses of large pressure signature (rise and fall) occurrences within the three frequency bands are similar to the variance analyses, highlighting regions of mesoscale and synoptic system activity.

The results of the time series analyses provided motivation to extend the use of the pressure data at hundreds of locations to examine the spatiotemporal characteristics of mesoscale pressure perturbations. The spring and summer 2011 seasons were selected for further analysis due to a large number of mesoscale signatures and high (relative to average) mesoscale variance while the TA was deployed over the central United States. Hourly 5-km horizontal resolution Real Time Mesoscale Analysis surface pressure grids were collected and used as an initial background field of surface pressure. These hourly pressure analyses were interpolated to 5-min intervals from 1 Mar – 31 Aug 2011. Using the high temporal resolution TA observations and two-dimensional variational techniques, surface pressure analysis grids at 5-min intervals and 5-km spatial resolution were produced. Band-pass filtering (10 min – 12 h) was then used to isolate mesoscale pressure perturbations. A feature detection algorithm was developed using concepts

derived from existing detection procedures to identify and quantify characteristics (e.g., phase speed) of prominent mesoscale features.

Case studies of two detected mesoscale features (a mesoscale convective system and gravity wave event) are used to illustrate the detection and tracking procedures, as well as to analyze the degree to which the detected pressure perturbations align with corroborating surface and precipitation features. Prominent mesoscale perturbations are most prevalent across the southern and central Great Plains during spring 2011, with a shift in occurrence frequency northward to the north-central Great Plains during summer. Analyses of assessed feature tracks and calculated speeds and directions reveal a seasonal shift for generally faster, east-northeastward moving features in spring to slower, east-southeastward movement during summer, consistent with seasonal shifts in the synoptic pattern generally present over the central United States. Median feature speeds for over 75% of the detected features are within the 15-35 m s^{-1}, established by many previous studies as being commonplace speeds for mesoscale convective systems and solitary gravity waves.

5.2 Future Work

The results of this dissertation highlight several potential avenues for future work. As described in Chapter 4, the most natural extension of this work would be to expand to utilizing additional observational and numerical gridded resources to assess mesoscale pressure perturbations. The temporal resolution and availability of surface observations through a wide variety of resources continue to increase. Many mesonets have improved temporal resolution to 15 min or greater, with extended availability via resources such as

the MesoWest and MADIS systems. When considering surface pressure, the potential use of observations from nonstandard networks increases in part because of fewer concerns with station siting and other metadata factors. Assuming reasonable instrumentation and data quality, the quantity of pressure observations available now could provide a more detailed and accurate representation of mesoscale pressure perturbation features. The incorporation of "Internet of Things" technologies (e.g., pressure observations from cell phones), further adds to the growing reservoir of observational pressure data. Similar methods to generate an increased temporal resolution set of gridded analyses (e.g., every 15 min or 5 min) could be employed that could assess perturbation features over a much broader region and time period than that assessed in this dissertation.

In terms of gridded background pressure resources, the Real Time Mesoscale Analysis has gone through several updates since 2011, including improved horizontal resolution (now 2.5 km) and switching from background fields obtained from the Rapid Update Cycle model to the NOAA High Resolution Rapid Refresh (HRRR) model as an initial grid resource. The HRRR itself also provides an additional resource of gridded analyses that could serve as background grids for a similar approach to this study. However, while spatial resolution for these resources has increased, the available temporal resolution remains hourly.

Another possible extension arises from an operational perspective. Over the previous two decades there have been attempts within the community to develop a real-time operational inertial gravity wave detection system. In several cases those attempts were met with concerns over real-time access to observations with high enough temporal

frequency, in addition to computing resource and adequate detection of feature concerns. As stated previously, continuous improvements in real-time observational data access, improved gridded analyses, and computational resources make such a task much more feasible. This research illustrates potential methodologies that could be utilized to identify the initial pressure perturbation features associated with such features. Some alterations would be required due to aliasing concerns when utilizing filtering procedures in a real-time capacity, though experimental attempts to depict real-time perturbation features have been created as a part of monitoring the incoming TA data stream via web products (http://meso1.chpc.utah.edu/usarray/). Similar algorithms could be enacted to detect perturbations in temperature, wind, and other sensible measurement fields to further characterize a mesoscale system (e.g., cold pool of MCS, wind shift with inertial gravity wave). Incorporating further datasets such as radar imagery could add confidence in identifying and tracking such features in an operational system.

Finally, while the EarthScope campaign is entering its final phase in Alaska, there is a wealth of information that can still be gained through utilizing the TA surface pressure data as either a primary or secondary resource for research initiatives. The deployment of TA platforms in Alaska should provide a dataset comparable to that which was acquired for this research, and could be utilized to study additional atmospheric phenomena such as mountain waves and other terrain-flow interactions. Over 150 TA deployments remain in place as well across the central and eastern United States and continue to routinely collect data, and could serve as another valuable resource for real-time detection of inertial gravity wave features and case studies of past events. Procedures to collect and archive the TA data at the University of Utah remain in place,

and updates to the NCAR Research Data Archive will continue on an annual basis while the TA program continues.